A RAMAN INVESTIGATION OF THE A_g OXYGEN VIBRATIONS IN YTTRIUM BARIUM COPPER OXIDE

by

Eric Herbert Altendorf
B.Sc., University of Waterloo, 1986
M.Sc., University of Waterloo, 1988

A THESIS SUBMITTED IN PARTIAL FULFILLMENT OF
THE REQUIREMENTS FOR THE DEGREE OF
DOCTOR OF PHILOSOPHY
in the Department
of
PHYSICS

SIMON FRASER UNIVERSITY
November 1992

APPROVAL

Name: Eric Herbert Altendorf
Degree: Doctor of Philosophy
Title of Thesis: A Raman Investigation of the A_g Oxygen Vibrations in Yttrium Barium Copper Oxide

Examining Committee: Chairman: Dr. M. L. W. Thewalt

Dr. J. C. Irwin, Professor
Senior Supervisor

Dr. S. Gygax, Professor

Dr. B. Heinrich, Director of the Surface Physics Laboratory

Dr. B.P. Clayman, Professor and Dean of Graduate Studies, Internal Examiner

Dr. J.E. Eldridge, Professor, Dept. of Physics, University of British Columbia, External Examiner

Date Approved: December 11, 1992

PARTIAL COPYRIGHT LICENSE

I hereby grant to Simon Fraser University the right to lend my thesis, project or extended essay (the title of which is shown below) to users of the Simon Fraser University Library, and to make partial or single copies only for such users or in response to a request from the library of any other university, or other educational institution, on its own behalf or for one of its users. I further agree that permission for multiple copying of this work for scholarly purposes may be granted by me or the Dean of Graduate Studies. It is understood that copying or publication of this work for financial gain shall not be allowed without my written permission.

Title of Thesis/Project/Extended Essay

A RAMAN INVESTIGATION OF THE A_g OXYGEN VIBRATIONS IN YTTRIUM BARIUM COPPER OXIDE

Author:

(signature)

ERIC ALTENDORF

(name)

December 16, 1992

(date)

ABSTRACT

In this thesis, an investigation of three oxygen dependent optical phonons at 340, 440, and 500 cm^{-1} in the prototype high temperature superconductor $YBa_2Cu_3O_7$, is carried out by means of Raman light scattering.

The frequency and linewidth shifts in isotopically exchanged samples (^{18}O for ^{16}O) suggest that the 340 and 440 cm^{-1} modes primarily involve a different set of atomic sites than the 500 cm^{-1} phonon in agreement with the predictions of lattice dynamics models. A linear chain is used to numerically model the 500 cm^{-1} mode and generate Raman peaks whose isotopic frequency shifts and linewidth changes are in good agreement with the corresponding experimental observations.

The temperature dependences of the 340, 440, and 500 cm^{-1} phonons are investigated in $YBa_2Cu_3O_y$ single crystals with a range of oxygen concentrations ($6.7 \lesssim y \leq 7.0$) and $YBa_2Cu_3O_7$ single crystals containing a small amount of thorium. The results indicate that the superconductivity induced self energy shifts in the 340 cm^{-1} phonon are strongly dependent on the hole concentration. Smaller variations in the superconductivity induced self energy shifts of the 440 and 500 cm^{-1} phonons are also observed. Superconducting gap energy estimates obtained using strong coupling theories range from $2\Delta \approx 5.4k_BT_c$ in the fully oxygenated samples ($y \approx 7.0$) to energies possibly as large as $6.7k_BT_c$ in the deoxygenated and hence hole reduced samples. These values for 2Δ are not entirely consistent with the self energy shifts of the 440 and 500 cm^{-1} modes, however, suggesting the possible existence of two or more gaps with different symmetries.

DEDICATION

To my parents

Ruth and Heinz

QUOTATION

Die ganzen 50 jahre bewusster Grübelei haben mich der Antwort der Frage 'Was sind Lichtquanten' nicht näher gebracht.

Albert Einstein

ACKNOWLEDGEMENTS

I would like to gratefully acknowledge the financial support provided by the Natural Sciences and Engineering Research Council of Canada, Simon Fraser University and by my supervisor, Chuck Irwin. I would also like to thank Dr. Irwin for his guidance, helpful suggestions and keen interest in the work carried out for this thesis.

The experiments carried out in this thesis would not have been possible without the samples which were graciously provided by Ruixing Liang, J.P. Franck, and A. O'Reilly. Ruixing Liang was particularly helpful in providing high quality crystals almost at a moments notice. I am also very much indebted to Janusz Chrzanowski, Jeff Dahn, and Per Joensen for their assistance in various Raman and x-ray experiments. I would also like to thank Georg Soerensen, Dr. S. Gygax, and W. Xing for carrying out magnetic measurements on the samples investigated in this thesis.

Last but certainly not least I would like to thank my wife Sue for her support, patience (while I spent those long nights in the lab), and sense of humor.

TABLE OF CONTENTS

TABLE OF CONTENTS (Continued)

TABLE OF CONTENTS (Continued)

LIST OF TABLES

Table **Page**

LIST OF FIGURES

LIST OF FIGURES (Continued)

LIST OF FIGURES (Continued)

LIST OF FIGURES (Continued)

CHAPTER 1
INTRODUCTION

1.1 Background of High Temperature Superconductors

Superconductivity was discovered by the Dutch physicist Kamerlingh Onnes in 1911 [11O]. Onnes found that when a mercury wire was cooled below 4.2 K its DC electrical resistivity vanished. Further experiments by Onnes revealed that the elements tin and lead also became superconducting at 3.8 K and 6 K respectively [89Ha]. The characteristic temperature at which such materials become superconducting is referred to as the superconducting transition temperature or critical temperature T_c. To present, at least twenty six metallic elements and thousands of alloys and compounds are known to be superconducting when cooled to sufficiently low temperatures [89Ha]. Prior to 1986, however, the highest recorded T_c was 23.2 K for the alloy Nb_3Ge [89Ha].

In 1986, Alex Mueller and Georg Bednorz [86B] observed that the semiconducting compound $LaCuO_4$, when lightly doped with Barium, exhibited a superconducting transition near 30 K. Later that same year Paul Chu and coworkers [87W] raised the value of T_c above the technically significant liquid nitrogen temperature (~ 77 K) by substituting Y for La in the Bednorz and Mueller superconductor. The resulting compound had a T_c of approximately 90 K and was later identified as $YBa_2Cu_3O_7$. Many additional high temperature superconductors based on these two original materials have since been discovered. One of these superconductors is the Thallium based compound, $Tl_2Ba_2Ca_2Cu_3O_{10}$, which also has the highest confirmed superconducting transition temperature of any material (~ 125 K). Most of these high temperature superconductors are comprised of the same

fundamental building blocks as the original $La_{2-x}Ba_xCuO_4$ compound of Bednorz and Mueller. In particular, they all contain planes of copper and oxygen atoms, which have the formula unit CuO_2, and hence are referred to as CuO_2 planes. Separating these planes are metal atoms and copper oxygen chains which serve the structural task of separating the CuO_2 planes and also act as charge reservoirs [89Ga]. The superconductivity in these materials occurs predominantly [89Ga] in the CuO_2 planes. This quasi-two dimensionality is also evident in the normal state where the resistivity perpendicular to the CuO_2 planes can be orders of magnitude larger [90B] than the in-plane resistivity.

The high temperature superconductors are mixed metal oxides which have the mechanical properties of ceramics and the electrical properties of metals. The carrier density, however, is significantly lower [91B] than that of conventional metals. Almost all of these compounds are p-type materials [90B] including $YBa_2Cu_3O_7$, implying that the charge carriers are in the form of holes. The superconducting state of these materials is that of a type II superconductor implying penetration of an external magnetic field in the form of flux lines for a field strength greater than a critical value H_{c1}.

The microscopic mechanism for superconductivity in conventional materials was formulated in 1957 by Bardeen, Cooper, and Schrieffer [57B], and is commonly referred to as the BCS theory. Fundamental to this theory is the realization that an attractive interaction between the electrons at the Fermi surface can lead to a ground state that is separated from the excited electronic state of the system by an energy gap Δ. The source for the attractive interaction can be found in an electron-lattice-electron interaction in which a given electron can effectively attract a second electron by deforming the lattice and creating a temporary region of net positive charge. In the language of

quantum mechanics, the electrons attract one another by exchanging phonons (quantized lattice vibrations). Changing phonon frequencies by replacing atoms with heavier or lighter isotopes should therefore affect the superconducting state. In particular, a shift in the critical temperature due to such isotopic substitution (isotope shift) was predicted by BCS theory and observed experimentally [50M].

The electrons in the BCS ground state are grouped in pairs of opposite momentum, known as Cooper pairs, so that the effective unit of charge is 2e rather than e. The BCS theory is formulated in the so-called weak coupling limit in which the electron-phonon interaction is assumed to be small compared to the maximum phonon energy. A generalization of BCS theory by Eliashberg [60E] allows for arbitrary electron-phonon coupling strengths. Although phonons provide the "glue" to bind the electrons in BCS theory, in general any boson (e.g. magnon, plasmon, exciton etc.) can be utilized within a BCS framework or formalism.

Although it is not clear whether such a formalism can describe the mechanism responsible for superconductivity in the high temperature cuprate superconductors, flux quantization experiments [87G] and inverse Josephson effect experiments [87J] have shown that the elementary current carrying excitation in the superconducting state has charge 2e, suggesting that Cooper pair-like bound states are formed just as in conventional superconductors. Whether electron-phonon interactions provide the binding mechanism as in conventional superconductors is still open to question, but the high value of T_c, and the very small isotope shift [87Ba] [87L] [89F] have led many researchers to propose alternate mechanisms to explain the superconducting state of the cuprates. Mechanisms involving antiferromagnetic fluctuations [86S], magnons [87P], resonating valence bonds

[87A], and anyon superconductivity [88La] are some of the explanations that have been proposed.

Many experiments including infrared reflectivity [90Sa], tunneling [88Ta], photoemission [89I], and Raman spectroscopy [90Fb] [88Cb], have shown that gap-like behavior exists in the high temperature superconductors. Unfortunately at the time of this writing, even for the prototype high temperature superconductor, $YBa_2Cu_3O_7$, no consensus has been found regarding the symmetry or magnitude of the gap or for that matter whether a true gap (no states in the gap) actually exists.

This lack of any clear understanding of the underlying mechanism of the high temperature superconductors as well as the possibility of far-reaching technical applications have led to an unprecedented volume of research focussing on these materials. One of the simplest, most heavily investigated, and hence best characterized member of the copper oxide family of high temperature superconductors is $YBa_2Cu_3O_7$, which has a critical temperature of about 93 K. High quality single crystals of $YBa_2Cu_3O_7$ are now available making this compound an ideal choice for investigating the fundamental properties of high temperature superconductivity. In this thesis both polycrystalline and single crystal samples of $YBa_2Cu_3O_7$ will be investigated by Raman light scattering. In particular, oxygen isotope substitution in polycrystalline $YBa_2Cu_3O_7$ samples will be used to investigate the Raman active phonons at nominal frequencies of 340, 440, and 500 cm^{-1} which are due to oxygen atom vibrations with A_g symmetry. The effects of oxygen doping on these same phonon modes will then be investigated in $YBa_2Cu_3O_y$ crystals with $6.7 \lesssim y \leq 7.0$.

1.2 Raman light scattering and High Temperature Superconductors

Raman light scattering has been particularly useful for investigating $YBa_2Cu_3O_7$ and other high temperature superconductors since results could be obtained from very small samples by focussing the incident laser spot with a lens or microscope. This is particularly relevant for investigating single crystals of $YBa_2Cu_3O_7$ whose dimensions are typically 1.0 mm by 1.0 mm by 0.1 mm or smaller. In addition, the Raman technique probes the optical phonons at the center of the first Brillouin zone. Since phonons play such an important role in conventional superconductors, their behavior in these materials is well understood and can be explained using BCS or strong coupling theories. It is therefore of interest to determine the degree to which the behavior of the phonons in the high temperature superconductors such as $YBa_2Cu_3O_7$ conform to the predictions of these same theories and the conventional BCS or strong coupling models of superconductivity. Such comparisons can for instance yield information about the nature of the superconducting gap, which may in turn provide clues about the form of the excitation(s) mediating the electron pairing. Fundamental to the success of this approach, however, is a clear understanding of the phonons themselves.

In this thesis the results of Raman light scattering from both polycrystalline $YBa_2Cu_3O_7$ and single crystal $YBa_2Cu_3O_y$ ($6.7 \lesssim y \lesssim 7.0$) samples are discussed. Chapter two, following this introduction, deals with the theoretical aspects of the Raman technique which are required to interpret the results presented in chapters five and six. Chapter three discusses the symmetry and Raman light scattering properties of $YBa_2Cu_3O_7$, and the known properties of the Raman active phonon modes in this compound. Chapter four gives details on the preparation and characterization of the

various samples investigated in this thesis as well as the experimental Raman light scattering apparatus and arrangement.

In order to better understand the nature of the phonon modes discussed in this thesis an analysis of the effects of $^{16}O/^{18}O$ isotope substitution has been carried out and is presented in chapter five. Polycrystalline samples were used for this work due to the relative ease that such isotopically substituted samples could be grown and prepared. The results are consistent with the eigenmodes and atomic displacement patterns assigned to these phonons by dynamical models.

Chapter six examines the superconductivity-induced changes in the phonons at frequencies of 340, 440, and 500 cm^{-1}. Changes in the energies and lifetimes of these oxygen vibrations which occur as the samples are cooled below T_c are compared to the predictions of strong coupling theories. $YBa_2Cu_3O_7$ crystals containing thoria impurities and crystals with a variety of oxygen concentrations are investigated in order to determine the effects of hole concentration on the phonon renormalization below T_c, and the derived value of the superconducting gap energy, 2Δ, implied by the corresponding phonon frequency and linewidth shifts.

In the weak coupling limit, phonons with energies just above the superconducting gap energy, 2Δ, can decay below T_c by scattering Cooper pairs into quasi-particle states. This results in a reduction in the phonon lifetime and a corresponding broadening of the associated Raman peak [73A]. In addition phonons with energies just below 2Δ should soften or decrease in frequency [75S] due to the repulsion of the interacting phonon and gap excitations. Strong electron-phonon coupling [90Z] [92Mb] results in a smearing of these effects so that both softening (decrease in frequency) and broadening can occur for a phonon sufficiently close in energy to the value of

the superconducting gap energy 2Δ. A significant softening (decrease in frequency), by about 2%, of the 340 cm^{-1} phonon in $YBa_2Cu_3O_7$ as first observed by Macfarlane et al. [87M], and subsequent observations of broadening by up to 50% of this same mode [88Cb], therefore suggest that the superconducting gap energy, 2Δ, should be in the vicinity of the energy of the 340 cm^{-1} phonon.

Various groups [90Fb] [91Ab] [91Ma] [92A] have utilized the anomalous frequency and linewidth shifts below T_c of the 340 cm^{-1} mode as well as similar but less pronounced changes in nearby phonons at 440 and 500 cm^{-1}, to obtain estimates of the superconducting gap energy, 2Δ, in $YBa_2Cu_3O_7$. The resulting values obtained range from $2\Delta \approx 5.0k_BT_c$ ($\approx$ 312 cm^{-1}) [90Fb] to $2\Delta \approx 7.7k_BT_c$ ($\approx$ 480 cm^{-1}) [91Ma], primarily reflecting a significant variation in the behavior of the 340 cm^{-1} phonon below T_c for different crystals with essentially the same T_c ($\approx$ 90 K) and superconducting properties. This lack of correlation between 2Δ and T_c is a significant departure from the universal dependence predicted by BCS theory, namely $2\Delta=3.52k_BT_c$ [90Tb].

In this thesis, the temperature dependences of all three oxygen dependent phonons at 340, 440, and 500 cm^{-1}, are obtained from single crystals with a range of oxygen concentrations ($YBa_2Cu_3O_y$: $6.7 \lesssim y \lesssim 7.0$) as well as $YBa_2Cu_3O_7$ crystals containing a small amount of Thorium. The results obtained, as well as the behavior of the 340 cm^{-1} mode in crystals containing other impurities [91Ma], suggest that the previously mentioned variations [90Fb] [91Ma] in the behavior of the 340 cm^{-1} phonon below T_c are due to small differences in the oxygen or hole concentrations of the crystals, near y = 7.0. If the changes in the linewidth and frequency of the 340 cm^{-1} phonon below T_c result from the formation of a superconducting gap, or more generally a redistribution of electronic states below T_c, then this redistribution

of electronic states is also very sensitive to the oxygen or hole concentration. The behavior of the 440 and 500 cm^{-1} phonons is not entirely consistent with this picture, however, suggesting that these modes may interact with a different group of electrons or a different gap. Estimates for the superconducting gap energy, 2Δ, based on strong coupling models [90Z] and the behavior of the 340 cm^{-1} phonon in each of the crystals studied, indicate that 2Δ increases as the oxygen or hole concentration, y, decreases from y = 7.0 where $2\Delta \approx 5.4k_BT_c$, to y = 6.9 where $2\Delta \approx 7.0k_BT_c$.

Chapter seven restates these conclusions in more detail based on the results presented in chapters five and six.

Finally, it should be mentioned that anomalous phonon softening has been observed for infrared-active phonons in $YBa_2Cu_3O_7$ [89Gb], $YBa_2Cu_3O_8$ [92Lb] and oxygen deficient or Au and Pr doped $YBa_2Cu_3O_{7-\delta}$ [92Lb]. Phonons with energies as high as 569 cm^{-1} were found [89Gb] to soften in $YBa_2Cu_3O_7$ suggesting a significantly higher value for 2Δ than is obtained from the Raman measurements. The anomalous decreases in frequency [92Lb] of the phonons in the $YBa_2Cu_3O_8$ samples, and oxygen depleted or Au and Pr doped $YBa_2Cu_3O_{7-\delta}$ samples were, however, found to start up to 50-60 K above T_c making it difficult to establish a connection between the phonon softening and the onset of superconductivity in these compounds.

CHAPTER 2

THEORY OF RAMAN SCATTERING

2.1 Introduction

Raman scattering is the inelastic scattering of light by matter. The discovery of this effect was announced in 1928 by C.V. Raman after a systematic investigation of the scattering of light from various liquids and solids [27R] [28Ra-c]. In the Raman process elementary excitations of the material system may be created in what is referred to as a Stokes process, or destroyed in an anti-Stokes process. The excitations involved can take many forms including electronic transitions, vibrational modes, magnetic excitations and others. In this thesis the principal excitations studied will be lattice vibrations in the form of optical phonons.

In a single scattering event an incident photon of energy $\hbar\omega_L$ is destroyed and simultaneously a scattered photon of energy $\hbar\omega_S$ is created. Energy is conserved in the scattering process so that

$$\omega_L = \omega_S \pm \sum_j \omega_j \qquad (2.1),$$

where ω_j are the frequencies of the elementary excitations and the plus(minus) signs refer to Stokes(anti-Stokes) processes. Unlike absorption, the energy of the incident photon is usually significantly greater than the energies of the excitations and does not correspond to the energies of any direct transitions

$$\omega_j << \omega_L, \omega_S \qquad (2.2).$$

This thesis will concern itself primarily with first order processes in which a single excitation is created or destroyed so that equation 2.1 becomes

$$\omega_L = \omega_S \pm \omega_j \qquad (2.3).$$

In addition if wavevector is a good quantum number, that is, if the elementary excitation can be characterized by a wavevector, $\vec{k}_j$, then wavevector conservation holds and

$$\vec{k}_L = \vec{k}_S \pm \vec{k}_j \qquad (2.4).$$

where $\vec{k}_L$ and $\vec{k}_S$ are the wavevectors of the incident and scattered light respectively. In principle this equation only holds for transparent samples which possess translational symmetry (e.g. large non-absorbing single crystals).

For the work presented in this thesis the incident photons will be in the visible region of the electromagnetic spectrum and hence will have wavelengths (λ) of about 5000 Å. The magnitude of the wavevector of the incident light is therefore approximately 10^5 cm^{-1}. By comparison phonon wavevectors at the edge of the first Brillouin zone have magnitudes of the order of 10^8 cm^{-1}. Compared to the phonon wavevectors the incident and scattered photon wavevectors are therefore nearly zero implying that the phonons that can participate in the first order Raman scattering processes described by equations 2.3 and 2.4 must come from near the Brillouin zone center, so that $\vec{k}_j = \vec{0}$. The resulting spectra will therefore consist of discrete lines at the $\vec{k}_j \approx \vec{0}$ optical phonon frequencies.

For the samples studied in this thesis wavevector conservation is only approximately satisfied due to the fact that the samples are opaque. For $YBa_2Cu_3O_7$ normally incident visible light penetrates to a depth of about $\Delta x = 1000$ Å into the surface resulting in an uncertainty or smearing of the wavevector of the incident light. The order of magnitude of the amount of smearing can be estimated from the uncertainty principle and gives a value of

$\Delta k \approx 1/\Delta x \approx 10^5 cm^{-1}$. The magnitude of the total momentum or wavevector transfer to the phonon is thus still at the most of the order of 10^5 cm^{-1} and hence to a good approximation the $\vec{k} = \vec{0}$ selection rule still applies.

A more significant effect occurs through the loss of translational symmetry achieved by the presence of defects or substitutional impurities. At high impurity or defect concentrations the uncertainty in wavevector transfer may be as large as the wavevectors at the Brillouin zone boundary in which case the $\vec{k} = \vec{0}$ selection rule no longer applies and the first order Raman spectrum becomes an approximate representation of the one-phonon density of states.

2.2 The Raman Cross-Section

The main features of the first order Raman effect as described in the previous section can be understood classically using a simple one-dimensional model. If α is the polarizability of the scattering medium then the polarization induced by the incident electric field is given by

$$P=\alpha E \tag{2.5}$$

Excitations such as phonons can then give rise to Raman light scattering by modulating the polarizability α. For example, if α is expanded about an equilibrium value α_0 in terms of atomic displacements u_j then

$$\begin{aligned} \alpha &= \alpha_o + \frac{\partial \alpha}{\partial u_j} u_j + \frac{\partial^2 \alpha}{\partial u_j \partial u_i} u_j u_i + \cdots \\ &\approx \alpha_o + \alpha_1 u_j = \alpha_o + \alpha_1 \cos \omega_j t \end{aligned} \tag{2.6}$$

If the incident electric field is produced by a monochromatic light source such as a laser then

$$E = E_o \cos \omega_L t \tag{2.7},$$

which when combined with equations 2.6 and 2.5 gives

$$P = \alpha_o E_o \cos \omega_L t + \frac{\alpha_1 E_o}{2}\left\{\cos(\omega_L + \omega_j)t + \cos(\omega_L - \omega_j)t\right\} \tag{2.8}.$$

Since the scattered light is proportional to P^2, the first term in equation 2.8 corresponds to the elastically scattered light unshifted in frequency (Rayleigh scattering) while the remaining term corresponds to the Stokes and anti-Stokes Raman scattered light. Note that as assumed in the above derivation, α_1 and the higher order terms in equation 2.6 are usually small when compared to α_o implying that the Raman scattering effect is relatively weak when compared to the Rayleigh scattering contribution.

Although this simple argument contains many of the essential features of the Raman effect it does not yield an expression for the actual Raman cross-section. The anti-Stokes component, for example, vanishes at low temperatures, a feature which is not predicted by the previous derivation. A more complete description requires a quantum mechanical derivation, the results of which will now be given. The exact form of a Raman cross-section depends on the microscopic details of the material system. Montgomery [71Ma] has derived a basic form for the Raman cross-section appropriate for scattering from phonons which serves as a good starting point for describing more sophisticated forms of Raman scattering. The basic assumptions of this derivation will now be given. For more details consult the theses of Montgomery or Holy [71Ma] [77H].

The Hamiltonian for the matter-photon system can quite generally be determined from the Hamiltonian for the matter system, H_o, by replacing the ith particle's momentum, $\vec{p}_i$, by $\vec{p}_i - \frac{e_i}{c}\vec{A}(\vec{r},t)$, so that

$$H = \sum_i \frac{1}{2m_i}\left\{\vec{p} - \frac{e_i}{c}\vec{A}(\vec{r}_i,t)\right\}^2 + V(\vec{r}) = H_o + H_1 + H_2 \qquad (2.9a),$$

$$H_o = \sum_i \frac{p_i^2}{2m_i} + V(\vec{r}) \qquad (2.9b),$$

$$H_1 = -\sum_i \left(\frac{e_i}{2m_i c}\right)[\vec{p}_i.\vec{A} + \vec{A}.\vec{p}_i] \qquad (2.9c),$$

$$H_2 = \sum_i \left(\frac{e_i}{2m_i c^2}\right)A^2 \qquad (2.9d)$$

where m_i and e_i are the particle mass and charge, $\vec{A}$ is the vector potential of the electromagnetic field, and $V(\vec{r})$ is the total potential energy of the matter system. The radiation field contributions, H_1 and H_2, are treated as perturbations to the initial matter system. It is therefore assumed that the incident photon energies are considerably smaller than any direct transition energies. The initial matter-photon state is given by the initial wavefunction of the matter system, $\phi_i(\vec{r})$, and the initial state of the radiation field, $|\cdots 0,0,0,N_{k_L,\eta_L},0,0,0,\cdots>$, which is comprised of N_{k_L,η_L} laser photons of energy $\hbar\omega_L = ck_L$ and no other photons in any other states. Similarly the final matter-photon state is given by the final wavefunction of the matter system, $\phi_f(\vec{r})$, and the final state of the radiation field, $|\cdots 0,0,0,N_{k_L,\eta_L}-1,N_{k_s,\eta_s}=1,0,0,0,\cdots>$, which indicates the destruction of a laser photon and the creation of a scattered photon. The scattering event therefore consists of a transition from an initial matter-photon state $|I>=|\phi_i(\vec{r})>|\cdots 0,0,0,N_{k_L,\eta_L},0,0,0,\cdots>$, to a final matter-photon state $|F>=|\phi_f(\vec{r})>|\cdots 0,0,0,N_{k_L,\eta_L}-1,N_{k_s,\eta_s}=1,0,0,0,\cdots>$.

Following the standard procedures of time dependent perturbation theory [74S], the general matter wavefunction Ψ is expanded as

$$\Psi = \sum_m c_m(t)\phi_m(\vec{r})\exp(i\omega_m t) \qquad (2.10),$$

where $\phi_m(\vec{r})$ are the eigenfunctions of the unperturbed Hamiltonian, H_o, and form a complete set of states. Further, assuming that the matter-photon system is in state $|I>$ at time $t=0$ gives $c_m(0)=\delta_{i,m}$. The transition probability per unit time is then given by

$$\frac{|c_f(t)|^2}{t}=\frac{|c_f^{H_1}(t)+c_f^{H_2}(t)|^2}{t} \qquad (2.11),$$

where $c_f^{H_1}(t)$ is the contribution from perturbation Hamiltonian H_1 and $c_f^{H_2}(t)$, is due to H_2. First order contributions are contained in $c_f^{H_2}(t)$, while contributions from second order processes are contained in $c_f^{H_1}(t)$. In both first and second order processes an incident photon is destroyed and a scattered photon created. The second order processes involve virtual intermediate matter states. Transitions to these states cannot be directly observed and do not need to conserve energy.

In general, both H_1 and H_2 contributions to the perturbation Hamiltonian are needed [78H] to determine the inelastic scattering rate through equation 2.11. The second order H_1 contribution, through the intermediate states, allows for scattering processes involving interband transitions between the initial and final states. For these processes, which include scattering from crystal lattice vibrations (phonons) [78H], the remaining first order H_2contribution which describes intraband scattering processes can be shown [69B] to be small. In the derivation discussed here the H_2contribution is cancelled [69B] by part of the H_1 contribution so that only second order processes are represented in the final expression for the Raman cross-section.

At this point a number of simplifying approximations are introduced. As mentioned previously, the photon wavevectors $\vec{k}_L$ and $\vec{k}_s$ are essentially

zero on the scale of the first Brillouin zone boundary wavevectors and can to a good approximation be taken as zero. This is often referred to as the dipole approximation. Also, to a good approximation when considering scattering due to phonons, it may be assumed that photons with optical frequencies do not result in any real electronic transitions so that the initial and final electronic states are the ground state while the intermediate states are virtual. Finally the ionic masses respond much more slowly than the electrons to an oscillating electric field, and at the relatively high optical frequencies of the incident light, the ionic contribution to the polarizability and scattered light can be neglected.

These approximations allow the Raman cross-section to be written in terms of matrix elements of the form, $< v_i | P_{\alpha\beta}(\omega_L, R) | v_f >$, where $|v_i>$ and $|v_f>$ are the initial and final vibrational states respectively, and $P_{\alpha\beta}(\omega_L, R)$ is a component of the electronic polarizability tensor which depends parametrically on the frequency of the incident light and the nuclear coordinates R. It is therefore possible to expand $P_{\alpha\beta}$, in a Taylor series with respect to nuclear positions, or more appropriately, for phonons with respect to the normal coordinates Q_j:

$$P_{\alpha\beta}(\omega_L, R) = P^o_{\alpha\beta} + \sum_j \left\{ \frac{\partial P_{\alpha\beta}}{\partial Q_j} \right\}_o Q_j + \sum_{j,j'} \left\{ \frac{\partial^2 P_{\alpha\beta}}{\partial Q_j \partial Q_{j'}} \right\}_o Q_j Q_{j'} + \cdots \qquad (2.12).$$

The first term is responsible for elastic Rayleigh scattering while the second and third terms cause first and second order Raman scattering respectively.

Keeping only the first order contribution the differential Raman cross-section for Stokes scattering becomes [71Ma]

$$\boxed{\frac{d^2\sigma(\omega)}{d\Omega d\omega} = \frac{\omega_L \omega_s^{\,3}}{c^4} \sum_j \frac{\hbar}{2\omega_j} \left| \sum_{\alpha\beta} \eta_{s,\alpha} P^1_{\alpha\beta}(j) \eta_{L,\beta} \right|^2 [n(\omega_j)+1] \delta(\omega - \omega_j)} \qquad (2.13),$$

where $n(\omega_j) = \dfrac{1}{\exp(\dfrac{\hbar\omega_j}{k_B T}) - 1}$ is the Bose factor , $P^1_{\alpha\beta}(j) \equiv \left\{ \dfrac{\partial P_{\alpha\beta}}{\partial Q_j} \right\}_o$, and $\eta_{L,\beta}$ and $\eta_{s,\alpha}$ are components of the unit polarization vectors of the incident and scattered light respectively. The expression for anti-Stokes scattering can be obtained by replacing $n(\omega_j)+1$ with $n(\omega_j)$ in equation 2.13. This implies that at low temperatures (i.e. room temperature and below) Stokes scattering dominates over anti-Stokes processes. In particular, a ratio of the anti-Stokes to Stokes intensities can be used to deduce the the sample temperature.

Note that first order Raman scattering in an extended medium can also be described by utilizing a macroscopic formalism [78H]. In this approach, excitations in the scattering medium set up fluctuations in the first order polarizability which when combined with the incident electric field generate the scattered light. The fluctuation-dissipation theorem [89P] can be used to demonstrate quite generally [78H] that the resulting Stokes Raman cross-section is proportional to the Bose factor $n(\omega_j)+1$.

2.3 Crystal Symmetry and Selection Rules

The symmetry properties of a given crystal structure can be classified as belonging to one of the 230 possible space groups [77Ba]. The space group of a crystal that does not contain screw axes or glide planes may be denoted $\{R|\vec{L}\}$,

where R is a point group operation, and $\vec{L}$ is a lattice translation vector. In addition the factor group defined as $\{R|\vec{0}\}$, can be shown to be symmorphic with the point group of the unit cell of the crystal.

The effects of the translational symmetry component of the space group can be seen by expanding the Raman polarizability introduced in the previous section (equation 2.13) in terms of nuclear displacements, $u_{j\gamma}(\vec{L})$, where the index j refers to a specific atom in the unit cell and γ is a coordinate index. In particular, the linear term responsible for first order Raman scattering, may be written

$$P_{\alpha\beta} = \sum_{j\gamma,\vec{L}} P^1_{\alpha\beta,j\gamma}(\vec{L}) u_{j\gamma}(\vec{L}) \qquad (2.14),$$

where $P^1_{\alpha\beta,j\gamma}(\vec{L})$ is the first derivative of the polarization with respect to the atomic displacement $u_{j\gamma}(\vec{L})$. Note that the dipole approximation was used in the derivation of the Raman cross-section (equation 2.13) described in the previous section. This implies that the incident and scattered photon wavevectors are assumed to be zero. Translational symmetry now requires that $P^1_{\alpha\beta,j\gamma}(\vec{L})$ be independent of $\vec{L}$ so that

$$P_{\alpha\beta} = \sum_{j,\gamma} P^1_{\alpha\beta,j\gamma} \sum_{\vec{L}} u_{j,\gamma}(\vec{L}) \qquad (2.15).$$

Expanding $u_{j\gamma}(\vec{L})$ in terms of normal modes [71Mb] implies that $\sum_{\vec{L}} u_{j\gamma}(\vec{L}) \propto \sum_{\vec{k}} C_{\vec{k}} \sum_{\vec{L}} \exp(i\vec{k}\cdot\vec{L})$ where $\vec{k}$ is a phonon wavevector and $C_{\vec{k}}$ is a $\vec{k}$ dependent amplitude. Since $\sum_{\vec{L}} \exp(i\vec{k}\cdot\vec{L})$ vanishes unless $\vec{k}$ equals zero or a reciprocal lattice vector [71Mb] it follows that only phonons at the Brillouin zone center can contribute to first order Raman scattering through $P^1_{\alpha\beta,j\gamma}(\vec{L})$ in the dipole approximation. Translational symmetry is therefore responsible

for wavevector conservation as given by equation 2.4, and the resulting $\vec{k} = \vec{0}$ selection rule.

The total number of $\vec{k} = \vec{0}$ normal modes is given by 3p, where p is the number of atoms in the unit cell of the crystal. The symmetries of these modes can be determined using the methods of group theory [77Ba]. Briefly, a representation of the point group of the unit cell can be obtained by forming matrices which transform 3p arbitrary displacements of the p atoms of the unit cell under all the symmetry operations of the point group. Decomposing this representation into the irreducible representations of the point group then gives the number of $\vec{k} = \vec{0}$ normal modes corresponding to different symmetries. These symmetry assignments can now be used to determine the number of the Raman active normal modes as well as their symmetries.

First order Raman scattering due to phonons requires that the matrix element $\langle v_i | P_{\alpha\beta} | v_f \rangle$ be non-zero. For the temperatures discussed in this thesis the initial state, $|v_i\rangle$, can to a good approximation be taken as the vibrational ground state which possesses the full symmetry of the point group; Γ_1. The symmetry of the product $P_{\alpha\beta}|v_i\rangle$ is therefore equivalent to the symmetry of the polarizability; Γ_P. Group theoretical methods [77Ba] then predict that in order for the matrix element $\langle v_i | P_{\alpha\beta} | v_f \rangle$ to be non-zero, the symmetry of the final state, $|v_f\rangle$, must be included in an irreducible representation of the polarizability tensor $P_{\alpha\beta}$. The various elements of the polarizability tensor transform as the product of Cartesian coordinates, e.g. P_{xy} as xy, and the representations to which these elements belong are usually tabulated in character tables for various point groups. The symmetries of the $\vec{k} = \vec{0}$ modes can then be compared to the representations of the polarizability tensor thereby determining which modes are Raman active. In particular, for crystals

with a center of inversion only even parity phonons are Raman active while odd parity phonons are infrared active [77Ba].

2.4 Raman scattering from opaque samples

The Raman cross-section derived in section 2.2 and given by equation 2.13, in principle only applies to scattering from transparent samples where the incident and scattered wavevectors can be taken to be zero to a good approximation (dipole approximation). Opaque or metallic samples such as those described in this thesis, are characterized by a complex index of refraction, $\tilde{n} = n - i\kappa$, where κ is the principal absorption coefficient and n is the principal index of refraction. An electric field entering such a material normal to the surface and penetrating to a depth z is attenuated by a factor $\exp(-\frac{z}{\delta})$, where δ is the skin depth which for incident light with a wavelength λ is given by $\delta = \frac{\lambda}{2\pi\kappa}$. As mentioned previously this results in a smearing of the electromagnetic field wavevectors which in turn implies that wavevector conservation as expressed by equation 2.4 no longer strictly applies. For spectra obtained in a near backscattering geometry ($\vec{k}_s \approx -\vec{k}_L$) the maximum wavevector transfer to the scattering medium is given [83P] [84A] approximately by $\frac{4n\pi}{\lambda} \pm \frac{1}{2\delta}$ which for $YBa_2Cu_3O_7$ is about $5(\pm 2)\times 10^5$ cm^{-1} [92F]. This range of wavevectors is nearly zero on the scale of phonon wavevectors at the boundary of the first Brillouin zone ($\approx 10^8$ cm^{-1}) which implies that the $\vec{k} = \vec{0}$ selection rule is still valid to a good approximation.

Similarly, the relatively small value of $\frac{4n\pi}{\lambda}$ implies that the dipole approximation is justified.

As well, Mills et al. [68M] have derived a Raman cross-section for opaque materials and have shown that for phonons with symmetries that would be Raman active in a transparent sample, an expression similar to equation 2.13 is obtained with a reduced overall intensity due to the loss of signal through attenuation effects and the reduction in scattering volume. Since the phonons discussed in this thesis satisfy the above condition, equation 2.13 may be used as a good first approximation for the phonon Raman spectrum.

2.5 Phonon linewidths

For a perfect transparent crystal the Raman cross-section given by expression 2.13 predicts a spectrum which is composed of delta function peaks at the $\vec{k} \approx \vec{0}$ optic mode frequencies. Experimentally observed spectra of single crystals however always exhibit Raman phonon peaks with finite linewidths. For first order Raman phonon peaks, linewidth contributions are primarily the result of anharmonic interactions among phonons, coupling of phonons to other excitations, disorder and finite size effects, and instrumental broadening.

As a consequence of the finite slit widths and apertures encountered by light passing through a spectrometer even a purely monochromatic light source will acquire some measured spectral width. This instrumental broadening can be reduced by using smaller slit widths and estimated by measuring the spectral linewidth of a highly monochromatic light source

such as a single plasma line excitation from a gas discharge tube or laser. In any case, the broadening is usually independent of sample temperature and other experimental variables and the intrinsic sample linewidth can be obtained by deconvoluting the observed lineshape with the instrumental response. If both the observed and instrumental lineshapes are approximately Lorentzian then the intrinsic linewidth of the sample can be obtained by simply subtracting the instrumental linewidth from the observed linewidth [84J]. The remaining sources of linewidth and lineshape are characteristic of the the sample under investigation and will now be considered separately.

2.6 Disorder induced broadening and the Equation of Motion method

In order to determine the first order Raman spectrum of an arbitrary collection of harmonically coupled atoms it is useful to write the Stokes Raman cross-section as given by equation 2.13 in the following form:

$$\frac{d^2\sigma}{d\omega\, d\Omega} = \frac{\omega_L \omega_s^3}{c^4} \hbar \frac{[n(\omega)+1]}{2\omega} G(\omega) \qquad (2.16),$$

where $\omega > 0$, and

$$G(\omega) = \sum_j |\vec{\eta}_L \ddot{P}^1_{\alpha\beta}(j) \vec{\eta}_s|^2 \{\delta(\omega - \omega_j) + \delta(\omega + \omega_j)\} \qquad (2.17).$$

In equation 2.17 the summation is over normal coordinates, Q_j, $\ddot{P}^1_{\alpha\beta}(j)$ is the 3×3 polarizability tensor, $\left\{\frac{\partial P_{\alpha\beta}}{\partial Q_j}\right\}_o$, and $\vec{\eta}_L, \vec{\eta}_s$, are polarization vectors of the incident and scattered light respectively. The atomic displacements, $u_{i,\alpha}(t)$, may be related to the normal coordinates, $Q_j = q_j \cos\omega_j t$, through the relation

$$u_{i\alpha}(t) = m_i^{-1/2} \sum_j U_j(i\alpha) Q_j(t) \tag{2.18},$$

where $U_j(i\alpha)$ is the unitary transformation matrix and m_i is the mass of the ith atom. Using equation 2.18 it is possible to express the polarizability tensor $\tilde{\tilde{P}}^1_{\alpha\beta}(j)$ in the following form:

$$\tilde{\tilde{P}}^1_{\alpha\beta}(j) = \sum_{i\gamma} D^{\alpha\beta}_{i\gamma} \frac{U_j(i\gamma)}{m_i^{1/2}} \tag{2.19},$$

where

$$D^{\alpha\beta}_{i\gamma} = \left\{ \frac{\partial P_{\alpha\beta}}{\partial u_{i\gamma}} \right\}_o \tag{2.20}.$$

In addition, for computational purposes, it is useful to utilize the following delta function representation:

$$\delta(x) = \lim_{\substack{\lambda \to 0^+ \\ T \to \infty}} \frac{1}{\pi} \int_0^T \cos(xt) \exp(-\lambda t^2) dt \tag{2.21}.$$

Combining equations 2.17 through 2.21 with some algebraic manipulations gives

$$G(\omega) = \lim_{\substack{\lambda \to 0^+ \\ T \to \infty}} \frac{2}{\pi} \int_0^T \sum_{i,\alpha} A_{i\alpha} u_{i\alpha}(t) \{\cos \omega t\} \exp(-\lambda t^2) dt \tag{2.22},$$

provided that the initial conditions are chosen to be

$$u^o_{i\alpha} \equiv u_{i\alpha}(t=0) \equiv \sum_{\gamma\beta} \eta^\beta_L \eta^\gamma_s \frac{D^{\gamma\beta}_{i\alpha}}{m_i} \tag{2.23a},$$

$$\dot{u}_{i\alpha}(t=0) \equiv 0 \tag{2.23b},$$

and

$$A_{i\alpha} \equiv m_i u^o_{i\alpha}. \tag{2.23c}.$$

The first order Raman cross-section can now be obtained by solving the appropriate equations of motion for the time dependent atomic

displacements, $u_{i\alpha}(t)$, with initial conditions 2.23a and 2.23b, and substituting into equations 2.22 and 2.16. This equation of motion technique was developed by Beeman and Alben [77Bb] and can be applied to any collection of harmonically coupled atoms, whose equations of motion are of the form

$$m_i \frac{d^2 u_{i\alpha}}{dt^2} = \sum_{j\beta} V_{i\alpha,j\beta} u_{j\beta} \qquad (2.24),$$

$V_{i\alpha,j\beta}$ being the second derivative of the elastic energy with respect to the iα and jβ displacements. In any actual numerical calculations an upper limit T is used in equation 2.22, which is chosen so that contributions to the integral are negligible for t > T. In addition a finite value of λ is used, which gives through equation 2.21, a Gaussian peak with an approximate linewidth (FWHM (full width at half maximum)) of 3.3λ in place of a delta function. The linewidth, 3.3λ, of a single normal mode is chosen to approximate the average experimentally observed single mode linewidth due to processes not included in the harmonic approximation (equation 2.24) such as anharmonic interactions between phonons for instance.

This method is particularly useful in determining the approximate Raman spectra of disordered systems since no pre-existing symmetries are required and the method can be applied to systems with any degree of disorder provided that the interactions between atoms are harmonic (equation 2.24). As has been mentioned previously, disorder leads to a loss of translational symmetry which in turn weakens the $\vec{k} = \vec{0}$ selection rule. At low levels of disorder this can result in the effective broadening and shifting of modes, and the presence of additional modes which are not present or Raman active in the spectra of the perfect crystal.

2.7 Anharmonic effects

All discussions up to this point have assumed that the scattering medium consists of harmonically coupled atoms whose vibrational states can be described in terms of normal modes. Such normal modes can be treated as independent harmonic oscillators. Quantum mechanically each oscillator with frequency ω and energy E above the ground state corresponds to n phonons each of energy $\hbar\omega$, such that $E = n\hbar\omega$. The independence of the normal modes implies that phonon-phonon interactions are absent. Assuming a lack of additional interactions between the phonons and other excitations then implies that the phonons possess an infinite lifetime. Any technique such as light scattering which probes the phonons in the frequency domain is therefore predicted to give rise to delta functions at the phonon energies.

For many materials the adiabatic approximation is justified and the direct decay of phonons into electronic excitations can be neglected. Under these circumstances the lifetime of a phonon is primarily limited by interactions with other phonons. Such interactions are due [62K] to anharmonic terms, V_A, in the interatomic potential energy V. Since the anharmonic terms are assumed small, transition rates for phonon-phonon scattering events can be determined through second order perturbation theory and matrix elements of the form $< v_f | V_A | v_i >$. The potential energy of a crystal due to atomic displacements can be expanded as a Taylor series in powers of the atomic displacements about equilibrium positions. The cubic and higher order terms in such an expansion combine to give V_A after transforming atomic displacements, u_n, into normal coordinates, Q_n, and

expressing Q_n in terms of creation and annihilation operators. To a good approximation only the cubic and quartic terms need to be considered in V_A since the higher order terms rapidly decrease in magnitude.

The net effect of these anharmonic terms is to add a complex self energy to the bare phonon energy [84M]. As a result, the harmonic frequency of a phonon, ω_o, is replaced by a complex frequency which is given approximately by

$$\omega = \omega_o + \Sigma_1 - i\Sigma_2 \qquad (2.25),$$

assuming $|\Sigma_1|,|\Sigma_2| << \omega_o$. This transforms the original delta function contribution to the Raman spectrum, centered at ω_o, into a Lorentzian with a shifted peak position of $\omega_o + \Sigma_1$, and a linewidth (HWHM (half width at half maximum)) given by Σ_2. The lineshape of the Stokes Raman peak therefore becomes

$$I_s(\omega) = \frac{I_o}{\frac{(\omega_o + \Sigma_1 - \omega)^2}{\Sigma_2^2} + 1} \qquad (2.26).$$

The temperature dependence of this lineshape can be approximately determined through the temperature dependences of the self energy parameters Σ_1 and Σ_2. In general these self energy contributions increase in magnitude with temperature. The linewidths of anharmonically broadened phonons usually increase with temperature while frequencies normally decrease. In principle, equation 2.26 should be multiplied by the Bose factor $n(\omega)+1$ for temperatures, T, greater than 0 K as required by the fluctuation-dissipation theorem [89P]. For the phonons and temperatures investigated in this thesis, however, $n(\omega)+1$ is a slowly varying function of frequency and has been approximately taken into account through the fitting parameter I_o.

In second order perturbation theory both cubic and quartic terms in the anharmonic potential contribute to the frequency shift, Σ_1, while only the cubic term contributes to the change in linewidth Σ_2 [92W]. A quantitative analysis of the linewidth contributions due to cubic anharmonicity has been carried out by Klemens [66K]. A typical decay process due to cubic anharmonicity for zone center phonons involves the destruction of a phonon with frequency ω, and the creation of a pair of phonons whose frequencies sum to ω and wavevectors sum to zero [60K]. In Klemen's model [66K] the optical phonon is assumed to decay into a pair of acoustic phonons each of which has a frequency of $\omega/2$. In addition, the acoustic phonons are assumed to belong to the same branch in the phonon dispersion curve. Although this assumption ignores contributions from decay channels involving different branches, it does lead to a simple analytic expression for the temperature dependence of the linewidth;

$$\Sigma_2 = \Sigma_o\left[1+2n(\omega_o/2)\right]+B \qquad (2.27).$$

The constant B takes into account other residual sources of line broadening which are assumed to be independent of temperature (e.g. disorder, or decay channels which do not vary significantly with temperature). For many materials where anharmonic interactions dominate phonon scattering processes, equation 2.27 can be used as a good first approximation for the phonon linewidth temperature dependences below 300 K [84M]. Similar expressions can also be derived for the temperature dependences of the phonon frequencies but these generally require a detailed knowledge of the thermal expansion properties of the material in question. In any case, the phonons discussed in this thesis have energies greater than 300 cm^{-1} so that Bose factors such as $n(\omega_o/2)$ are approximately constant below 60 K.

Anharmonically induced phonon linewidth and frequency shifts between 100 K and 15 K are therefore expected to be small in this temperature range.

2.8 The Fano effect

Interactions between phonons and other excitations can also lead to self energy corrections. Of particular interest is the case of a single Raman active phonon interacting with a Raman active continuum as shown in Fig. 2.1. T_p and T_e are the Raman matrix elements for phonon and continuum scattering respectively, and the interaction is in the form of a matrix element, V, coupling the phonon state, $|p\rangle$, to the states, $|e\rangle$, of the continuum.

This phonon-continuum interaction results in the interference of Raman amplitudes for first order transitions, $|g\rangle$ to $|e\rangle$, and Raman amplitudes for indirect second order transitions, $|g\rangle$ to $|p\rangle$ to $|e\rangle$. Such interference effects result in an asymmetric phonon lineshape accompanied by anti-resonances on either the high or low energy side of the phonon peak. Interference effects of this kind are quite general and can be observed in many systems [69J] [70S] [91O] where a discrete state interacts with a continuum of states in the manner described above. This explanation was in fact first proposed by Fano [74F] to explain asymmetries in atomic absorption spectra. It is therefore common to refer to such asymmetries as Fano effects and corresponding spectral lineshapes as Fano lineshapes and this terminology will be used throughout this thesis.

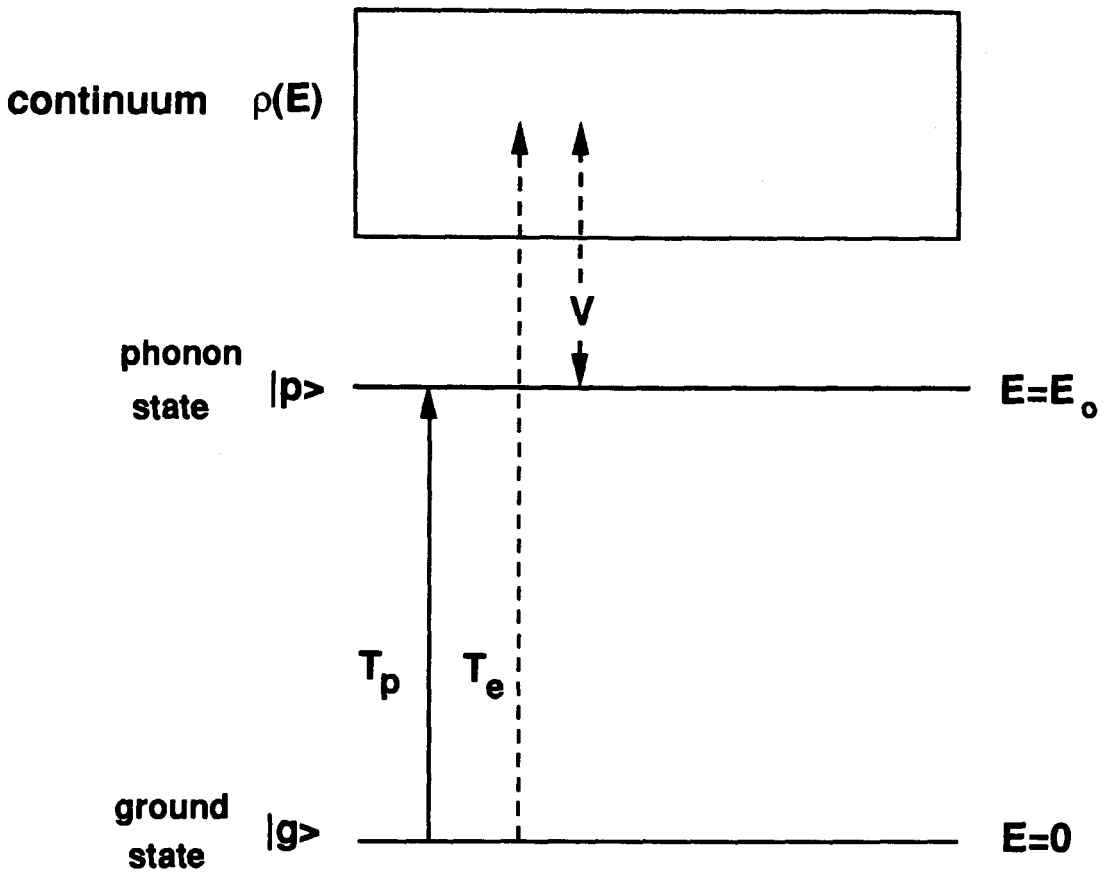

Figure 2.1

Energy levels and Raman transitions involved in the Fano effect. T_p and T_e are the Raman amplitudes for scattering from the phonon state and continuum states respectively, and V is the matrix element coupling the phonon state to the states of the continuum.

A derivation of the Raman Fano lineshape corresponding to a Raman active phonon coupled to a Raman active continuum has been carried out by Klein [81K] assuming constant transition matrix elements V,T_e, and T_p. The resulting expression can be cast in the following form:

$$\boxed{I(\omega) = I_o \frac{(q+\varepsilon)^2}{1+\varepsilon^2}} \qquad (2.28).$$

If the density of states for the continuum can be taken as approximately constant over the energies of interest, i.e. $\rho(E) \sim \rho_o$, then the parameters in equation 2.28 can be expressed as follows:

$$I_o = \pi \rho_o T_e^2 \qquad (2.29a),$$

$$\varepsilon = \frac{(\omega - \omega_o)}{\Gamma} \qquad (2.29b),$$

$$\Gamma = \pi \rho_o V^2 \qquad (2.29c),$$

$$q = \frac{T_p}{\pi \rho_o V T_e} \qquad (2.29d),$$

where ω_0 is the bare phonon frequency.

A set of Fano lineshapes is shown in Fig. 2.2. The effect of the phonon-continuum interaction is therefore in the form of a phonon self energy linewidth contribution, Γ, and a lineshape parameter q. Interestingly, in the case where Raman scattering from the continuum vanishes, that is when $T_e \to 0$ ($\Rightarrow |q| \to \infty$), equation 2.28 becomes

$$I = \frac{I_o'}{1+\varepsilon^2}, \quad I_o' = \frac{T_p^2}{\pi \rho_o V^2} \qquad (2.30),$$

which represents a Lorentzian profile. Larger magnitudes of the Fano

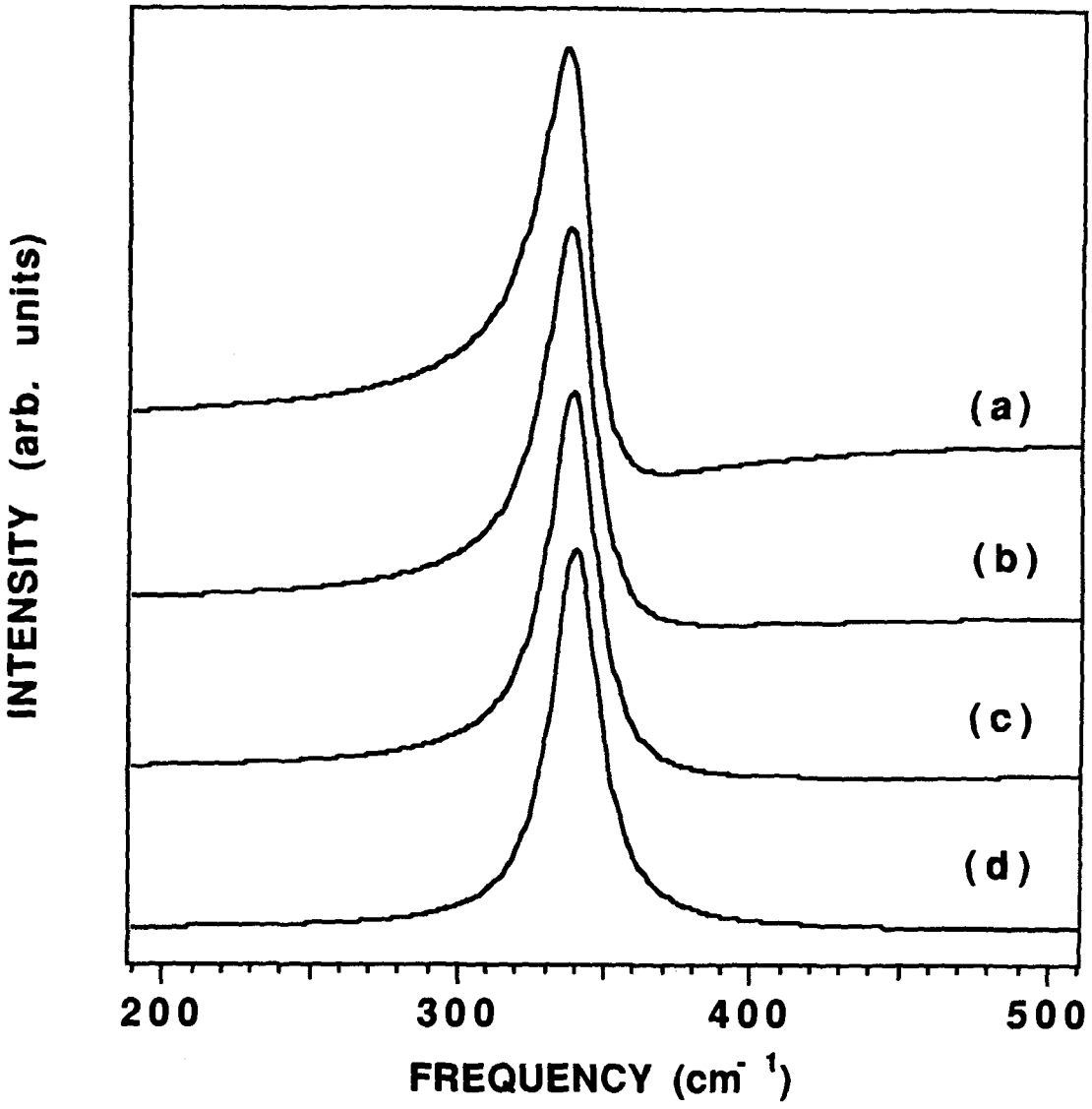

Figure 2.2

Fano profiles calculated using equation 2.28 with ω_o = 340 cm^{-1}, Γ = 10 cm^{-1}, and (a) q = -3.0, (b) q = -5.0, (c) q = -10.0, (d) q = -100.0. Note the increasing asymmetry associated with smaller magnitudes of the parameter q. The sign of the parameter q determines whether the anti-resonance falls on the high or low side of the peak maximum.

parameter, q, are therefore associated with increasingly symmetric lineshapes. Physically, $T_e \rightarrow 0$ corresponds to removing the interfering first and second order Raman amplitudes for continuum scattering. The phonon-continuum interaction, however, is still present resulting in a self energy contribution which is manifested in a finite linewidth Γ. Note that when fitting equation 2.28 to experimental data, the resulting linewidth Γ (HWHM) may contain the effects of other decay processes in addition to the phonon-continuum interaction discussed above.

Also, as for the Lorentzian profile (equation 2.26), the fluctuation-dissipation theorem for Raman scattering [78H] [89P] requires that the Fano profile (equation 2.28) be multiplied by the Bose function $n(\omega)+1$ for temperatures greater than 0 K. This has been approximately taken into account by allowing I_0 to be an adjustable parameter in any fits of equation 2.28 to experimental Raman peaks. In addition, in any fits to experimental data, equations 2.26 and 2.28 are combined with adjustable linear or constant backgrounds.

For this thesis, fitting of equations 2.26, 2.27, and 2.28 to experimental data was carried out numerically using non-linear least squares algorithms which adjust the fitting parameters until a minimum in $\sum_{i=1}^{N}\{y_i - z_i(a_1,\ldots a_m)\}^2$ is found (N = number of data points, y_i = value of the ith experimental data point, z_i = corresponding value of analytic expression to be fitted, $a_i,\ldots,a_m$ = fitting parameters).

2.9 Superconductivity-induced Self Energy Effects

From the viewpoint of this thesis the most interesting contributions to the phonon self energy result from interactions with superconducting charge carriers in the form of Cooper pairs. In standard BCS-like superconductors an energy gap, Δ, separates the superconducting ground state from the excited states of the electron system [85B]. This results in a restructuring of the Fermi surface [85B]. In particular, a gap in the quasi-particle density of states forms which is centered on the Fermi energy and has a width of 2Δ. In addition, the density of states becomes sharply peaked at the boundaries of this gap i.e. at energies, Δ, above and below the Fermi energy E_f [90Tb]. States with energies less than E_f-Δ form the superconducting Cooper pairs while the states with energies greater than E_f+Δ comprise the quasi-particle excited states. A phonon with energy just above the superconducting gap energy, i.e. $\omega_o \geq 2\Delta$, should therefore be able to scatter significant numbers of Cooper pairs into quasi-particle excited states provided that a sufficient electron-phonon coupling exists. This phonon decay channel should therefore result in a broadening of the phonon lineshape at temperatures below the critical temperature T_c. Similarly since energy levels of interacting excitations tend to repel, phonons with energies greater than 2Δ should harden or increase in frequency while phonons with energies less than 2Δ should soften or decrease in frequency below T_c.

These effects can be described in terms of superconductivity induced contributions or changes to the phonon self-energy:

$$\Delta\Sigma_v = \Delta\Sigma_1 - i\Delta\Sigma_2 \qquad (2.31),$$

which can be obtained in a quantitative manner using BCS [84K] or strong coupling theories [90Z]. In both cases, the superconductivity induced change in the phonon self energy can be written in the form [92T]:

$$\Delta\Sigma_\nu = \omega_\nu \lambda_\nu f(\tilde{\omega}) \qquad (2.32),$$

where ω_ν is the bare phonon frequency, λ_ν is the electron-phonon coupling constant for the vth phonon mode and f is a universal function of the scaled frequency, $\tilde{\omega} \equiv \frac{\omega}{2\Delta}$. The coupling constant for the nth mode, λ_ν, in equation 2.32 is given by

$$\lambda_\nu = \frac{2N(0)\left\langle |g_{\nu kk'}|^2 \right\rangle_{FS}}{\omega_\nu} \qquad (2.33),$$

where $2N(0)$ is the density of states at the Fermi surface in the normal state and $\left\langle |g_{\nu kk'}|^2 \right\rangle_{FS}$ is the square of the electron-phonon matrix element averaged over the normal state Fermi surface.

In the weak coupling BCS limit ($\lambda << 1.0$) the universal function $f(\tilde{\omega})$, can be described [92T] analytically as follows for $\vec{k} = \vec{0}$ phonons:

$$f(\tilde{\omega}) \equiv \begin{cases} -2u/\sin(2u) & ;\sin(u) \equiv \tilde{\omega} < 1 \\ (2v - i\pi)/\sinh(2v) & ;\cosh(v) \equiv \tilde{\omega} > 1 \end{cases} \qquad (2.34).$$

A plot of the real and imaginary parts of $f(\tilde{\omega})$ corresponding to the changes in phonon frequency and linewidth are shown in Fig. 2.3.

In the strong coupling limit [90Z] [92Mb] the divergences occurring at frequencies near the superconducting gap energy, 2Δ, are broadened and replaced by extrema which occur slightly above $\tilde{\omega} = 1$. In addition, in the strong coupling limit the function $f(\tilde{\omega})$ depends explicitly on temperature (T/T_c), and an impurity scattering rate $1/\tau$. Both the real and imaginary parts of $f(\tilde{\omega})$ in the strong coupling limit have been calculated by Zeyher and Zwicknagl [90Z] who assumed a total coupling constant of $\lambda_{total} = 2.9$ in order

to be consistent with a transition temperature of 90 K for $YBa_2Cu_3O_7$. Some of the results of their calculations are shown in chapter six.

In principle an estimate for the superconducting gap energy, 2Δ, can now be obtained by comparing the superconductivity induced shifts in phonon frequencies and linewidths below T_c to the results of these strong coupling calculations. The validity of this approach depends on whether such strong coupling calculations can be used to describe the electron-phonon interaction. This does not require that the electron-phonon interaction be responsible for the onset of superconductivity, or the existence and value of the superconducting gap. In principle the phonon self energy shifts can be used to probe the superconducting gap generated by some addition interaction or excitation.

Finally, it has been shown [84M] that the frequency dependence of the real part of the self energy, $\Delta\Sigma_1$, leads to a measured linewidth, Σ_2', which in principle may differ from the true linewidth, Σ_2. The relationship between these two quantities is given by [90Fb]

$$\Sigma_2' = \frac{\Sigma_2}{1-(\frac{d\Delta\Sigma_1}{d\omega})_{\omega_\nu}} \qquad (2.35).$$

The amount of dispersion in $\Delta\Sigma_1$ is usually small so that $\Sigma_2' \approx \Sigma_2$. For phonons with energies slightly less than a BCS like superconducting gap, however, this is not the case as indicated by the solid line in Fig. 2.3.

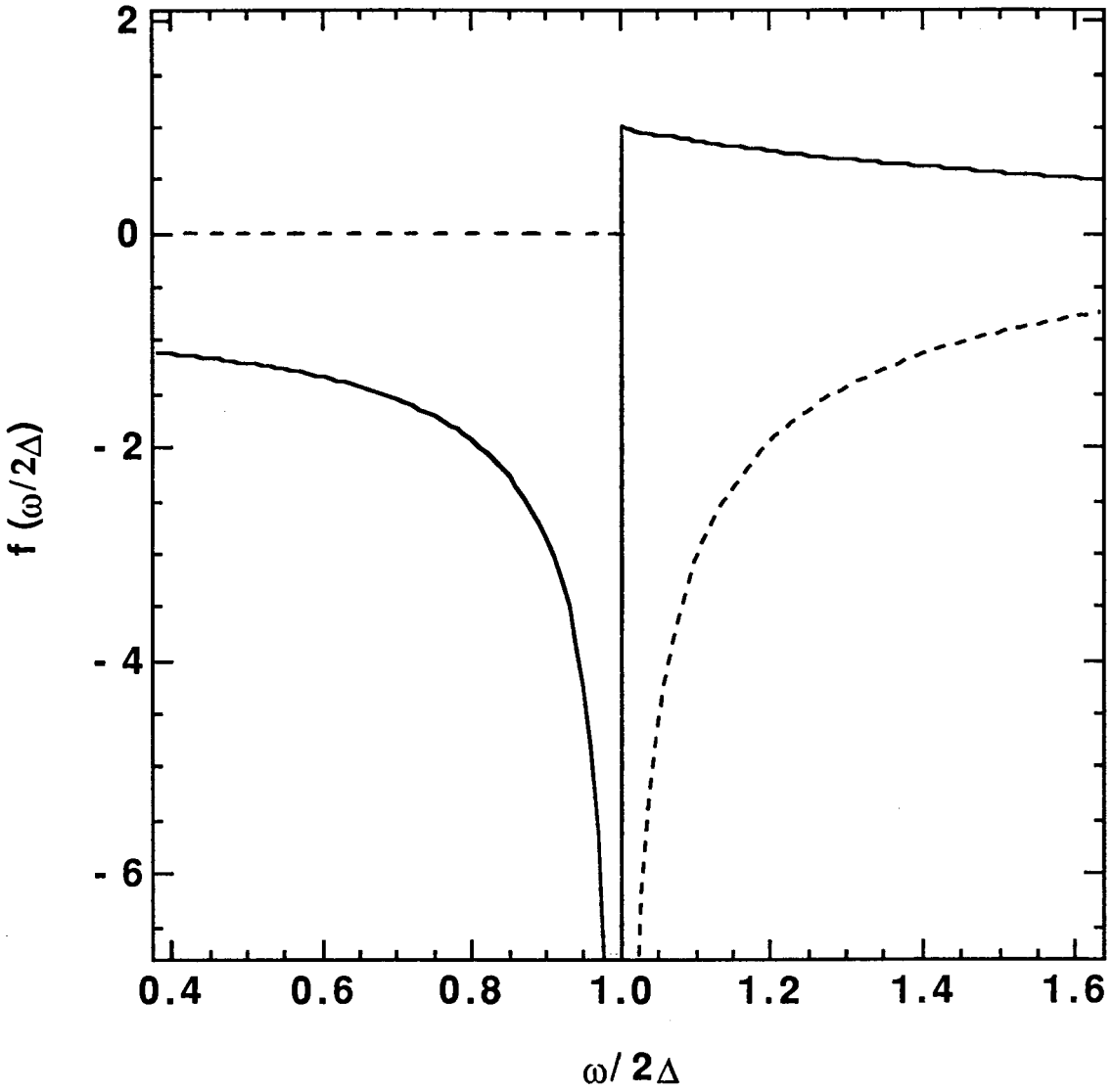

Figure 2.3

Real (solid line) and imaginary (dashed line) parts of the universal BCS function $f(\tilde{\omega})$ (equation 2.34), corresponding to the superconductivity induced self energy corrections to the $\vec{k} = \vec{0}$ phonon frequency and linewidth respectively.

CHAPTER 3
RAMAN PROPERTIES OF $YBa_2Cu_3O_7$

3.1 $YBa_2Cu_3O_7$ crystal structure and phonon symmetries

The space group for stoichiometric $YBa_2Cu_3O_7$ is Pmmm (D_{2h}) using standard short and Schoenflies notation [89T]. The corresponding crystal structure is orthorhombic and has a unit cell of N = 13 atoms as shown in Fig. 3.1. The Cu(2), O(2), and O(3) atoms make up the superconducting CuO_2 planes while the O(1) and Cu(1) atoms form the CuO chains which are thought to act as charge reservoirs [89Ga]. Between the CuO chains and CuO_2 planes are the O(4) atoms commonly referred to as apical or bridging oxygen atoms. The size of the unit cell is given by the lattice constants [89T] which for this structure are a = 3.822 Å, b = 3.891 Å and c = 11.677 Å.

The $\vec{k} \approx \vec{0}$ long wavelength vibrational modes of the $YBa_2Cu_3O_7$ crystal are given by the 3N = 39 normal modes of the unit cell. Since the space group for this structure is symmorphic, classification of these normal modes in terms of symmetry can be achieved by determining the number of modes that transform as each irreducible representation of the D_{2h} point group of the unit cell (see chapter 2). In Mulliken or chemical notation, the resulting classification can be written [89T]:

$$\Gamma_{vib} = 5A_g + 5B_{2g} + 5B_{3g} + 8B_{1u} + 8B_{2u} + 8B_{3u} \qquad (3.1),$$

where the 15 modes denoted with the subscript g (gerade) are even with respect to inversion symmetry while the 24 remaining u (ungerade) modes are odd with respect to inversion symmetry. Since the unit cell has a center of inversion, only the 15 even (g) modes are Raman active. Of the remaining 24 odd u modes three are acoustic (B_{1u}, B_{2u}, B_{3u}) and 21 are infrared (IR) active. Experimentally the $5A_g$ modes are the dominant features in most of the

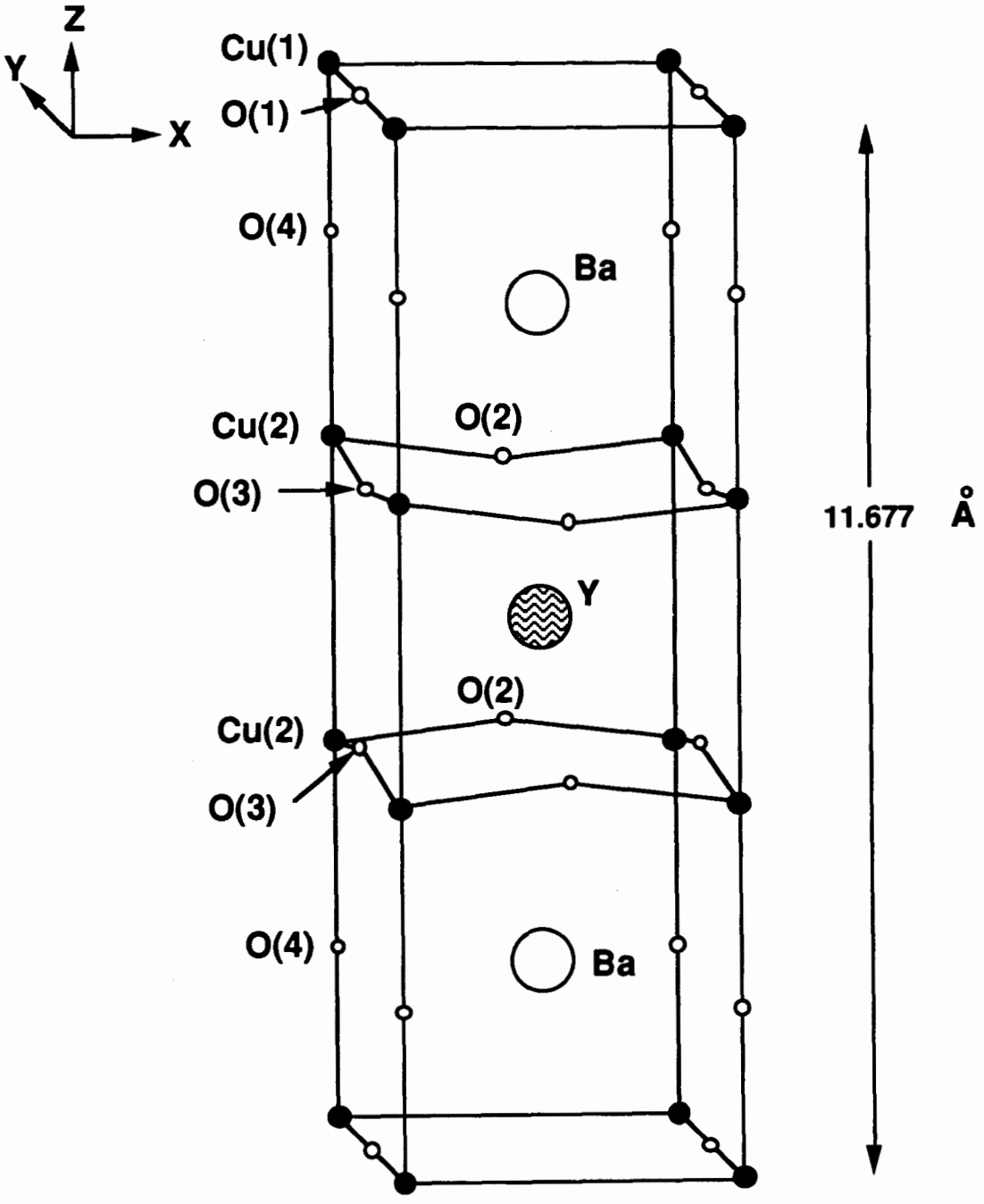

Figure 3.1

$YBa_2Cu_3O_7$ unit cell.

Raman spectra of this compound. A typical Raman spectrum taken from a ceramic pellet of $YBa_2Cu_3O_7$ is shown in Fig. 3.2. The dominant features at approximately 115, 150, 340, 440, and 500 cm^{-1} are generally accepted to be due to the $5A_g$ phonon modes.

The weaker B_{2g} and B_{3g} modes have been identified by McCarty et al. [90Ma] in spectra of untwinned single crystals using scattering geometries consistent with the symmetries of these modes. The dominant $k \approx 0$ $5A_g$ modes have the full symmetry of the D_{2h} point group and hence involve displacements of the Ba, Cu(2), O(2), O(3), and O(4) atoms along the c-axis of the crystal. Details of the eigenmode atomic displacement patterns, and values for the eigenfrequencies which correspond to these modes cannot, however, be determined from group theoretical considerations alone. A number of dynamical models [87Bb] [88Ka] [88Kb] [88Lb] [89B] have been used to estimate the $\vec{k} \approx \vec{0}$ eigenmodes and eigenfrequencies. The simplest approaches involve modelling the atoms and interatomic bonds by masses and harmonic springs respectively [87Bb] [89B]. More sophisticated shell models [88Ka] [88Kb] [88Lb] assume that the outer valence electrons of a given atom can be modelled by a massless shell which is coupled to both the ionic core of the same atom and the shells and cores of other atoms. Usually these shell model calculations assume interatomic force constants that are obtained from the known parameters of simpler related oxides [88Lb]. The results of such lattice dynamics calculations consistently predict the atomic displacement patterns shown in Fig. 3.3 for the $\vec{k} \approx \vec{0}$ A_g eigenmodes. Note in particular that while the 115 and 150 cm^{-1} modes are due to the motion of the Ba and Cu(2) atoms respectively the 340, 440, and 500 cm^{-1} modes are entirely the result of vibrations among the oxygen atoms. Of the three high energy modes the 340 and 440 modes are predicted to be due to the

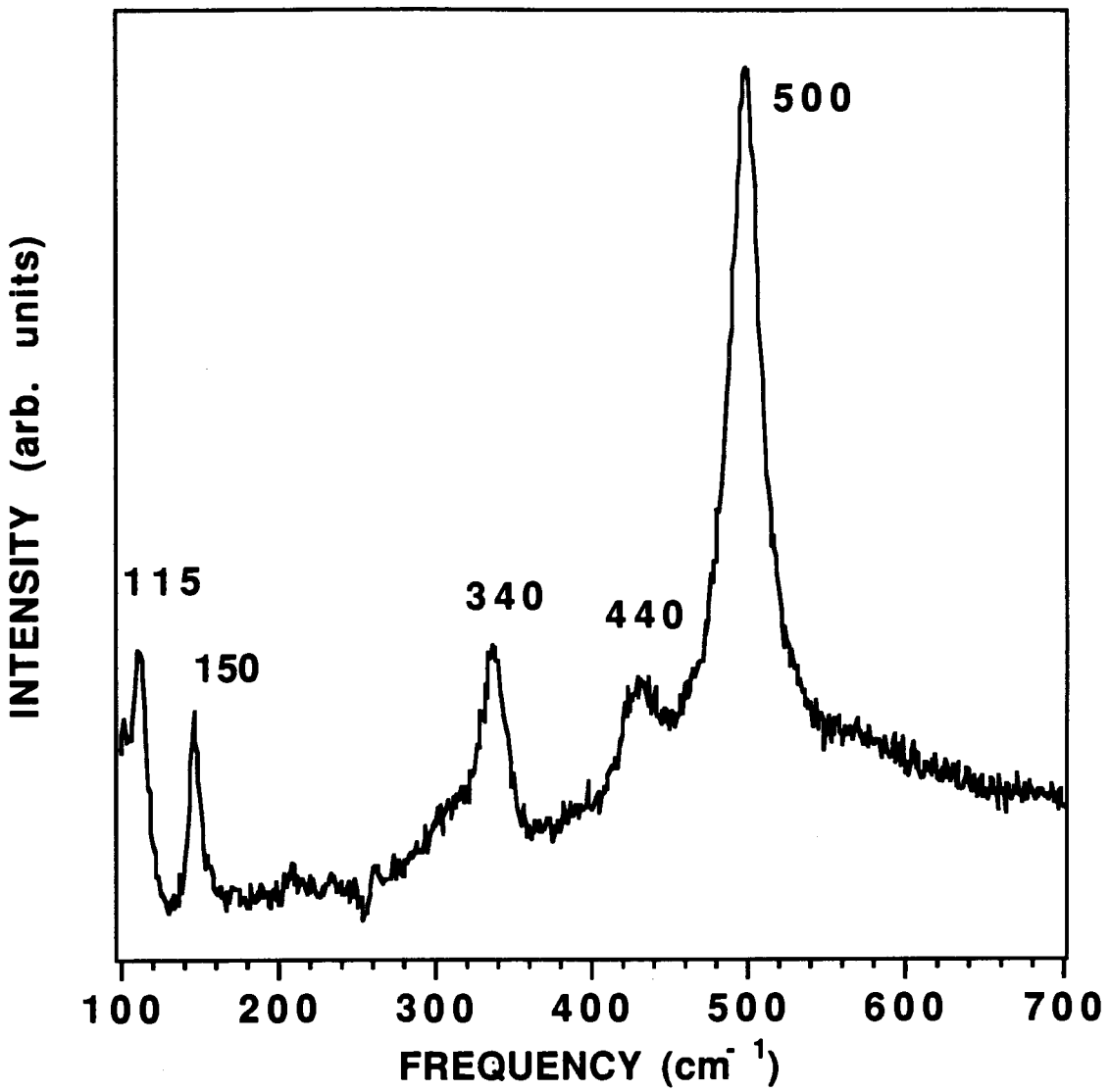

Figure 3.2

Raman spectrum of a polycrystalline sample of $YBa_2Cu_3O_7$. Peaks in the spectrum are due to the five A_g phonon modes discussed in the text (nominal frequencies in cm^{-1} are indicated by bold face numbers).

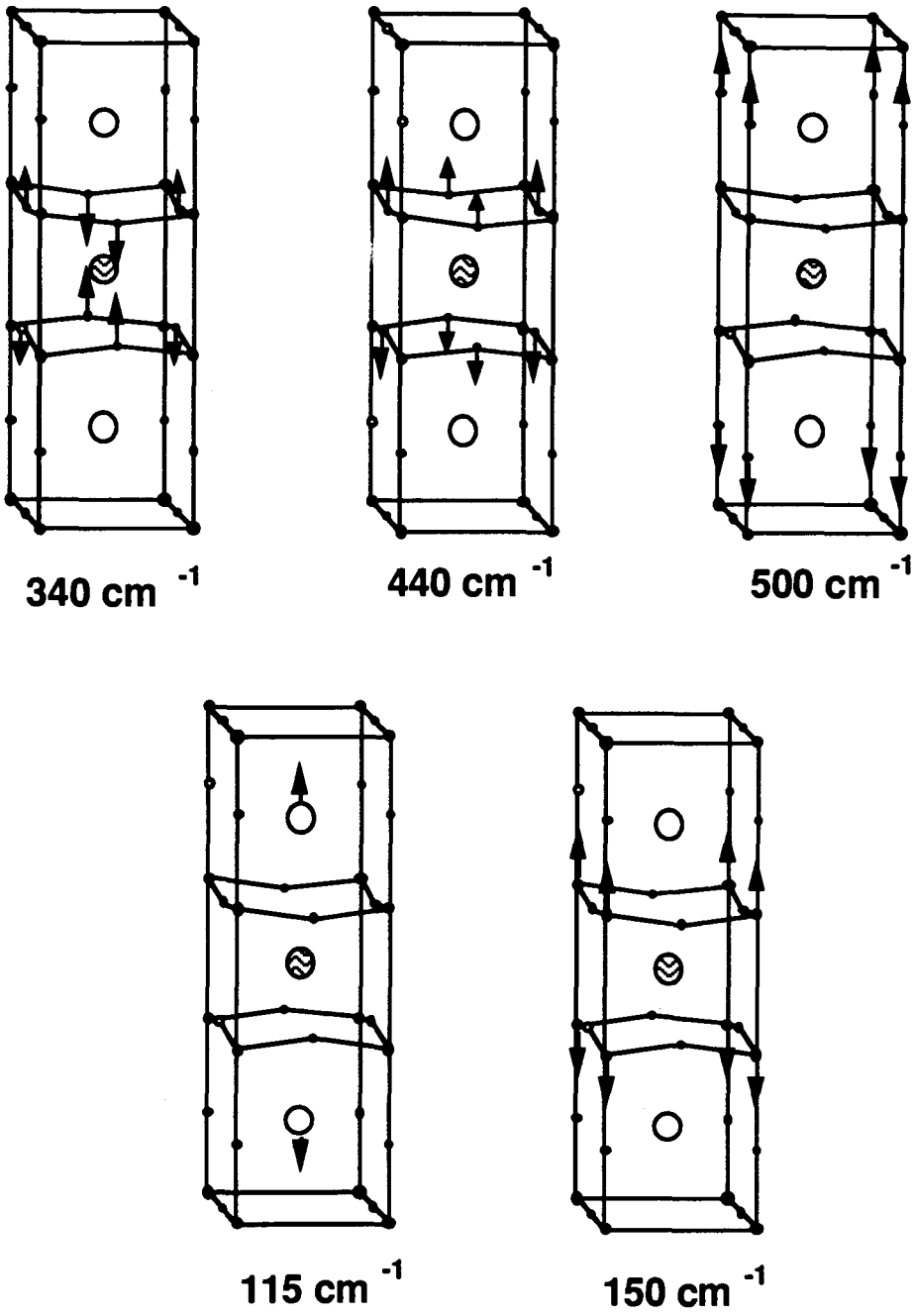

Figure 3.3

Atomic displacement patterns for five A_g Raman modes as determined by shell model calculations [88Lb]. The three oxygen dependent vibrations are shown at the top of the figure.

motion of the O(2) and O(3) planar oxygen atoms while the 500 cm^{-1} mode is predicted to involve only the O(4) oxygens bridging the CuO_2 planes and CuO chains.

An additional method that has been used to determine the A_g eigenmodes involves carrying out band structure calculations. In these LDA (local density approximation) frozen phonon calculations [90Ta] [90R] [90C] the total energies, E, are self consistently determined for all possible A_g displacement patterns $d(z_{Ba}, z_{Cu(2)}, z_{O(2)}, z_{O(3)}, z_{O(4)})$. The phonon eigenmodes are then determined from the eigenvectors of the dynamical matrix $\frac{\partial^2 E}{\partial z_i \partial z_j} \times \frac{1}{\sqrt{M_i M_j}}$, where M_i and M_j are the atomic masses. This approach predicts that the O(2), O(3), and O(4) atoms all have significant and comparable amplitudes of vibration for all three A_g phonon modes at 340, 440 and 500 cm^{-1}. In particular, the 340 and 440 cm^{-1} modes involve motion of the bridging O(4) oxygens in addition to the O(2) and O(3) planar oxygen displacements predicted by the shell model calculations, and the 500 cm^{-1} mode involves motion of the planar oxygen atoms in addition to the O(4) atoms. This is often referred to as a mixing or hybridization of the 500 cm^{-1} mode with the planar 340 and 440 cm^{-1} modes.

In this thesis, the consequences of oxygen isotope substitution on the Raman spectra of the A_g modes will be presented and analyzed. The results obtained suggest that the degree of hybridization predicted by the LDA calculations [90C] may be overestimated and that the atomic displacement patterns predicted by the shell model calculations [88Lb] (Fig. 3.3) are consistent with the experimental observations.

In order to better understand the symmetry properties of the A_g eigenmodes it is worthwhile to consider the semiconducting stoichiometric

$YBa_2Cu_3O_6$ compound. The unit cell corresponding to this material has tetragonal symmetry [89T] and is similar to the orthorhombic unit cell shown in Fig. 3.1 except that in the tetragonal cell the O(1) chain atoms are absent. The tetragonal cell has a higher degree of symmetry than its orthorhombic counterpart, in particular, the four edges of the CuO_2 planes (i.e. a and b axes) in the tetragonal unit cell are equivalent. This fourfold symmetry implies that for a given phonon mode, the displacement amplitudes of the oxygen atoms on the four edges must be equivalent since they are related by a fourfold rotation. As a result, the symmetries of the planar oxygen modes are distinct in the tetragonal compound. In particular, the normal mode corresponding to the 340 cm^{-1} mode in the orthorhombic compound has B_{1g} symmetry [89T] while the mode corresponding to the 440 cm^{-1} phonon has A_{1g} symmetry.

The forms of the Raman tensors corresponding to these tetragonal symmetries are given by [89T]:

$$R_{A_{1g}} = \begin{pmatrix} a & 0 & 0 \\ 0 & a & 0 \\ 0 & 0 & c \end{pmatrix} \qquad (3.2a),$$

$$R_{B_{1g}} = \begin{pmatrix} d & 0 & 0 \\ 0 & -d & 0 \\ 0 & 0 & 0 \end{pmatrix} \qquad (3.2b).$$

The intensity of scattered light due to a phonon with a Raman tensor R is given by $I \propto \left|\vec{E}_s \cdot \vec{R} \cdot \vec{E}_i\right|^2$ where $\vec{E}_i$ and $\vec{E}_s$ are the incident and scattered electric field vectors. Suitable scattering geometries (choices of $\vec{E}_i$ and $\vec{E}_s$) can therefore yield the relative magnitudes of each of the elements α_{ij} of $\vec{R}$. Note in particular that the zz element of the B_{1g} tensor is zero, implying that the corresponding B_{1g} phonon should not appear for a scattering geometry in which the incident and scattered light are both polarized in the z or c-axis

direction. The B_{1g} phonon should also yield a vanishing Raman intensity when the incident and scattered electric fields are polarized at 45° to the x (a) and y (b) axes respectively (or vice versa). In Raman light scattering experiments such selection rules may be used to identify the A_{1g} and B_{1g} phonons.

The amount of orthorhombic distortion in the $YBa_2Cu_3O_7$ unit cell is small as evidenced by the nearly equal unit cell lengths in the a and b directions. The 340 cm^{-1} A_g phonon in the nearly tetragonal $YBa_2Cu_3O_7$ compound should therefore assume a B_{1g}-like symmetry, and hence have a Raman tensor with elements given approximately by those of $R_{B_{1g}}$ (equation 3.2b). A systematic analysis [89T] of the 340 cm^{-1} phonon has shown that its corresponding Raman tensor indeed has the approximate form of $R_{B_{1g}}$, indicating B_{1g}-like symmetry. Finally, the 440 and 500 cm^{-1} modes have been shown to exhibit Raman selection rules which are consistent with their A_g symmetry assignment. Therefore in this thesis and following common usage [89T], the 340 cm^{-1} phonon will often be designated as a B_{1g} phonon (tetragonal notation) while the 440 and 500 cm^{-1} phonons will be referred to simply as A_g phonons (orthorhombic notation).

As has already been mentioned, in the semiconducting tetragonal $YBa_2Cu_3O_6$ compound the O(1) atoms shown in Fig. 3.1 are missing. Extra oxygen atoms added to this compound are found between the Cu(1) atoms and tend to order themselves exclusively along one of the planar axes thereby forming the CuO chains. By convention this axis is referred to as the b-axis [88S] which expands relative to the a-axis length as a result of the extra O(1) oxygen atoms. This lowers the symmetry of the unit cell from tetragonal to orthorhombic. To accommodate this distortion the crystals undergo a process known as twinning [88S] wherein the a and b axes interchange over a distance

which defines the size of a single domain. In a heavily twinned crystal the length scale of a single domain may be as small as 0.01 μ (micro-twinned) [88P]. Following common terminology, such twinned crystals will still be referred to as single crystals. The crystals used for the work presented in this thesis are mostly lightly twinned (1-100 μ) with the incident laser beam often spanning more than one domain. The twin domains can be observed using crossed polarizers and an optical microscope. Single domains with unique a and b axes appear as bright bands while micro-twinned areas appear dark. Typical images obtained for crystals investigated in this thesis are shown in Fig. 3.4. As a result, spectra taken from the ab faces of the crystals with the incident light propagating in the c-axis direction contain a mixture of $E_i \parallel [100]$ and $E_i \parallel [010]$ polarization geometries and will be referred to simply as (ab) spectra in this thesis. Spectra taken from the edges of the crystals with the incident light propagating in the ab plane and with the electric field polarized parallel to the c-axis ($E_i \parallel [001]$) will be referred to as (zz) spectra.

Since the orthorhombic distortion in $YBa_2Cu_3O_7$ is small the basic atomic displacement patterns of the 5 eigenmodes shown in Fig. 3.3 do not change significantly in going from $YBa_2Cu_3O_7$ to $YBa_2Cu_3O_6$. The frequencies corresponding to these modes shift by less than 10% [88Ma] with the largest shift occurring in the vibrations of the bridging O(4) oxygens. The frequency for this mode varies approximately linearly [88Ma] from about 500 cm^{-1} in the orthorhombic $YBa_2Cu_3O_7$ compound to about 480 cm^{-1} in $YBa_2Cu_3O_6$. This mode can therefore be used to estimate the approximate degree of oxygenation in crystalline or polycrystalline samples.

In addition to the $5A_g$ modes discussed so far, features at approximately 235 and 580 cm^{-1} commonly appear in spectra of partially deoxygenated $YBa_2Cu_3O_y$, $6.7 \lesssim y < 7.0$, samples. The exclusive appearance of these modes

Figure 3.4

Optical micrographs, using crossed polarizers (light incident on crystal is polarized at 90° to light which forms image) to reveal twinning, in (a) $YBa_2Cu_3O_7$ crystal grown in a thoria crucible (b) $YBa_2Cu_3O_{6.93}$ crystal grown in a zirconia crucible. Light regions correspond to domains containing unique a and b axis directions which are oriented in the plane of the page. Darker regions correspond to areas of micro-twinning. The crystal in micrograph (b) is partially detwinned with the large white region corresponding to a single domain. Scales are indicated under the micrographs.

(a)

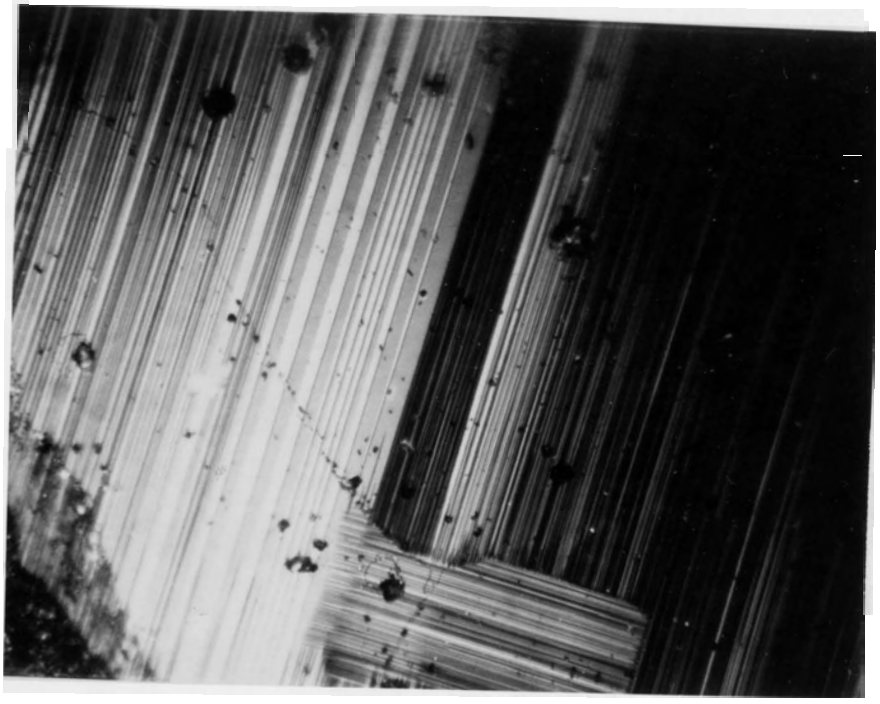

100 microns

(b)

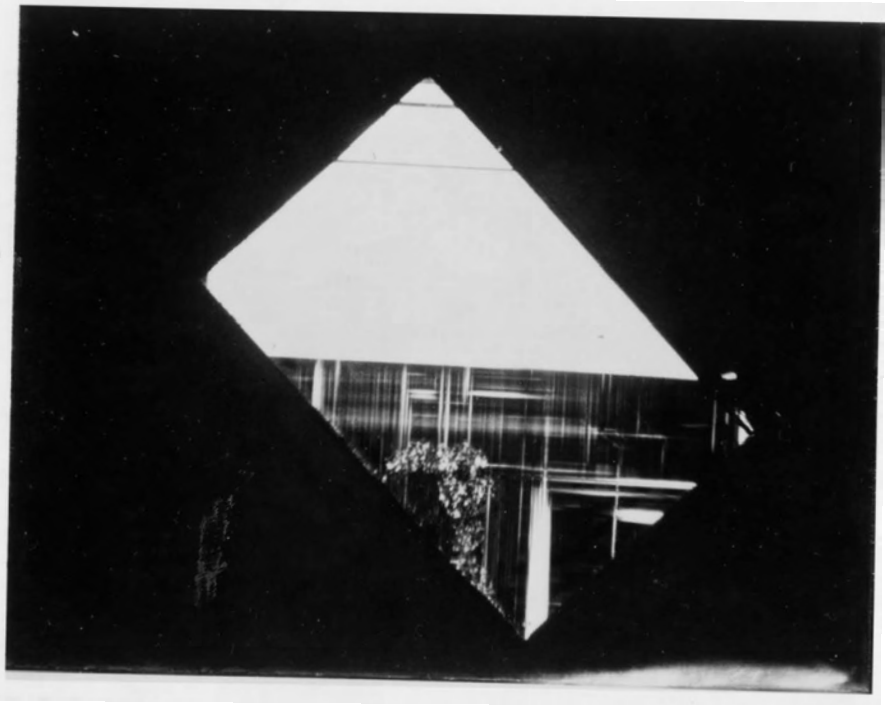

100 microns

45(b)

in the yy (bb) polarization spectra of crystals suggests that they represent intrinsic modes which are thought to be [91H] defect induced CuO chain modes. These modes appear even in nearly fully oxygenated crystals (e.g. $YBa_2Cu_3O_{6.95}$) and hence serve as sensitive indicators of the degree of oxygenation near y = 7.0.

Finally, Raman spectroscopy is also highly sensitive to small amounts of impurity phases which often cannot be detected by x-ray measurements or optical examination under a microscope. A common impurity compound found in $YBa_2Cu_3O_y$ samples is $BaCuO_2$ which produces Raman features at frequencies of approximately 580 and 640 cm^{-1} [88Lc]. These impurity phases can be distinguished from the previously mentioned defect modes by the absence of the 235 cm^{-1} defect feature and the lack of any Raman selection rules.

3.2 Electronic Scattering and Fano Lineshapes in the normal state

Having discussed the symmetries of the dominant phonon modes, it is now useful to examine the nature of the Raman spectrum for temperatures above T_c in somewhat more detail. A unique feature observed in the normal state Raman spectra of $YBa_2Cu_3O_7$ and other high temperature superconductors is a broad temperature independent background [88Cb] which is constant in amplitude and extends out to very high frequencies ($\omega > 4000\,cm^{-1}$) [91K]. This background is a general property of the high temperature cuprate superconductors [92T] and remains even after subtracting off other sources of background such as stray light and elastic scattering. More specifically, Raman background contributions with different symmetries [88Cc] can be observed in various scattering geometries. Although

some background scattering exists [90Sb] even in semiconducting $YBa_2Cu_3O_6$, increases and changes [90Sb] [91K] in the background intensity correlated with increasing oxygen or hole concentrations suggest that scattering from low lying electronic excitations may be the source of some of the background. Other potential explanations such as multi-phonon or multi-magnon processes are unlikely due to the lack of a temperature dependence for $T > T_c$ and the presence of scattering even at very high energies ($\approx 0.5\,eV$) [91K]. For polarization in the ab plane, the electronic background can be described [89Ca] in terms of a contribution which has A_{1g} symmetry (tetragonal notation) and a second contribution which has B_{1g} symmetry (tetragonal notation). A Raman background has also been observed in the zz geometry by McCarty et al [90Mb].

It is interesting to note that the electronic scattering just described cannot be due to single-particle excitations of a free electron like system. Energy conservation for scattering in such a system requires that [66P]

$$\hbar\omega_s = \hbar\omega_i - \left\{[\hbar^2(q+q_F)^2/2m] - [\hbar^2 q_F^2/2m]\right\} \qquad (3.3),$$

where ω_i and ω_s are the incident and scattered photon frequencies, q_F is the Fermi wavevector, m is the mass of the carrier (free electron or hole), and $\hbar q$ is the momentum transferred to the carrier. For maximum energy transfer q should be parallel to q_F so that equation 3.3 becomes

$$\Delta\omega_{max} = \omega_i - \omega_s = qv_F + \hbar q^2/2m \qquad (3.4),$$

where v_F is the carrier velocity at the Fermi surface. In addition, $q << q_F$ for optical phonons so that $\Delta\omega_{max} \approx qv_F$. As mentioned in chapter 2, the wavevector transfer for visible light (eg. λ=514.5 nm) in $YBa_2Cu_3O_7$ is about $5\times10^5 cm^{-1}$ [92F]. Using this value for q, and typical values for v_F (eg. $v_F \approx 6\times10^7 cm/s$ [92F]), gives $\Delta\omega_{max} \approx$ 150 cm^{-1} which clearly cannot account for the electronic background observed in $YBa_2Cu_3O_7$ out to about 0.5 eV.

Note also that the phonons investigated in this thesis have energies larger than this cutoff ($\Delta\omega_{max}$), implying that there should not be any broadening of these phonons in the normal state due to coupling to free electron like quasi-particles (Landau damping).

It has also been shown [92T] that the inclusion of coulomb interactions leads to screening of the free particle excitation spectrum which further reduces the amount of electronic light scattering in the frequency range probed by the Raman experiments. Attempts to explain the electronic background within a Fermi liquid framework have therefore focussed on band structure effects. In particular, inter-valley effective mass fluctuations [92T] have been suggested as a possible explanation for the background since such fluctuations would not be screened by the free carriers. Alternatively, Monien and Zawadowski [89M] have suggested a model in which intraband transitions within the planes are responsible for the A_{1g} background while interband transitions involving bridging O(4) oxygens and CuO_2 planar oxygens are responsible for the B_{1g} background. Finally, Varma et al. [89V] have proposed a phenomenological theory in which the starting point is an electronic polarizability $P(q,\omega)$ which reproduces the essential features of the Raman background. Such a polarizability can also explain a number of other normal state properties of high T_c superconductors such as the linear resistivity and nearly temperature independent thermal conductivity. The form of the polarizability $P(q,\omega)$ assumed in this theory leads to a quasiparticle strength that vanishes logarithmically at the Fermi surface. Varma and coworkers [89V] have coined the term Marginal Fermi Liquid to describe this state.

Related to the electronic background, are the distinctly asymmetric lineshapes [92T], of the 115 and 340 cm^{-1} phonons. These lineshapes are well

represented by numerical fits to Fano profiles (equation 2.28) indicating that the observed asymmetry is most likely the result of an interaction between the phonons and a Raman active continuum. Cardona and coworkers [89Cb] have shown that the Fano lineshapes of the 115 and 340 cm^{-1} modes in $YBa_2Cu_3O_7$ transform into symmetric Lorentzian profiles in the semiconducting $YBa_2Cu_3O_6$ compound. Results presented later in this thesis will describe in detail the reduction in asymmetry of the 340 cm^{-1} mode with decreasing carrier (hole) concentration by utilizing $YBa_2Cu_3O_y$ crystals with concentrations ranging from $y \approx 7.0$ to $y \approx 6.7$. This correlation between the Fano asymmetries and the carrier concentration strongly supports suggestions that the Fano resonances observed in the 115 and 340 cm^{-1} phonon modes may be due to an interaction between the phonons and an electronic continuum that forms part or all of the the Raman background.

3.3 Superconductivity related changes in Raman spectrum of $YBa_2Cu_3O_7$

Some of the spectral features discussed in the previous sections undergo anomalous changes as the sample under investigation is cooled below the superconducting transition temperature T_c. The nature of the superconducting state of $YBa_2Cu_3O_7$ can therefore be probed by investigating the temperature dependences of these Raman features.

In the five years since the discovery of superconductivity in $YBa_2Cu_3O_7$ various groups have investigated the temperature dependences of the A_g phonon modes, and the behavior of the Raman background for temperatures above and below T_c. The superconductivity induced effects observed in the phonon modes include shifts in the phonon frequencies and linewidths, and changes in the amount of asymmetry of the spectral lineshapes. Of the five A_g

phonons (orthorhombic notation), the 340 cm^{-1} B_{1g} like mode (tetragonal notation) has exhibited the most pronounced superconductivity induced changes below T_c. Macfarlane et al. [87M] initially observed that in fully oxygenated samples of polycrystalline $YBa_2Cu_3O_7$ the 340 cm^{-1} phonon softened (decreased in frequency) by about 2% as the sample was cooled from the critical temperature (T_c) near 90K to about 10K. This result was subsequently confirmed by various groups in experiments on polycrystalline [87W] [88Cd] [88Td], thin film [88F], and single crystal samples [88Cb] [88Cc] [88Te], and furthermore it was found [88Cb] that the linewidth of this same mode increased by up to 50% when the sample was cooled below T_c. These superconductivity induced changes in the frequency and linewidth of the 340 cm^{-1} phonon in conjunction with its distinctive Fano lineshape, have provided evidence of strong electron-phonon interactions in $YBa_2Cu_3O_7$. Zeyher and Zwicknagl [90Z], motivated by these results and the implication that the energy of the 340 cm^{-1} phonon may roughly coincide with a superconducting gap energy, 2Δ, developed the strong coupling model mentioned earlier.

At this point it should be mentioned that a number of experiments carried out by various groups have essentially eliminated the possibility that the shifts observed in the 340 cm^{-1} phonon at T_c are coincidental and not related to superconductivity. Data from neutron scattering experiments [90J] for instance have shown that the structural changes that occur in the vicinity of T_c are too small to account for the observed decrease in frequency (up tp 2%) of the 340 cm^{-1} phonon. Also, temperature dependences of the corresponding B_{1g} phonons in related non-superconducting compounds such as $PrBa_2Cu_3O_7$ and $YBa_2Cu_3O_6$ indicate no evidence of softening for temperatures ranging from 300 K to 4 K [88Kc] [88Tb]. Perhaps most significant

however are experiments by Ruf et al. [88R] in which an applied magnetic field was used to lower the critical temperature T_c. In the presence of the applied field the temperature corresponding to the onset of softening of the 340 cm^{-1} phonon coincided with the reduced critical temperature.

Subsequently it was found [90Ta] [90Mb] [90A] [90Fa] [91Ab] [91Ma] that the Raman active oxygen vibrations at 440 and 500 cm^{-1} also exhibited superconductivity induced changes in frequency and linewidth. Thomsen et al. [90Ta] and Friedl et al. [90Fb] utilized the temperature dependences of the frequencies (ω_ν) and linewidths (FWHM = $2\gamma_\nu$) of the 340 and 440 cm^{-1} phonons to obtain an estimate for the superconducting gap energy, 2Δ, in several polycrystalline $RBa_2Cu_3O_7$ compounds (R is a rare earth element e.g. Y, Eu,Gd,) all of which had a critical temperature T_c of about 90K. They obtained a value of $2\Delta \approx 5.0kT_c$ (~ 313 cm^{-1}) by comparing their experimental observations to the predictions of the strong coupling model of Zeyher and Zwicknagl [90Z].

More recently, however, several experiments [91Ab] [91Ma] have been carried out on samples in which the 340 cm^{-1} linewidth exhibited a very different behavior than that observed by Thomsen et al. [90Ta] and Friedl et al. [90Fb]. In particular, for some of the $YBa_2Cu_3O_y$ (y≈7.0) crystals investigated in this thesis, the 340 cm^{-1} mode does not broaden at all (see chapter 6). This implies a significantly larger value for the superconducting gap energy ($2\Delta >$ 340 cm^{-1}) than that obtained for crystals where the 340 cm^{-1} mode does broaden [90Ta][90Fb].

McCarty et al. [91Ma] found that both the 340 and 440 cm^{-1} modes actually narrowed for $T < T_c$ and obtained an estimate of $6.8kT_c < 2\Delta < 7.7kT_c$ for the gap from measurements on untwinned single crystals. Thomsen et al. [91T] have suggested that these quite different results for the 340 cm^{-1} phonon

shifts and hence gap energies could be attributed to differences in sample quality. In particular, some of the crystals investigated in this thesis were grown in thoria crucibles and contained approximately 8700 ppm by weight of thorium, while the crystals of McCarty et al. [91Ma] contained some gold. It was suggested [91T] that these impurities could lead to a symmetrization of the gap around the Fermi surface, and under appropriate circumstances, to larger measured values for 2Δ. However, more recent investigations [91Ac] [92A] (presented in chapter 6 of this thesis) on pure crystals grown in zirconia crucibles have demonstrated that a narrowing of the 340 cm^{-1} mode occurs even in high quality crystals with very small impurity concentrations. Similar results have been obtained by McCarty and coworkers [91Mb] [92Ma]. Furthermore McCarty et al. [91Mb] found that the 440 cm^{-1} mode narrowed slightly below T_c while for one batch of crystals investigated in chapter 6, a small broadening (~ 2 cm^{-1}) is observed for this same mode.

These results imply that the temperature dependences of the Raman active oxygen vibrations in $YBa_2Cu_3O_y$ ($y \approx 7.0$) are very sensitive to relatively minor differences in the properties of the samples studied. In this thesis evidence will be presented suggesting that the origin of these variations may be found in a strong sensitivity to the hole concentration which can vary slightly from crystal to crystal without significantly altering T_c.

The electronic background discussed earlier also undergoes substantial changes as the sample becomes superconducting. Both A_{1g} and B_{1g} contributions to the (ab) spectra form broad maxima below T_c at approximately 350 and 500 cm^{-1} respectively [88Cc]. In addition, scattering at frequencies below these maxima is reduced relative to the normal state. This is qualitatively similar to although somewhat different than the electronic scattering expected in a BCS like superconductor [84K] which has a sharp

cutoff at $\omega = 2\Delta$ with no scattering at energies less than 2Δ. Such conventional electronic scattering was observed in Nb_3Sn by Hackl et al. [89Hb] and in Nb_3Sn and V_3Si by Dierker et al. [83D].

It has been suggested [88Cb] [88Cc] that the restructuring of the Raman background below T_c in $YBa_2Cu_3O_7$ corresponds to a redistribution of the electronic states associated with the onset of superconductivity. The finite scattering near $\omega = 0$ at low temperatures may reflect the presence of states within the gap, a distribution of gaps [88H] or perhaps a gap with nodes ($2\Delta = 0$) for certain symmetries or directions in k-space [88Cc]. At this point a definite statement about the origin of the electronic background cannot be made.

The reduction of the Raman background scattering at low frequencies ($\omega < 150\ cm^{-1}$) has been used [91K] to phenomenologically analyze the anomalous narrowing of the 115 cm^{-1} Ba mode at temperatures below T_c. It is assumed that the 115 cm^{-1} phonon decays into the same electronic continuum seen by the Raman scattering experiments. This results in a contribution to the phonon linewidth which is lessened below T_c due to the redistribution of electronic states to higher energies.

CHAPTER 4

EXPERIMENTAL METHODS

4.1 Experimental apparatus

For the light scattering experiments described in this thesis the incident light consisted of either the 514.5 or 488.0 nm lines of an argon ion laser (most experiments were carried out using the 514.5 nm line). A spectra physics model 365 laser was used to generate the incident beam which was focussed onto the sample using two lenses and a right angle prism. The overall experimental setup is shown in Fig. 4.1 and the focussing optics is shown in Fig. 4.2. The incident beam at the sample surface was either in the form of a focussed spot or line depending on whether a spherical or cylindrical lens was used for the lens nearest the sample (Fig. 4.2). Line focussing was used unless sample surface conditions required using smaller areas of the sample surface.

Polycrystalline samples were mounted on a copper disk approximately 19.0 mm in diameter and 4.0 mm thick using clear nail polish as the bonding agent. Similarly the single crystal samples were either mounted directly onto the copper disk (Fig. 4.3 (b)), such that the incident light was polarized in the ab plane of the crystal, or sandwiched between two copper brackets which were screwed onto the copper disk (Fig. 4.3 (a)). The latter mounting configuration allowed the incident light to be scattered from the edges of the crystals with the incident light polarized along the c-axis direction of the crystals. This in turn allowed the zz element of the Raman tensor to be studied. As mentioned in chapter 3, the 440 and 500 cm^{-1} phonon modes in $YBa_2Cu_3O_7$ have A_g symmetry (orthorhombic notation) and hence corresponding diagonal Raman tensors. In addition, the zz element of these

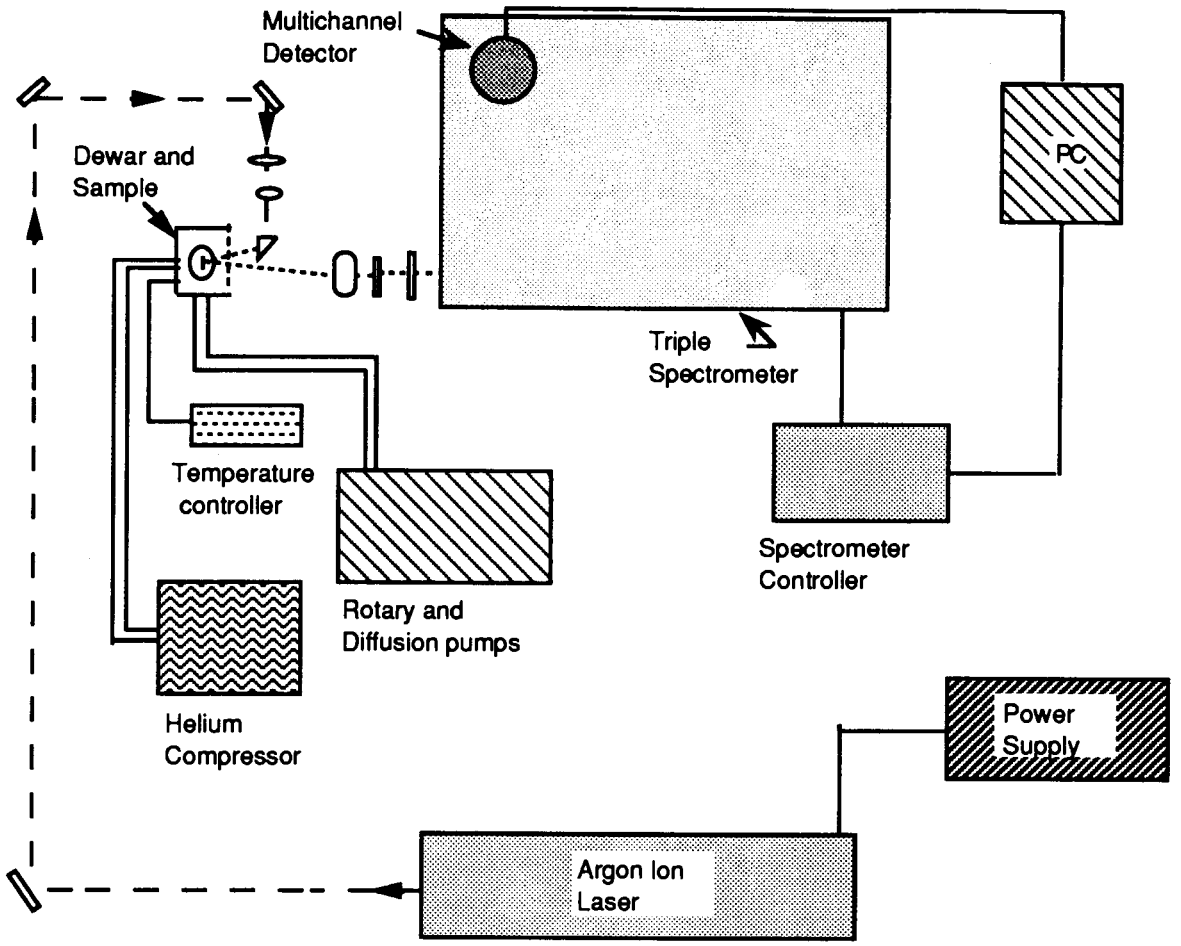

Figure 4.1

Schematic diagram of the experimental setup used to collect the data presented in this thesis.

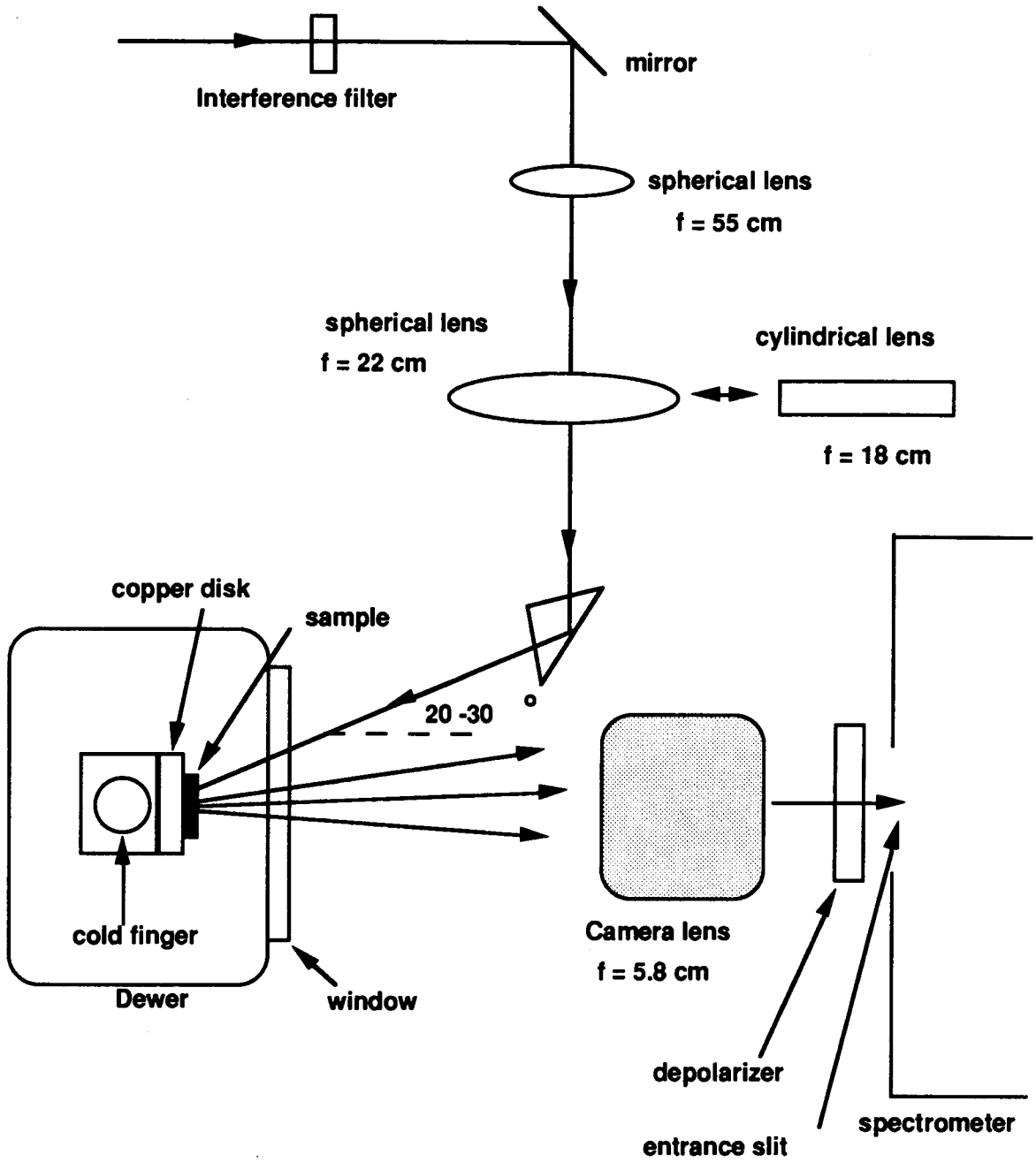

Figure 4.2

Schematic diagram of optics used to focus incident light onto the sample and scattered light into the spectrometer.

tensors is significantly larger than the xx or yy elements. It is therefore advantageous to observe these two phonons in the scattering geometry shown in Fig. 4.3 (b). In this thesis the scattering geometries depicted in Figs. 4.3(a) and 4.3(b) will be referred to as (ab) and (zz) respectively. In the (zz) geometry the crystals were also bonded to the lower bracket with clear nail polish and folded aluminum was used between the upper bracket and the sample in order to improve thermal contact. Removal of the sample from the copper disk or bracket could be achieved by soaking the copper disk (or bracket) and sample in acetone for about one minute. The disk and sample (and brackets for (zz) spectra) were mounted on the end of the cold finger of a APD Cryogenics HC2 closed cycle Helium refrigerator. Cry-con grease was applied between the cold finger and copper disk in order to improve thermal contact.

Spectra of the samples were taken at a vacuum of about 10^{-3} Torr in order to remove Raman scattering contributions due to air molecules near the sample surface and allow cooling of the sample down to 15 K using the APD refrigerator. Pumping of the space between the sample and the surrounding dewar was achieved using rotary and diffusion pumps for temperatures above 70 K. At lower temperatures the APD refrigerator alone could be used to maintain the vacuum. Monitoring and control of the sample temperature was carried out with an APD-E temperature indicator/controller which uses an Iron-doped Gold vs. Chromel thermocouple and 20 watt resistive heater.

Scattered light from the sample surface was collected using a 58 mm focal length camera lens and focussed onto the entrance slit of the spectrometer. The spectrometer used was a home built triple grating spectrometer in which the first two gratings are coupled together in a

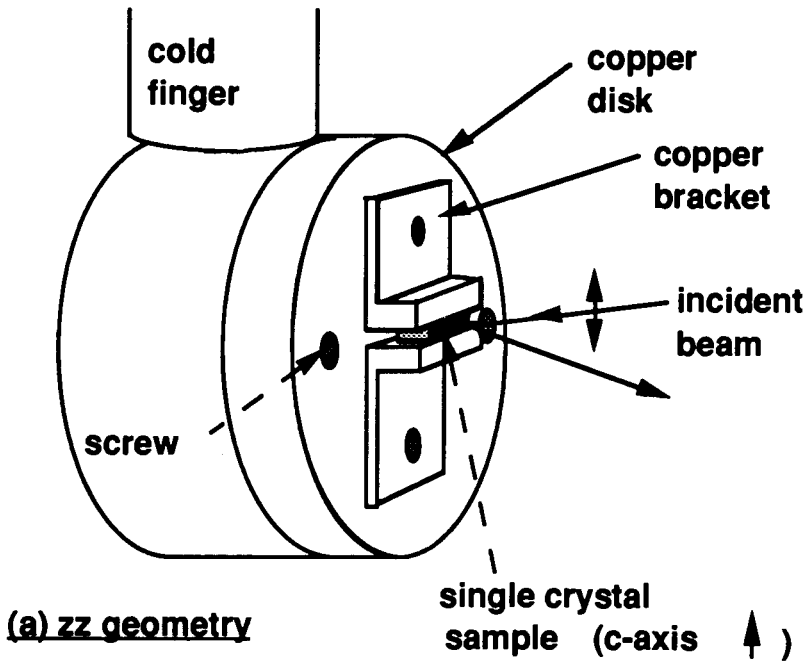

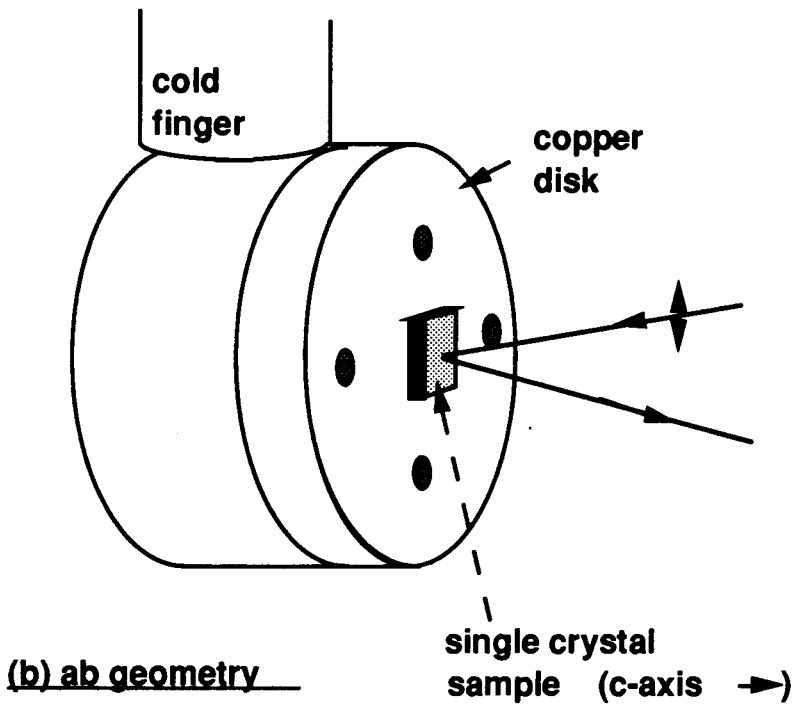

Figure 4.3

Schematic diagram of scattering geometries with (a) the incident electric field polarized along the c-axis direction of the crystal and (b) the incident electric field polarized in the ab plane of the crystal.

subtractive dispersion mode and are followed by a third grating which produces the final spectral dispersion. The first two gratings act to remove stray or elastically scattered light and result in good quality spectra even when close to the Rayleigh line (down to about 50 cm^{-1}). A choice of gratings allows several bandwidths to be investigated. The gratings remain fixed and the dispersed light is projected onto a Mepsicron multi-channel detector allowing data to be acquired simultaneously in all spectral channels. This combination of high stray light rejection, sensitivity, and short acquisition times has been put to good use for investigating the high temperature superconducting cuprates which have relatively weak Raman spectral features with frequencies ranging from approximately 100 cm^{-1} to 700 cm^{-1} [89T]. The resolution of the spectrometer was ultimately limited by the spatial extent of a single channel in the Mepsicron detector which for the grating used for the work presented in this thesis (1200 lines/mm) and incident laser wavelength λ_L = 514.5 nm, resulted in a frequency interval of about 1 cm^{-1} per detector channel.

The resolution is further limited by the adjustment of external and internal slits whose widths were set to 115 and 110 microns respectively. A convenient measure of the resulting instrumental linewidth and resolution can be obtained from the spectrum of the plasma lines of the argon ion laser tube. These plasma lines have negligible width ($< 0.1\ cm^{-1}$) [69M] compared to the spectrometer instrumental width and can therefore be treated as discrete lines. A typical plasma line spectrum is shown in Fig. 4.4 as obtained using the 514.5 nm laser line and the previously mentioned slit widths and gratings. From Fig. 4.4 it is evident that the instrumental width (FWHM) is about 4 cm^{-1}. No deconvolution of the Raman peaks with the instrumental profile has been carried out in this thesis. The plasma lines

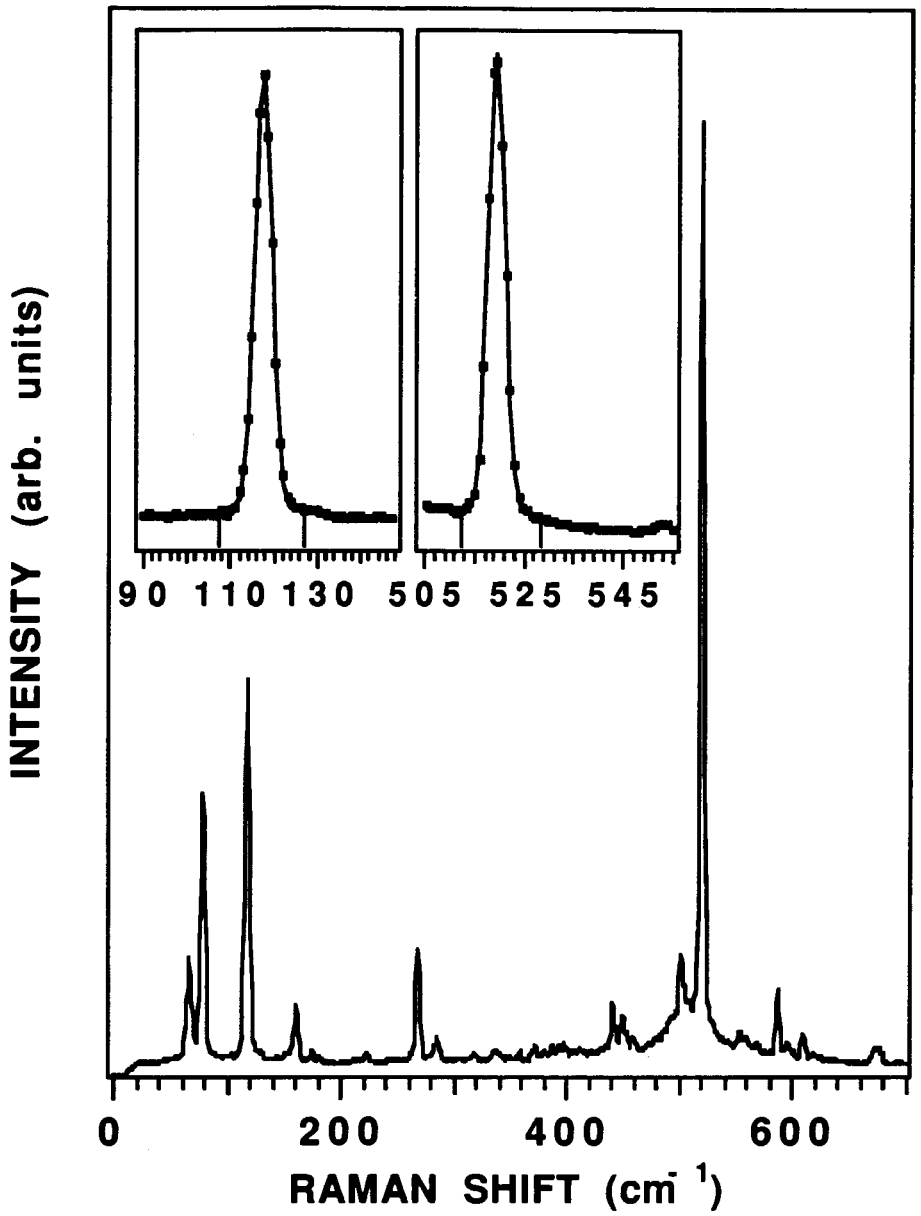

Figure 4.4

Plasma line spectrum and enlargement (inset) of plasma lines used for calibration purposes. Solid lines (inset) are Gaussian profiles fitted to the experimental data (dots).

have approximate Gaussian profiles ($I(\omega) = I_o \exp(-\frac{(\omega - \omega_o)^2}{\Gamma^2}) + B_o$) which when convoluted with the Raman peaks (approximate Lorentzians), should result [73K] an increase in the measured linewidth (FWHM) of about 1 cm^{-1}. This increase, for a given phonon and sample, is approximately independent of temperature, over the range of temperatures investigated in this thesis (< 0.5 cm^{-1} difference between 300 K and 15 K).

Backlash and play in the stepping motor drive requires that the spectrometer be recalibrated whenever the grating positions are adjusted or zeroed. In practice, external vibrations have also resulted in a similar loss of accuracy. To minimize these problems a plasma line spectrum such as the one shown in Fig. 4.4 was taken along with every sample spectrum simply by removing the interference filter (Fig.4.2). Two plasma lines such as those at frequencies (wavelengths) of 117 cm^{-1} (517.64 nm) and 521 cm^{-1} (528.7 nm) shown in Fig. 4.4, were then used to calibrate the sample spectrum by assigning these frequencies to the detector channels corresponding to the maxima of the plasma line peaks.

Further details on the design and operation of the triple spectrometer and Mepsicron detector can be found in the Ph.D. thesis of W.G. McMullen [88Mc].

The temperature recorded for a given spectrum is the temperature at the position of the thermocouple which is situated at the end of the coldfinger. The actual temperature of the sample area illuminated by the incident light may be significantly higher than the thermocouple reading due to local laser heating. This effect should be greatest when using point focussing. An estimate for the diameter, d, of the focussed disk of incident light at the sample was obtained from a magnified image of the sample and

focussed disk. The diameter of the focussed disk was found to be $120\mu \pm 40\mu$. Estimates of the local heating effects of such spot focussing on high temperature superconducting $Tl_2Ba_2CaCu_2O_8$ single crystals with dimensions comparable to the crystals investigated in this thesis have been reported by Maksimov et al. [92Mc] using Stokes/ anti-Stokes measurements. The low temperature (15 K < T < 150 K) (ab) spectra presented and used in this thesis were taken with incident powers at the sample of about 6 mW. Comparison with the results of Maksimov et al. [92Mc] for such incident powers suggests that the local temperature of the sample may be between 10 and 15 K higher than the temperature registered by the thermocouple. Note that due to the large Raman cross-sections of the 440 and 500 cm^{-1} peaks in the (zz) geometry, (zz) spectra could be taken using lower incident powers ($\approx 2mW$). Heating effects are therefore expected to be less noticeable for the (zz) spectra as compared to the (ab) spectra. In addition, the surfaces (edges) investigated in the (zz) geometry were usually cleaner (less remaining flux (used in crystal growth) and hence line focussing could be used to further reduce the incident laser heating. The line focussing resulted in an excited area of about $100(\pm 25)\mu \times 1mm$. Differences in the onset of softening of the 340 cm^{-1} phonon in spectra taken using spot and line focussing suggest that the local heating effects are relatively small (temperature increase $\lesssim$ 15 K).

Finally, observation of twin domains (Fig. 3.4) was carried out under crossed polarized light using a Reichert MeF2 optical camera microscope.

4.2 Preparation and characterization of polycrystalline $YBa_2Cu_3O_7$ samples.

The polycrystalline samples discussed in this thesis were grown at the University of Alberta by Dr. J. Franck. The samples were in the form of

pressed sintered pellets which were prepared from oxides and carbonates via the usual powder metallurgical method. More specifically, powders of Y_2O_3, CuO, and $BaCO_3$ were mixed in stoichiometric proportions and ground in an agate mortar at room temperature and in air. The resulting mixture was then pressed at 4 kbar of pressure into pellets of between 250 and 300 mg weight and 6.3 mm diameter. The resulting samples were calcined for 24 hours at 915 °C in flowing oxygen gas. Sintering and resintering of the samples was then carried out at 925 °C also in flowing oxygen gas.

The polycrystalline samples studied in this thesis were prepared in pairs labelled A,B,C,D,E,F,H, and Z, with one member of each pair containing the ^{16}O oxygen isotope and the other member of the pair containing the ^{18}O isotope. The ^{18}O samples were prepared both by growth from substituted oxides ($Cu^{18}O$ and $BaC^{18}O_3$) and gas exchange (flowing $^{18}O_2$ in calcining and sintering steps). In pairs A,B,C,D,E,F, and H, 99.1% pure ^{18}O gas was used in the calcining and sintering steps of the ^{18}O substituted sample while in pair Z, a 50%-50% atmosphere of $^{18}O_2$ and $^{16}O_2$ was used in an attempt to obtain a 50% ^{18}O-exchanged sample. A summary of these sample pairs is given in table 4.1. The samples were characterized by x-ray diffraction measurements, secondary ion mass spectroscopy (SIMS) [90Fc], and also the frequencies and temperature dependences of the Raman active phonon modes.

The superconducting properties of $YBa_2Cu_3O_y$ depend sensitively on the degree of oxygenation y, in particular the superconducting transition temperature which becomes zero at about y = 6.5 [87C]. In addition, other properties such as the frequencies and temperature dependences of the Raman active phonon modes also depend sensitively on oxygen concentration as will be shown in this thesis. Hence any meaningful comparison of sample measurements requires a knowledge of the oxygen

content. Cava et al. [87C] have measured lattice parameters of $YBa_2Cu_3O_y$ as a function of oxygen concentration, y, and these results can be used to determine the approximate oxygen concentration of a sample by means of x-ray diffraction. In particular Cava et al. [87C] found that the c-axis parameter (lattice spacing in the c-axis direction) varied approximately linearly from 11.680 Å at y = 7.0 to 11.740 Å at y = 6.6. Powder x-ray spectroscopy (Rigaku Rotaflex, sampling step 0.004, filtered Cu $K_{\alpha 1}$ radiation) [90Fc] of the polycrystalline samples studied in this thesis gave an average value of the c-axis parameter of 11.67 Å± 0.01 Å which implies essentially complete oxygenation (y > 6.95). This is consistent with the absence of a defect induced chain mode at about 235 cm^{-1}, which should appear [91H] in the Raman spectrum of even slightly deoxygenated samples (e.g. y = 6.95). In addition the x-ray diffraction patterns did not provide any evidence of impurity phases [88Lc] such as $BaCuO_2$, Cu_2O, CuO, $BaCO_3$ and Y_2BaCuO_5 which would contribute extra diffraction peaks.

The superconducting transition temperatures, T_c, of the polycrystalline samples were determined both by four-terminal resistance and by AC susceptibility measurements. These two methods gave almost identical results for the critical temperatures and gave values greater than 87.0 K ± 0.1 K for all samples. Results of the resistance measurements obtained by extrapolating the straight line portion of the resistance temperature curve in the transition region to the approximate point of zero resistance are listed in table 4.1. Transition widths (temperature interval containing 10% to 90% of the full transition) in all cases varied between 1 K and 1.5 K. Based on previous measurements of T_c as a function of oxygen concentration, one expects a critical temperature T_c in excess of 90 K for a fully oxygenated pure sample. A comparison with the T_c values obtained for the

Table 4.1. Critical temperatures of polycrystalline sample pairs A, B, C, D, E, F, H and Z. The first member of each pair (A_1, B_1, etc.) is the ^{16}O sample and the second (A_2, B_2, etc.) is the ^{18}O exchanged sample. The letters in parentheses in column 1 refer to the ^{18}O oxides used in preparing the substituted samples (Cu = $Cu^{18}O$; Ba = $BaC^{18}O_3$). The error in the T_c measurement is given in the first row.

Sample	T_c (K)
A_1	88.2±0.1
A_2 (Cu, Ba)	86.8
B_1	89.8
B_2 (Ba)	89.5
C_1	91.4
C_2	91.2
D_1	87.1
D_2 (Cu, Ba)	87.0
E_1	88.7
E_2 (Cu)	87.6
F_1	89.3
F_2 (Cu)	88.2
H_1	88.7
H_2 (Cu, Ba)	88.0
Z_1	90.0
Z_2 (Cu, Ba)	89.2

polycrystalline samples discussed here suggests that their oxygen concentration is $y \gtrsim 6.9$ which is slightly smaller that the value of $y \gtrsim 6.95$ obtained from the x-ray measurements. It is possible however that the T_c values may be slightly suppressed because of the presence of small amounts of impurities such as Zn or Sr. It is known [88Tc] for example that T_c in $YBa_2Cu_3O_7$ is rapidly suppressed by the addition of small amount of Zn, and the starting oxides used in the preparation of the samples discussed here had cation impurity (including Zn) concentrations which were consistent with the critical temperatures being a few degrees low. In any case, both samples in any sample pair have roughly the same impurity concentration. In addition the frequency of the 500 cm^{-1} mode in the Raman spectra of the unexchanged (^{16}O) samples was typically greater than 500 cm^{-1} at room temperature which also suggests [88Ma] almost complete oxygenation that is $y > 6.95$.

Finally SIMS measurements [90Fc] indicated that samples A-H were ^{18}O exchanged to greater than 80%. It should be mentioned that although the samples were exchanged to greater than 80%, individual oxygen sites may be exchanged by significantly less than this overall amount. Additional details concerning the preparation and characterization of the polycrystalline samples can be found in references [90Fc] [90I] and [91Aa].

4.3 Preparation and characterization of $YBa_2Cu_3O_7$ crystals grown in thoria crucibles

The three $YBa_2Cu_3O_7$ crystals investigated and described in this section were grown in thoria crucibles by a flux method. The flux method refers to the use of molten inorganic salts and oxides which act as a solvent for

crystallization at elevated temperatures [66G]. For the crystals described in this thesis, the flux consisted of oxides of copper and barium. The crystals grown in thoria crucibles and described here were grown using 6.7% by weight high purity YBaCuO powder in a BaO:CuO (28:72) flux [92La]. All the crystals described in this thesis were grown at the University of British Columbia by Dr. A. O'Reilly (crystals grown in thoria crucibles) and Dr. Ruixing Liang (crystals grown in zirconia crucibles). Descriptions of the crystal growth conditions and procedures used by these workers can be found in reference [92La]. The crystals grown in thoria crucibles were annealed in flowing oxygen at 40 atm. and 600 $^{\circ}C$ for 72 hours and then cooled at 10 $^{\circ}C$ per hour after which the transition temperature of the crystals was determined to be 89.5 K by DC magnetization in a 10 Gauss applied field of a commercial SQUID magnetometer. Further oxygen annealing produced no discernable change in the crystal properties indicating essentially uniform oxygen content. Elemental analysis by a commercial firm [E] using ICP (inductively coupled plasma) mass spectroscopy revealed that the crystals contained about 8700 ppm by weight of thorium and about 640 ppm by weight of zinc. The source of these impurities could be traced to the composition of the crucibles used to grow the crystals. These impurity levels likely account for the critical temperature of the crystals being slightly lower than the approximate maximum of 93.0 K for this compound. The magnetic transition was quite sharp (< 1.5 K) and independent of the crystal size implying a uniform distribution of the Th and Zn impurities.

X-ray diffraction measurements of the c-axis parameter were carried out on the crystals using a vertical circle diffractometer. The diffraction patterns consisted of very strong [00ℓ] lines which gave a value of $c = 11.698 \pm 0.005 \text{Å}$ for the c-axis dimension of the unit cell. This value was

obtained by a non-linear least squares fit (allowing for off axis crystal displacement) of the first six [00ℓ] Cu K_{α_1} diffraction peak positions (2θ) to the Bragg diffraction condition ($\ell\lambda = 2c\sin(\theta)$). A comparison of the obtained c-axis parameter ($c = 11.698 \pm 0.005 \text{Å}$) with the results of Cava et al. [87C] suggests that the crystals are essentially fully oxygenated (i.e. y > 6.93). This conclusion is supported [88Ma] by the frequency of the 500 cm^{-1} mode in the room temperature Raman spectra which was observed to be greater than 500 cm^{-1}, and the absence of the 235 cm^{-1} mode which is associated with oxygen vacancies in the CuO chains [91H].

Finally, the crystals described in this thesis had dimensions of up to 6.0 mm in the ab plane and 0.5 mm along the c-axis direction allowing spectra to be taken in both the (ab) and (zz) scattering geometries.

4.4 Preparation and characterization of $YBa_2Cu_3O_y$ ($6.7 \lesssim y \leq 7.0$) crystals grown in Zirconia crucibles.

The seven crystals that will now be described were initially obtained from batches of high purity crystals which were grown in yittria stabilized zirconia crucibles [92La] using the flux method described in the previous section. The crystals contained less than 10 ppm of Zr by weight and the sum of all other impurities was less than 500 ppm by weight. The elemental analysis was also carried out by a commercial firm [Q] using ICP mass spectroscopy.

Crystals with seven different oxygen concentrations (designated A,B,C,D,E,F, and G, see Table 4.2 on page 72) were then obtained by annealing the crystals at appropriate temperatures, pressures, and for suitable lengths of time. Known dependences [91S] of oxygen content on temperature and

oxygen pressure during annealing gave the initial oxygen concentration estimates. Crystals annealed under the same conditions as crystal C ($y \approx 6.95$) show a specific heat jump as narrow as 0.25 K [92La] indicating a high degree of homogeneity. Microwave measurements [92B] on these same crystals have also yielded a very small surface resistance of less than 50 $\mu\Omega$ (at 2.95 GHz and 77 K) and a correspondingly small estimate for the quasi-particle scattering rate ($< 10^3/s$ at 77 K).

The crystals had dimensions of up to 6.0 mm in the a-b plane and up to 0.5 mm along the c-axis. This latter dimension again allowed the Raman spectra to be obtained in the (zz) geometry (Fig.4.3 (b)) as well as the (ab) geometry (Fig.4.3 (a)). As mentioned previously, this allows the zz element of the Raman tensor to be studied. The annealing conditions and magnetization measurements of the seven crystals will now be described.

Crystal C was annealed in 1 atmosphere of flowing O_2 for two days at 860 $^{\circ}C$, and the temperature was then reduced to 450 $^{\circ}C$ at a rate of 18 $^{\circ}C$/hour. The crystal was then further annealed at 450 $^{\circ}C$ for a further 6 days, and then quickly cooled to room temperature (i.e. in a few minutes). This resulted in a high quality crystal with a transition temperature of 93.7 ± 0.1 K and transition width less than 0.2 K (10% - 90%) as determined by DC magnetization measurements (0.05 Oe applied field, parallel to c-axis). Considering the transition temperature and annealing conditions, the oxygen content (y in $YBa_2Cu_3O_y$) was estimated [91S] to be 6.95.

Crystal D was obtained from the same batch as crystal C and was annealed in the same way. It was then further annealed for 2 days at 510 $^{\circ}C$ in pure flowing O_2 at 1 atmosphere followed by rapid cooling, in order to reduce the oxygen concentration. This resulted in a reduced transition temperature of 92.5 ± 0.1 K and transition width of 0.4 K (10%-90%) as determined by DC

magnetization measurements (0.1 Oe applied field, parallel to c-axis). The oxygen content in this case was estimated to be y = 6.9.

Crystal E was grown and annealed in the same way as crystal C. Additional annealing for about four days at 540 $^{\circ}C$ in 1 atm of flowing O_2 resulted in crystal whose oxygen concentration was estimated to be y = 6.85, and a transition temperature of 91.1 K which was determined from DC magnetization measurements with an applied field of 0.1 Oe.

Crystal F was not taken from the same batch as crystal C, D and E but was grown and annealed under identical conditions. Crystal F was then further annealed for 72 hours at 550 $^{\circ}C$ in flowing O_2 at 1 atmosphere followed by rapid cooling. This resulted in a crystal with a transition temperature of 88.0 ± 0.2 K and transition width of 1.3 K (10%-90%) as determined by DC magnetization measurements (0.05 Oe applied field, parallel to c-axis). The resulting oxygen content for this crystal was estimated to be y = 6.85.

Crystal G was initially grown and annealed in a manner similar to crystal C and additional annealing for about 110 hours at 700 $^{\circ}C$ and 1 atm of flowing O_2 resulted in a crystal with an estimated oxygen concentration of y = 6.7, and a T_c of 59.2 K and transition width of 4.3 K (10%-90%), as determined from DC magnetization measurements with an applied field of 10.0 Oe.

Crystal B was also grown and annealed at high temperatures under identical conditions as crystal C, but was further annealed under high pressure in the following way. The crystal was heated at 50 $^{\circ}C$/hour under 31.6 atm. of pure O_2 up to a temperature of 450 $^{\circ}C$. The crystal was then kept at 450 $^{\circ}C$ for 24 hours under 39.5 atm. of pressure. It was then cooled at 3 $^{\circ}C$/hour to 350 $^{\circ}C$, kept at 350 $^{\circ}C$ and 37.5 atm. of pressure for 48 hours and finally cooled at 100 $^{\circ}C$/hour and 31.6 atm. of pressure. This resulted in a

crystal with a transition temperature of 93.0 ± 0.1 K, a transition width of 0.5 K (10%-90%) as determined by DC magnetization measurements (0.1 Oe applied field, parallel to c-axis), and an oxygen content y estimated to be greater than 6.95.

Crystal A was grown in the same manner as crystals B, C, D, E, F, and G, but was annealed by heating at 50 °C/hour under 32.6 atm. of pure oxygen to a maximum temperature of 500 °C, held at 500 °C and 32.6 atm. for 24 hours, after which it was cooled at 3 °C/hour to 350 °C and kept 350 °C and 32.6 atm. for 48 hours. Finally, crystal A was cooled at 100 °C/hour and 32.6 atm. This crystal had a transition temperature of 89.7 ± 0.2 K, a transition width of 2.5 K (10%-90%) as determined by DC magnetization measurements (10.0 Oe applied field, parallel to c-axis), and an oxygen content, y, estimated to be greater than 6.95. Chemical analysis of this crystal by a commercial firm [Q] using ICP mass spectroscopy indicated about 500 ppm (by weight) of potassium, in contrast with the previous six crystals. The source of this potassium was the fire brick used in the oven. It has been found that the initial high temperature (860 $^{\circ}C$) anneal [92La] used for crystals B,C,D,E,F, and G, ensures that the potassium concentration in these crystals is less than 50 ppm by weight. Although the amount of potassium in crystal A is still small (0.05 % by weight), it may act as an acceptor impurity by substituting for barium and may thus enhance the hole concentration in the crystal.

A comparison of the Raman spectra obtained from as grown crystals, and from crystals etched in a 1% Br/Ethanol solution [89W] for up to 1.5 hours did not indicate any significant differences, implying surface properties similar to that of the bulk. In particular, the oxygen content near the surface did not appear to be depleted from that of the bulk.

Table 4.2. Initial oxygen concentration estimates, y, c-axis parameters, refined oxygen concentrations, and results of DC magnetization measurements for $YBa_2Cu_3O_y$ crystals A,B,C,D,E,F, and G.

CRYSTAL	y (initial estimate)	c-axis parameter A	y (refined value)	T_c(K)	ΔT_c (10% -90%) (K)	Applied field (Oe)
A	7.0	11.688 ±.001	7.0 ±.02	89.7	2.5	10.0
B	>6.95, <7.0	11.689	6.99	92.8	0.8	0.1
C	6.95	11.698	6.93	93.7	<0.2	0.05
D	6.9	11.703	6.90	92.0	2.2	5.0
E	6.85	11.710	6.86	91.1	2.7	0.1
F	6.85	11.718	6.81	87.7	1.3	0.05
G	6.7	11.738	6.68	59.2	4.3	10.0

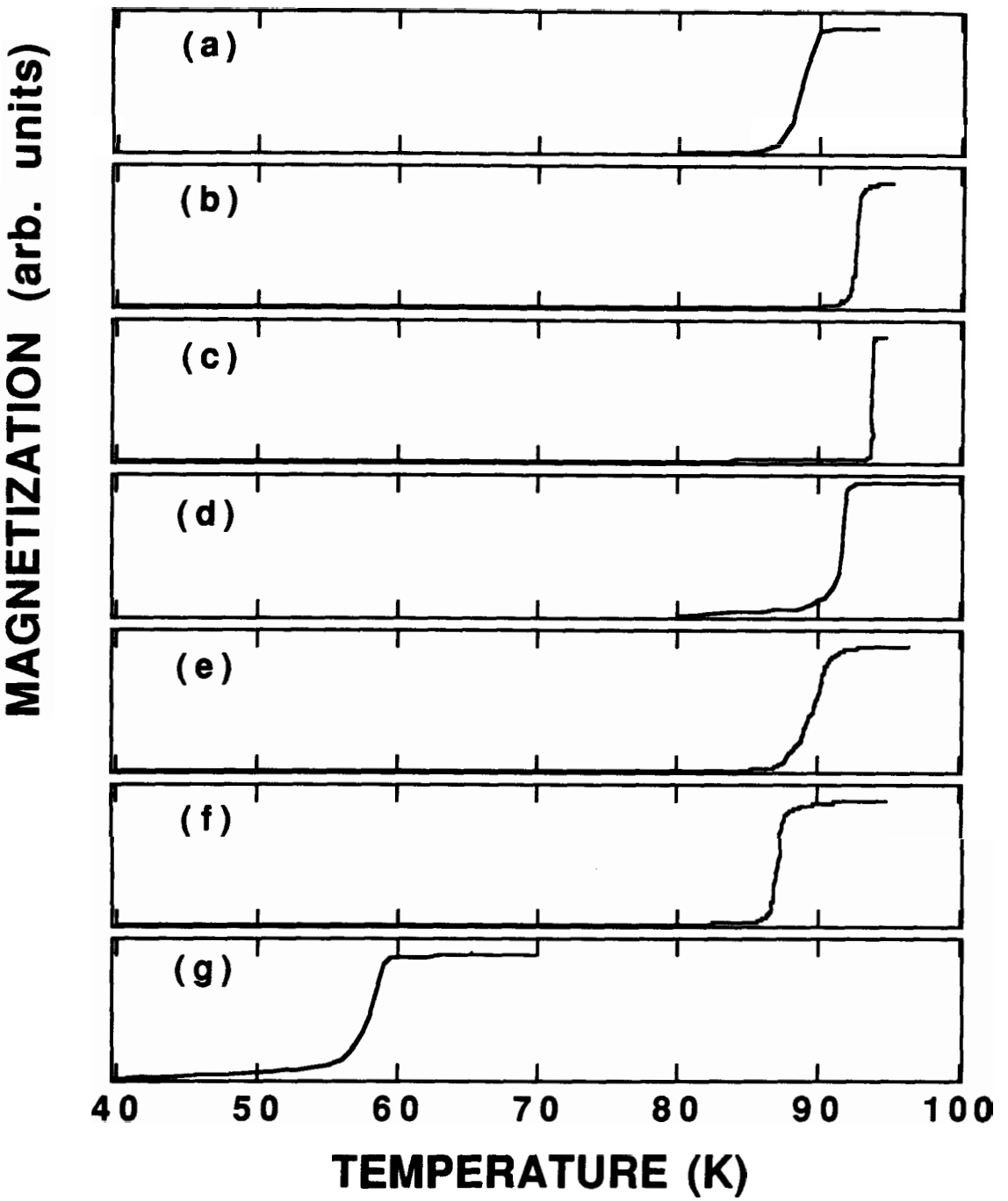

Figure 4.5

DC magnetization as a function of temperature for crystals A,B,C,D,E,F, and G cooled in fields, H_o, of 10.0 Oe, 0.1 Oe, 0.05 Oe, 5.0 Oe, 0.1 Oe, 0.05 Oe, and 10.0 Oe respectively with H_o parallel to the c-axis of the crystals.

The T_c values mentioned above and listed in Table 4.2 were determined from the intersection [91V] of the linear portion of the transition with the normal state baseline. Transition curves measured for crystals A, B, C, D, E, F and G using DC magnetization techniques are shown in Fig. 4.5. In all cases, the external field was parallel to the c-axis of the crystal under investigation.

The variation in the applied fields used in the magnetization measurements merely reflects the fact that some of the measurements were made with a commercial SQUID magnetometer (applied fields of 5.0 and 10.0 Oe) while the remaining measurements (applied fields of 0.05 and 0.1 Oe) were carried out with a highly sensitive SQUID magnetometer designed by Dr. S. Gygax at Simon Fraser University. The choice of which magnetometer to use was dictated by availability and time constraints. Differences in the superconducting transition widths listed in Table 4.2 and shown in Fig. 4.5 could in part be due to the differences in applied fields used in the magnetization measurements.

The oxygen concentrations of these crystals initially estimated from the annealing conditions were refined through c-axis spacings determined by x-ray diffraction measurements.To ensure that the top surface of the crystals was coincident with the zero angle plane of the vertical circle diffractometer, the crystals were mounted as is shown in Fig. 4.6. Rocking curves carried out at the (005) diffraction peak were used to further align the crystal surface with the diffractometer. As previously mentioned, Cava et al. [87C] have demonstrated that the c-axis spacing in $YBa_2Cu_3O_y$ varies approximately linearly with the oxygen concentration y. Comparison of our data with the linear dependence of Cava et al. in reference [87C] gave the refined oxygen concentrations which are listed in Table 4.2 along with the initial oxygen

concentration estimates, c-axis parameters and results of magnetization measurements.

In obtaining these concentrations the oxygen content of crystal A was fixed at the initial estimate of y = 7.0 which was based on annealing conditions [91S]. The slope of the expected linear dependence given by Cava et al. [87C] was then used to determine the remaining oxygen concentrations from the measured c-axis spacings. The intercept of the linear dependence of Cava et al. was assumed to depend on details of the sample mounting and measurement procedure and hence only the slope was used. This assumption was supported by neutron scattering measurements [90J] which reproduced the linear dependence of Cava et al. [87C] except for an offset in the magnitudes of the c-axis parameters.

A non-linear least squares fit of the positions (2θ) of the first eight (or more if possible) Cu K_{α_1} [00ℓ] diffraction peaks (allowing for off-axis crystal displacement) to the Bragg diffraction condition ($\ell\lambda = 2c\sin(\theta)$) was used to determine the c-axis spacings. A typical diffraction pattern from crystal E is shown in Fig. 4.7 with the [00ℓ] peaks labeled. Fig. 4.8 shows the c-axis parameter and assigned oxygen concentration for each crystal superimposed on the linear dependence of Cava et al. [87C].

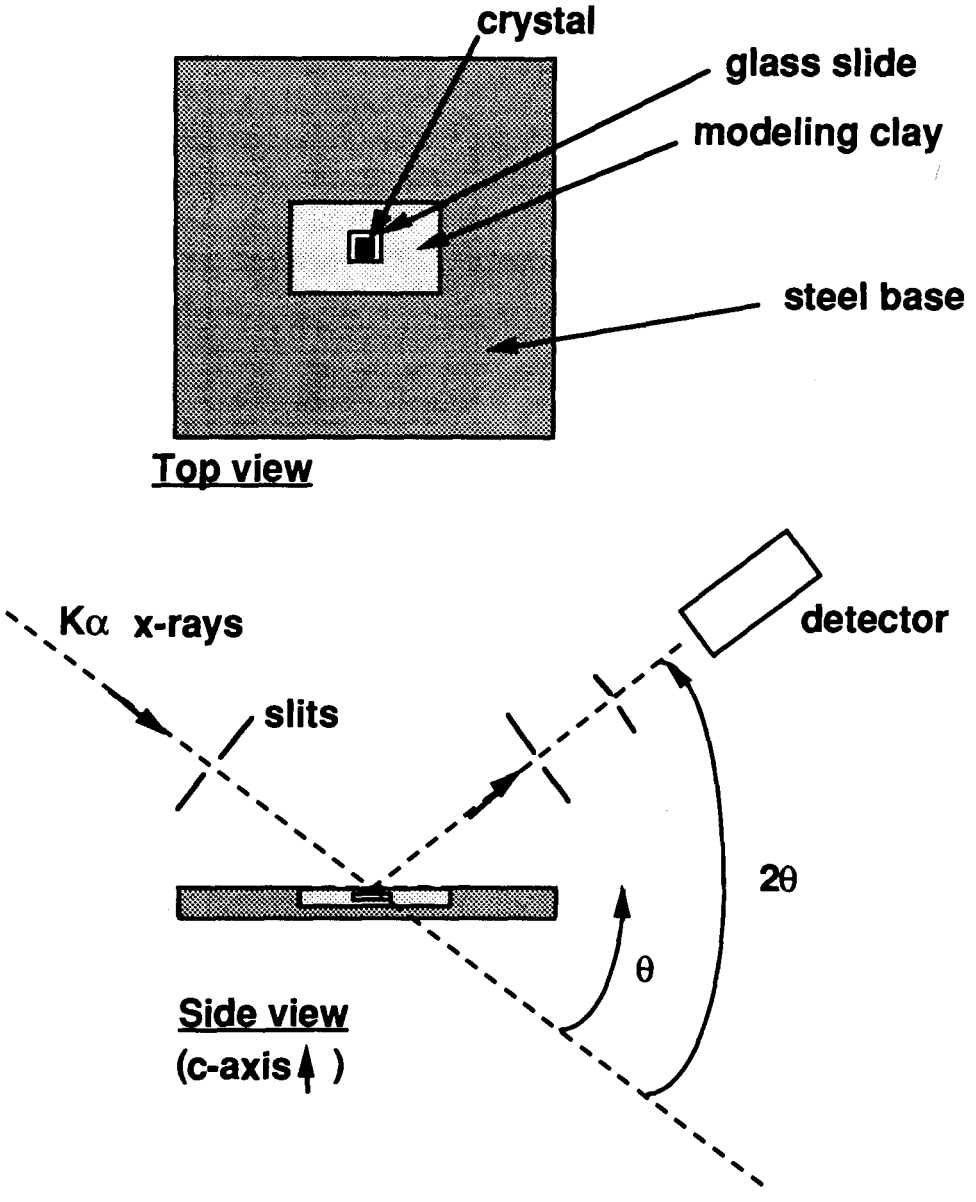

Figure 4.6

Schematic diagram of stage used to take x-ray diffraction measurements of crystals A,B,C,D,E,F, and G.

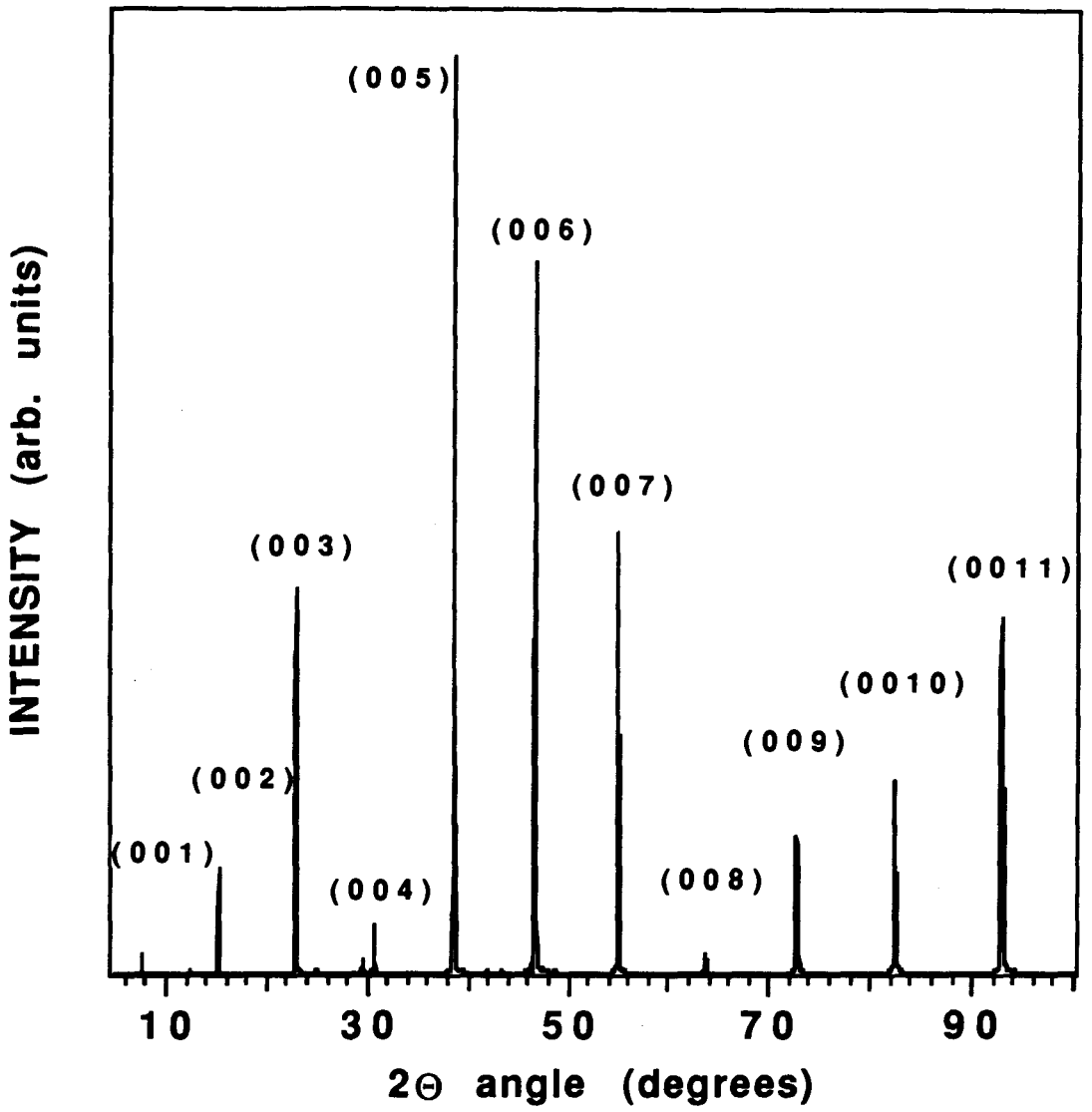

Figure 4.7

X-ray diffraction pattern for crystal E indicating the [00ℓ] diffraction peaks used to determine the c-axis parameter.

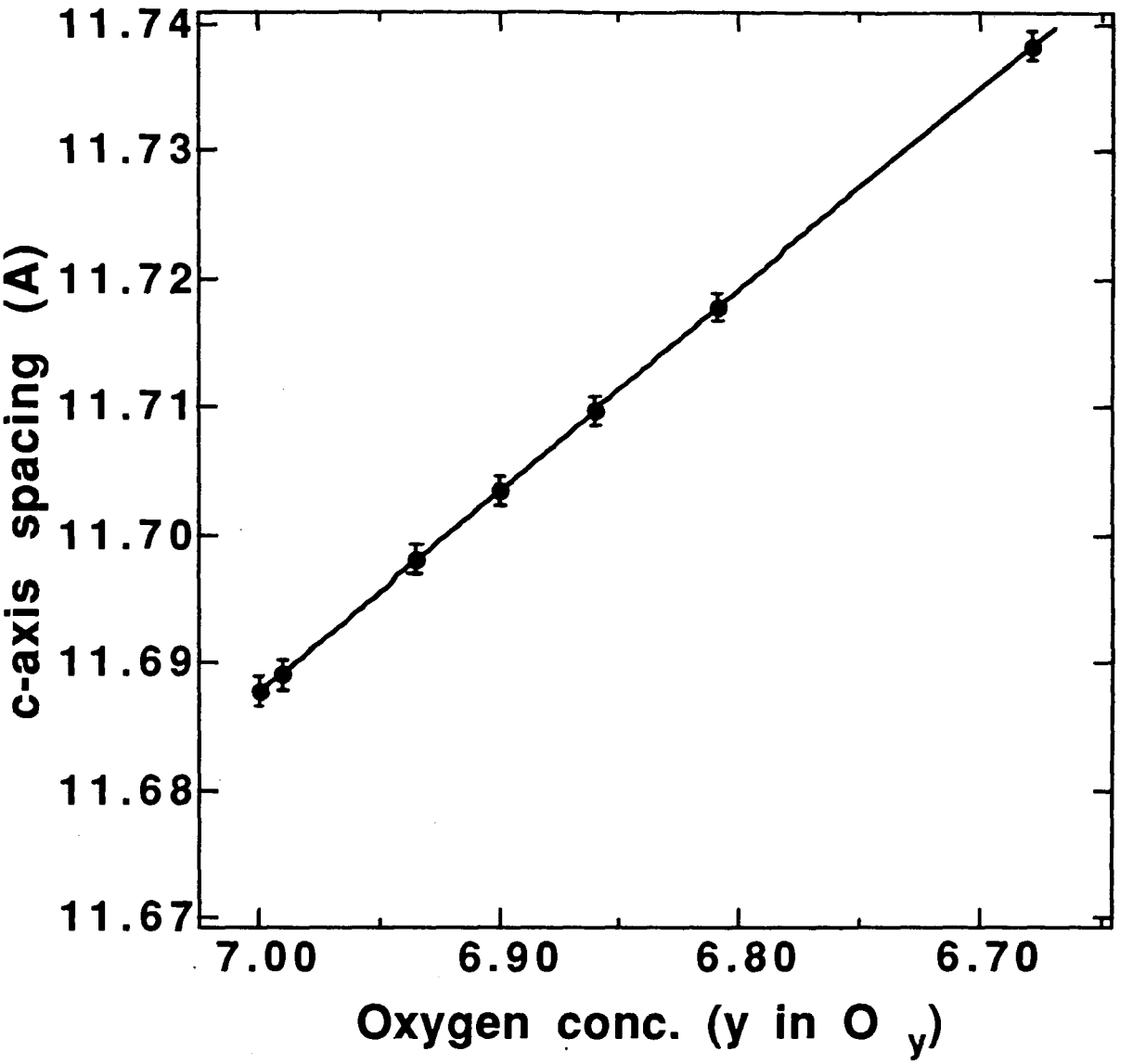

Figure 4.8

X-ray diffraction determined c-axis spacings versus oxygen concentrations for crystals A,B,C,D,E,F, and G, (filled circles), as determined by the linear dependence of Cava et al. [87C].

CHAPTER 5

ISOTOPE SUBSTITUTION AND NORMAL MODES

5.1 Experimental results

The results of Raman spectra taken from eight pairs of polycrystalline $YBa_2Cu_3O_7$ samples will now be presented. The preparation and characterization of these samples is described in chapter 4, and the various sample pairs are listed in Table 4.1. A typical set of spectra obtained from samples C_1 and C_2 are shown in Fig. 5.1. A close examination of this figure reveals that the 500 cm^{-1} peak in the spectra of the substituted sample, C_2, is shifted to a lesser degree than the 340 and 440 cm^{-1} modes relative to the corresponding modes in the unsubstituted sample C_1. This trend in also evident in the frequency shifts of the 340,440, and 500 cm^{-1} phonons of the substituted samples D_2, E_2, F_2, H_2, and Z_2, which are listed in Table 5.1 (all frequency and linewidths in this chapter were estimated by eye). This result is inconsistent with the previously discussed (chapter 3) mixing or hybridization of the 500 cm^{-1} mode with the 340 and 440 cm^{-1} modes which was predicted by LDA calculations [90C] [90R] and which would most likely result in approximately the same percentage frequency shift for all three modes. In addition, the degree of broadening of the 500 cm^{-1} mode appears to be greater than the linewidth changes of the 340 and 440 cm^{-1} modes. This can be seen in the spectra shown in Fig. 5.1 and also the isotope substitution induced linewidth shifts listed in Table 5.2. It is suggested that this broadening results from disorder due to incomplete substitution at the bridging O(4) site which is involved in the 500 cm^{-1} mode. This is consistent with the observation that the degree of broadening is correlated with

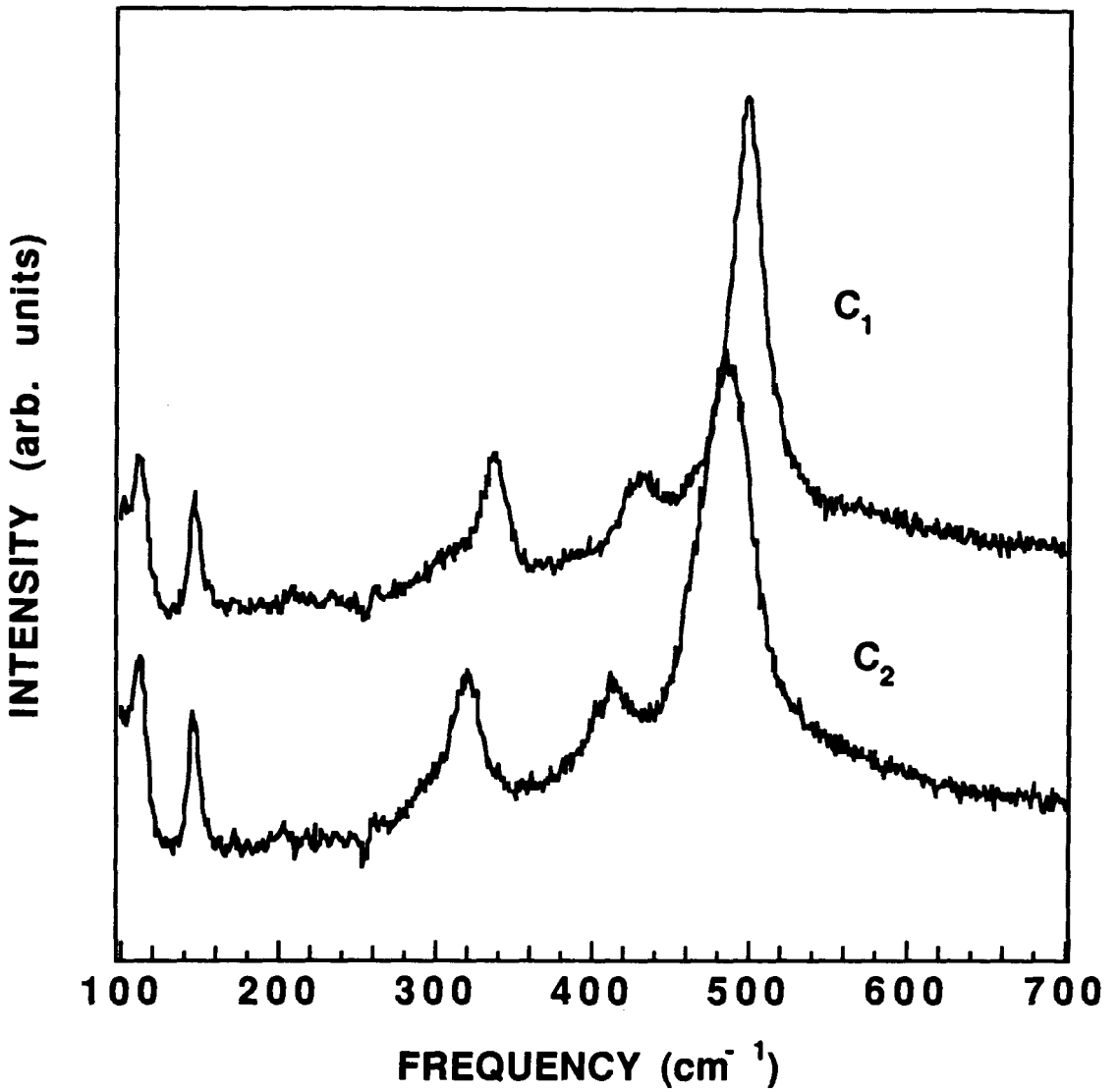

Figure 5.1

Raman spectra for the sample pair C_1-C_2 (^{18}O substituted sample is C_2). Spectra are offset for clarity, and the arrow indicates the 500 cm^{-1} peak in spectra of C_2.

Table 5.1. Experimental isotopic phonon frequency shifts of the 340, 440, and 500 cm^{-1} phonons of polycrystalline $YBa_2Cu_3O_7$ sample pairs A,B,C,D,E,F,H, and Z. All values are in cm^{-1} , and the estimated uncertainty is indicated in the first row.

Sample	Mode	Shift (%)	Mode	Shift (%)	Mode	Shift (%)
A_1	503	4.4	438	3.9	338	4.4
A_2	481	±0.4	421	±0.5	323	±0.5
B_1	502	4.6	436	4.8	338	5.0
B_2	479		415		321	
C_1	502	3.4	435	4.8	339	4.7
C_2	485		414		323	
D_1	502	3.6	438	4.1	338	4.1
D_2	484		421		324	
E_1	502	2.8	435	3.9	338	4.7
E_2	488		418		322	
F_1	502	2.4	435	5.3	339	5.6
F_2	490		413		320	
H_1	501	2.6	436	5.5	339	5.6
H_2	488		412		320	
Z_1	502	1.0	438		340	2.4
Z_2	497				332	

the degree of $^{18}O/^{16}O$ exchange as estimated by isotopic frequency shift of the 500 cm^{-1} mode. For instance, the degree of broadening is greatest for those samples, listed in Table 5.2, where the frequency shift of the 500 cm^{-1} mode is about 50% of the percentage shifts of the 340 and 440 cm^{-1} modes.

5.2 Theoretical background

The Equation of Motion method used for this chapter is described in detail in section 2.6 of chapter 2. This theoretical technique was used to model the effects of isotopic substitution on the behavior of the 500 cm^{-1} mode. The results of these calculations will now be presented, and compared to Raman spectra obtained from polycrystalline $YBa_2Cu_3O_7$ samples whose preparation and characterization was discussed in chapter 4.

Shell model calculations [88Lb] predict that the lattice motion which gives rise to the 500 cm^{-1} Raman line is the stretching motion along the c-axis of the bridging O(4) atoms with all other atoms stationary. This atomic displacement pattern is shown in Fig. 3.3 of chapter 3. To model this, a one-dimensional (1D) linear chain of oxygen and copper atoms was used as shown in Fig. 5.2. Atoms in the chain interact through nearest neighbor harmonic forces and initially all O(4) atoms are ^{16}O. Force constants were adjusted so that initial antiphase displacements, u_i^o, of the $^{16}O(4)$ atoms along the chain axis generated a single Raman peak at 502 cm^{-1}, through equations 2.16, 2.22, and 2.24, which were solved numerically . The frequency of 502 cm^{-1} was chosen to correspond to the experimentally observed frequency of this mode in unsubstituted samples. The force constants used were k_1=150.5 N/m,

Table 5.2. Experimental phonon linewidths (FWHM) in cm^{-1} of the 340 and 500 cm^{-1} phonons of polycrystalline $YBa_2Cu_3O_7$ sample pairs A,B,C,D,E,F,H, and Z. Estimated uncertainties in the linewidths are ± 1 cm^{-1}.

Sample	340 cm^{-1} mode		500 cm^{-1} mode	
	Width	Change (%)	Width	Change (%)
A_1	18	5.5	29	20.7
A_2	19		35	
B_1	17	11.8	24	29.2
B_2	19		31	
C_1	18	0.0	22	54.5
C_2	18		34	
D_1	19	0.0	32	21.9
D_2	19		39	
E_1	19	0.0	25	44.0
E_2	19		36	
F_1	17	11.8	23	65.2
F_2	19		38	
H_1	17	5.9	23	60.9
H_2	18		37	
Z_1	20	25.0	25	40.0
Z_2	25		32	

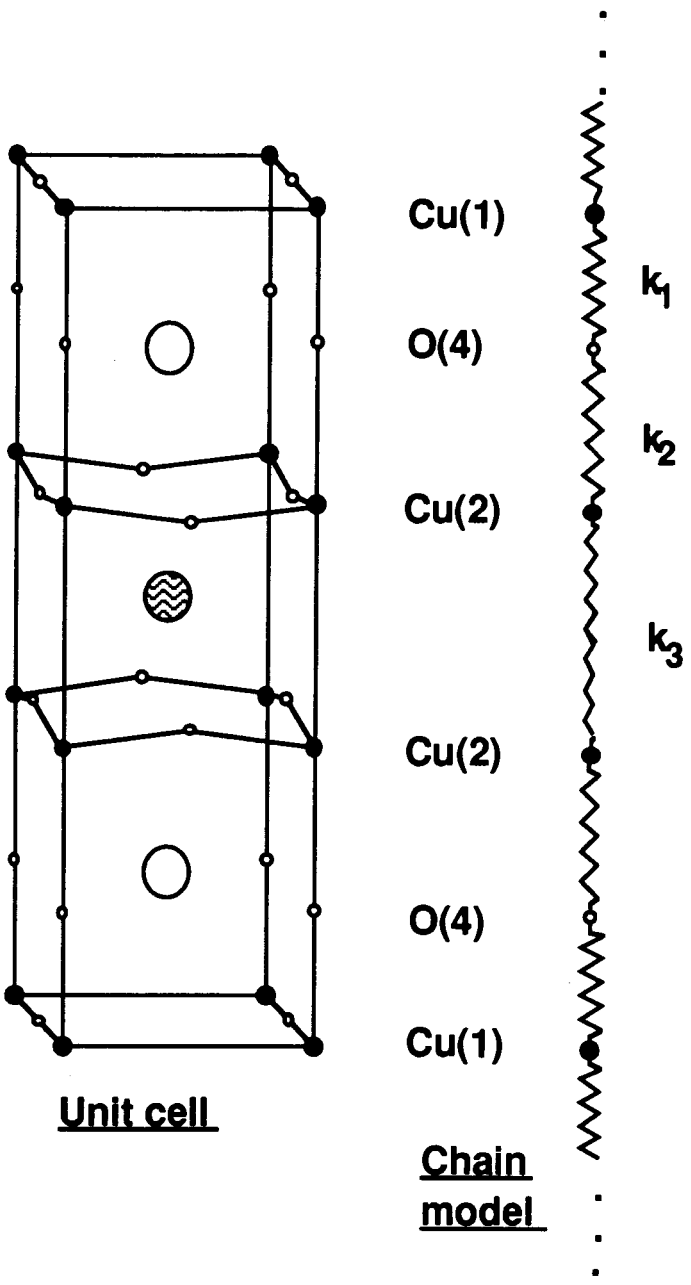

Figure 5.2

$YBa_2Cu_3O_7$ unit cell and chain model used to generate 500 cm^{-1} Raman peak.

k_2=88.1 N/m, and k_3=7140.3 N/m. The value of k_3 was chosen to be very large in order to inhibit the relative motion of the planar copper atoms, Cu(2) and Cu(3), which for this mode are not expected to move to any significant degree in unsubstituted samples according to shell model dynamical calculations [88Lb]. Note, however, that the force constant coupling the Cu(1) and O(4) atoms was not chosen to be large. As a result, motion of the Cu(1) atoms as well as in-phase motion of the coupled Cu(2) atoms is possible in the substituted chains.

Isotopic substitution was implemented by randomly replacing ^{16}O atoms in the chain by ^{18}O atoms. Substituting an ^{18}O atom for a ^{16}O atom at a given atomic site i, amounts to changing the mass of the atom at that site i, m_i, from 16 au. to 18 au. The probability of substitution at the O(4) sites was adjusted so that various degrees of substitution can be considered. The degree of substitution is specified by the ^{18}O concentration, which is defined as the percentage of O(4) sites occupied by ^{18}O atoms. The $\gamma\beta$ element of the atomic displacement polarizability tensor $D_{i\alpha}^{\gamma\beta}$ was assumed to be unaltered by the isotopic substitution. This seems reasonable since a change in isotopic mass is not expected to change the electronic properties of an atom. Initial displacement amplitudes of the unsubstituted atoms, u_i^o, therefore remained unaltered while the initial displacement amplitudes of the substituted atoms became $16u_i^o/18$ (equation 2.23a). Equations 2.16, 2.22, and 2.24 were then once again used to determine the Raman spectrum in each case.

The theoretical parameter γ was chosen so that the 100% ^{16}O peak at 502 cm^{-1} has a full width at half maximum (FWHM) similar to the measured FWHM of the unsubstituted experimental peaks ($\approx$ 26.0 cm^{-1}).

Finally, a chain length of 600 atoms was used and stated peak positions, FWHM, and errors are the results of averages over 10 spectra for any given ^{18}O concentration.

5.3 Theoretical Results

Theoretical Raman cross sections for the 502 cm^{-1} mode were computed for relative ^{18}O chain concentrations of 0%, 10%, 25%, 35%, 50%, 65%, 75%, 90%, and 100%. The frequency shifts and linewidth changes resulting from the calculation are summarized in Table 5.3, and the computed line profiles are shown graphically in Fig. 5.3 for relative ^{18}O concentrations of 0%, 25%, 35%, 50%, 75%, and 100%. Two measured line shapes obtained from the spectra of samples E_1 and E_2 are also shown in Fig. 5.3. From this figure it is clear that there is good agreement between the calculated and experimentally determined degree of broadening. In particular, the chain-model calculations indicate that sample E_2 has a relative ^{18}O concentration on the O(4) site of approximately 35%. Note also that the shift for full ^{18}O substitution (100% ^{18}O concentration) is 5.73% of 502 cm^{-1} which agrees quite well with full lattice dynamics calculations of 5.9% [88Ca], 5.5% [89B], and one minus the square root of the ratio of masses which gives 5.72%.

The calculated isotope shift is plotted versus relative ^{18}O concentration in Fig. 5.4 and the results clearly indicate a nonlinear dependence. In particular, the 502 cm^{-1} mode is predicted to be shifted by 50% of its maximum for a relative ^{18}O concentration of 37 $\pm$ 4 %. A comparison of the experimental isotope shifts listed in Table 5.1 with the dependence shown in Fig. 5.4 yields predicted relative ^{18}O concentrations for all the substituted samples. These concentrations are listed in Table 5.4 along with the

concentrations obtained by assuming a linear dependence of the isotope-induced frequency shift of the Raman line on the relative ^{18}O concentration.

A comparison of the numerical values of these data points (Table 5.4) indicates that the assumption of a linear dependence can overestimate the relative ^{18}O concentration by as much as 10-16%.

The percentage change in the FWHM is plotted versus the percentage frequency shift of the 500 cm^{-1} mode in Fig. 5.5 using the calculated results presented in Table 5.3. As before, all differences and shifts are with respect to the ^{16}O spectra. The experimental results obtained from the eight sample sets are also presented in the same figure for comparison. From Fig. 5.5 one can see that the experimentally observed linewidth is a maximum for a frequency shift of approximately 2.4%, which is about 40% of the maximum shift. This in turn corresponds to a sample which is isotope exchanged to between 24% and 35% (Fig. 5.4). As is evident from the figure, the experimental results are in reasonably good agreement with the chain model predictions. These results suggest that the linear chain model can be used to describe the 500 cm^{-1} phonon mode. This in turn implies that the degree of hybridization or mixing of the 500 cm^{-1} mode with the 340 and 440 cm^{-1} modes should be small, since these last two modes are not incorporated into the linear chain model. This agrees with the previously mentioned observations obtained directly from the experimental frequency shifts and linewidth changes shown in Tables 5.1 and 5.2.

The asymmetric aspects of the above results can be interpreted in the following manner. From Fig. 5.3, an ordered chain containing ^{16}O atoms only generates a $k = 0$ mode at 502 cm^{-1}, and the same chain with ^{18}O atoms only results in a $k = 0$ mode at 474 cm^{-1}. These modes involve motion of the oxygen atoms only. If disorder is introduced into the chain, for example, by

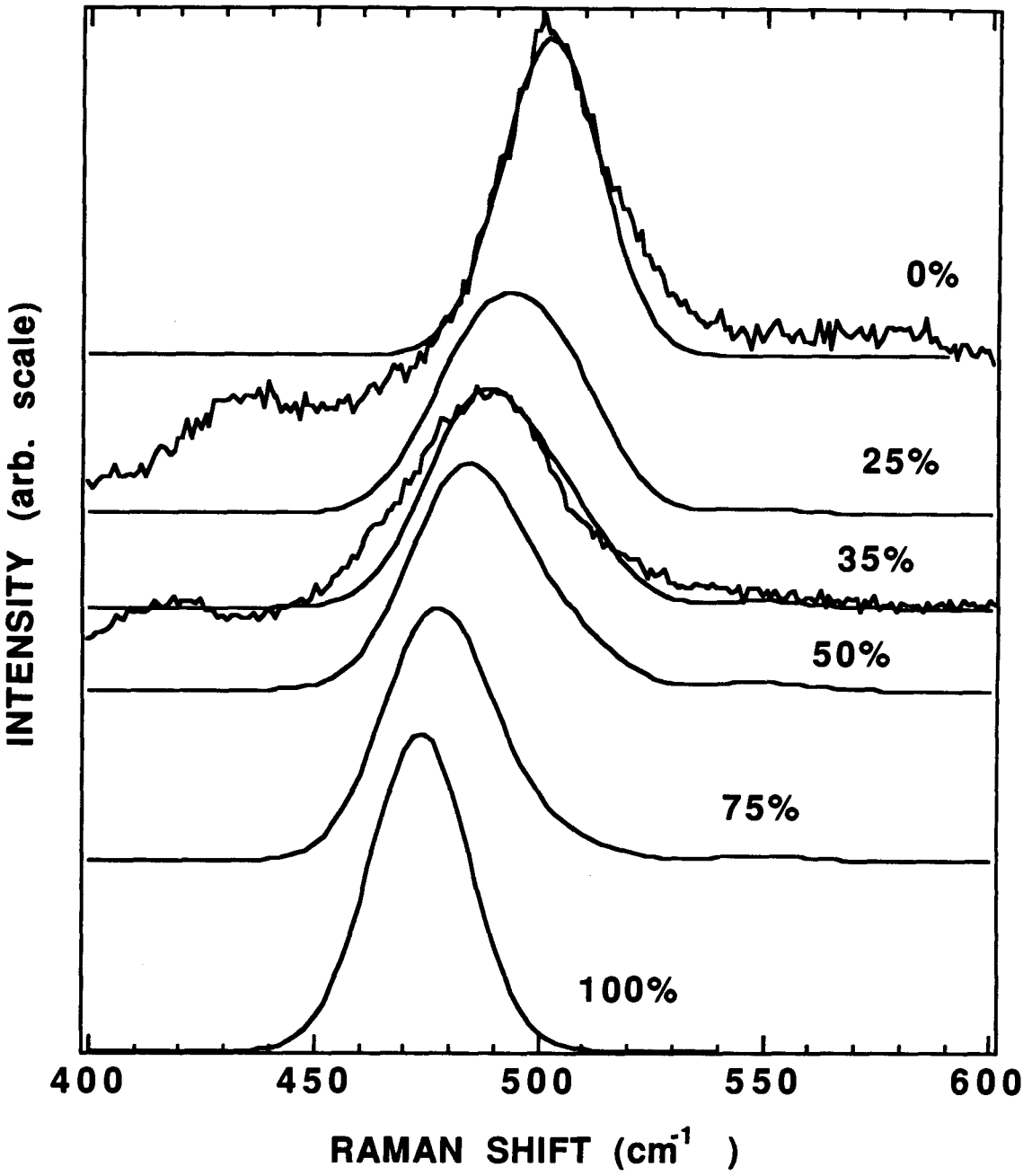

Figure 5.3

Raman cross sections calculated using the chain model (smooth curves) for ^{18}O concentrations of 100%, 75%, 50%, 35%, 25%, and 0% [percentage of O(4) chain sites occupied by ^{18}O atoms]. The experimental peaks from spectra obtained from sample pair E_1, E_2 are also shown.

Table 5.3. Theoretical results for the 500 cm^{-1} peak frequency shifts and linewidth (FWHM) changes due to ^{18}O substitution. The relative concentration of ^{18}O is in terms of O(4) sites occupied by ^{18}O, i.e., $[^{18}O(4)/^{16}O(4)]$.

Relative ^{18}O concentration (%)	Position shift (%)	Width change (%)
0	0.0	0.0
10	0.34 ± 0.09	18.4 ± 3.2
25	1.65 ± 0.46	63.1 ± 8.8
35	2.77 ± 0.12	41.1 ± 14.6
50	3.78 ± 0.20	25.2 ± 8.4
65	4.52 ± 0.12	17.3 ± 1.4
75	4.91 ± 0.11	10.7 ± 7.3
90	5.46 ± 0.05	3.8 ± 1.2
100	5.73	0.0

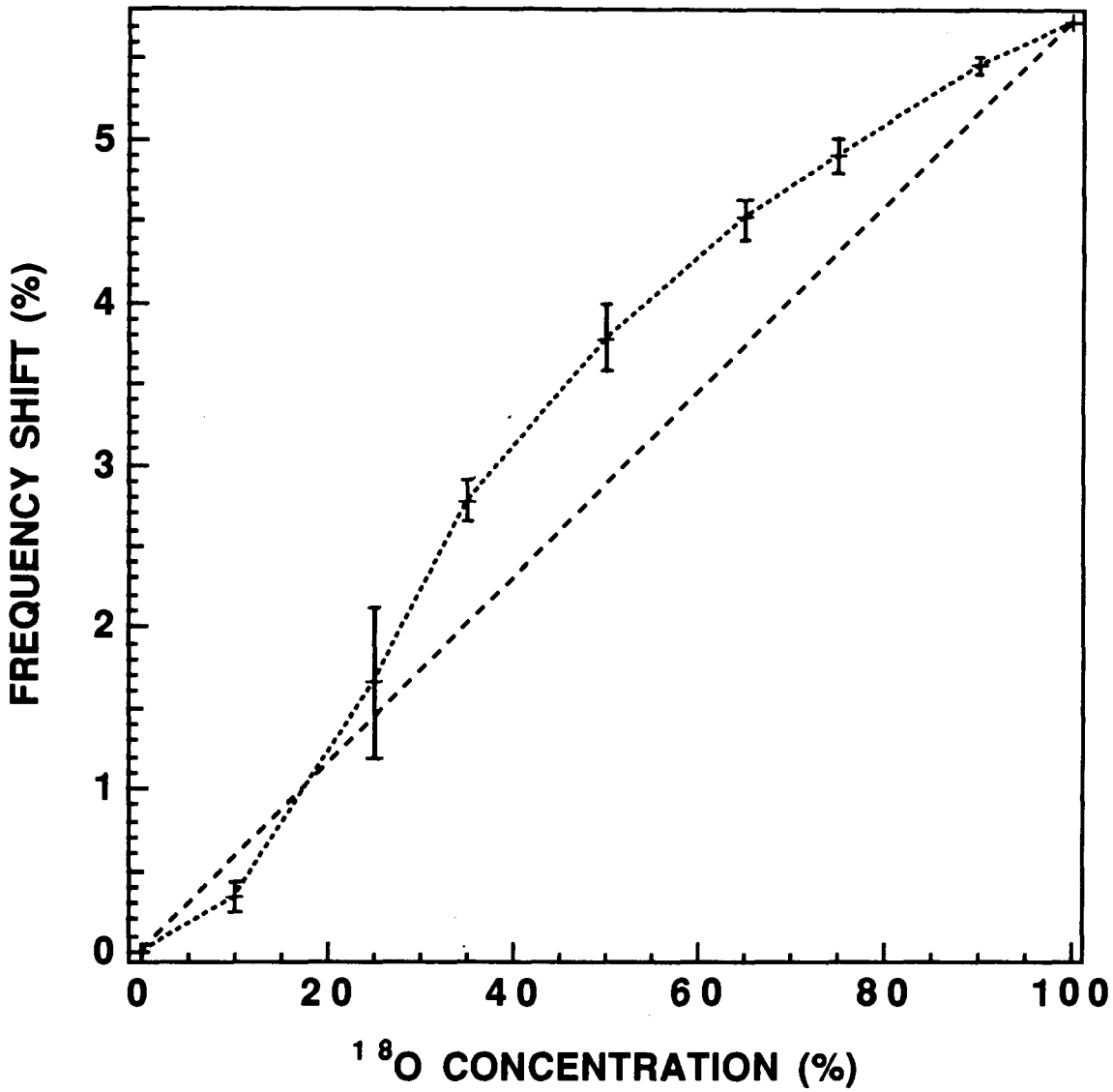

Figure 5.4

Chain model calculations (data points with error bars) indicating predicted isotopic frequency shift of the 502 cm^{-1} line vs. ^{18}O concentration [percentage of O(4) sites exchanged]. The isotopic shift is expressed as a percentage of the 502 cm^{-1} position. The dashed line connecting the points serves only as a visual aid, and the straight dashed line indicates a linear variation for comparison.

random substitution of ^{18}O atoms into the ^{16}O chain, localized modes involving ^{16}O or ^{18}O clusters are generated. These modes also involve motion of the Cu atoms and the much greater mass of the Cu tends to depress the frequencies independent of the isotopic chain involved. Thus the frequency shift induced by the ^{18}O substitution is enhanced and that resulting from ^{16}O substitution reduced. This asymmetry between ^{18}O doping and ^{16}O doping results in a nonlinear dependence of the Raman shift and linewidth on the concentration of exchanged ^{18}O atoms.

The application of the linear chain model has also yielded another interesting result. As the disorder is increased by random substitution of ^{18}O atoms on the O(4) sites, an additional small peak (Fig. 5.3) appears in the calculated spectrum at about 550 cm^{-1}. This peak corresponds to clustering in the distribution of ^{16}O and ^{18}O atoms along the chain. A feature at about this frequency has been observed previously in Raman spectra obtained at elevated temperatures and in samples that were assumed to be disordered to some extent because of oxygen deficiency [88Mb]. The appearance of this peak was attributed to disorder induced activity of the infrared active mode at about 560 cm^{-1}. It is interesting but not conclusive that the simple linear chain model used here also predicts the occurrence of a disorder induced feature in the same spectral region.

Finally, a comparison of Fig. 5.5 and Table 5.3 indicates an ^{18}O concentration in some of the experimental samples that is less than 50%. This is in contrast with the overall ^{18}O concentration which is estimated to be greater than 80% in samples A-H, by SIMS measurements, and about 50% in sample Z_2. These results are consistent, however, with the earlier suggestion that the O(4) site is exchanged to a lesser degree than the remaining oxygen sites which are essentially fully exchanged in samples A-H.

Table 5.4. Predicted sample ^{18}O concentrations using chain model and linear variation assumption for the substituted sample in polycrystalline sample pairs A,B,C,D,E,F,H, and Z. All concentrations are in terms of percentage of O(4) sites occupied by ^{18}O, i.e. [$^{18}O(4)/^{16}O(4)$]. Estimated uncertainties are indicated in the first row.

Sample	Chain Model	Linear variation	Difference
A_1, A_2	62.5 ± 4.0	76.9	14.4 ± 4.0
B_1, B_2	76.2	80.3	13.7
C_1, C_2	43.3	59.4	16.1
D_1, D_2	46.5	62.9	16.4
E_1, E_2	35.5	48.9	13.4
F_1, F_2	31.4	41.9	10.5
H_1, H_2	33.4	45.4	12.0
Z_1, Z_2	18.2	15.7	-2.5

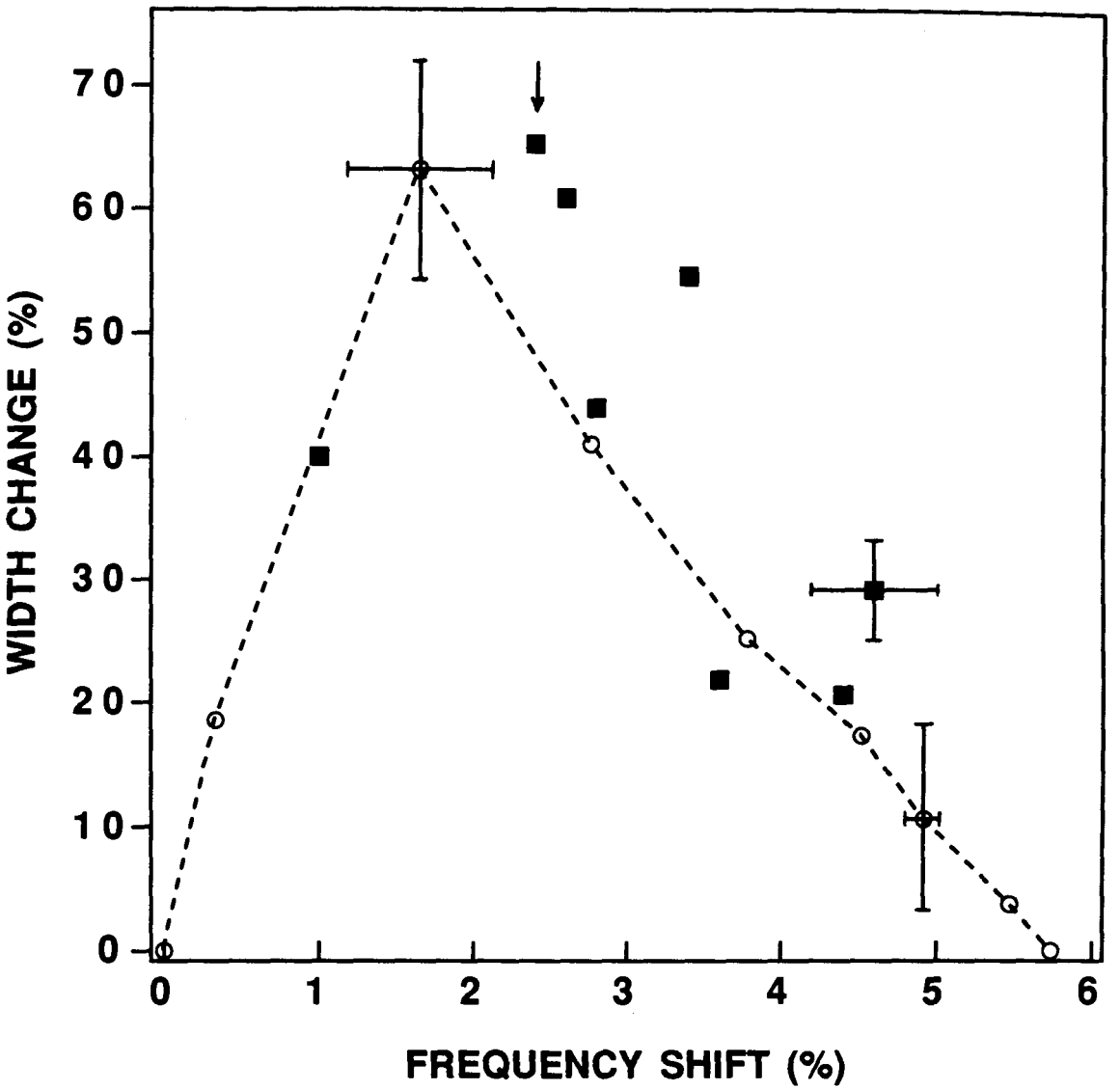

Figure 5.5

Change in the full width at half maximum (FWHM) vs. isotopic frequency shift for the 500 cm^{-1} line. All changes and shifts are relative to, and percentages of, the ^{16}O peak at 502 cm^{-1}. The results of the chain model calculations are indicated by open circles and experimental data points by closed squares. Typical error estimates are shown and the dashed line connecting the theoretical points serves only as a visual aid. The estimated position of the maximum FWHM is indicated by the arrow.

CHAPTER 6

SINGLE CRYSTAL TEMPERATURE DEPENDENCES

6.1 $YBa_2Cu_3O_7$ crystals grown in thoria crucibles

6.1.1 Introduction

The preparation and characterization of the crystals investigated in this section is described in chapter 4. Although these crystals are essentially fully oxygenated, they do contain a significant level of about 8700 ppm by weight of thorium which acts as an electron doping impurity, reducing the critical temperature to about 89.5 K.

Both (ab) and (zz) spectra were obtained from the crystals. More details on these scattering geometries can be found in section 4.1 of chapter 4. Typical spectra for both scattering geometries are shown in Fig. 6.1 for a sample temperature of 200 K. Note in particular that the frequencies of the 500 and 440 cm^{-1} modes, and the absence of the 235 cm^{-1} defect mode, both imply an essentially fully oxygenated crystal. Spectra identical to those shown in Fig. 6.1 were obtained from three different crystals, and in addition, the spectra were unaffected by dry polishing or etching in a 1% bromine ethanol solution [89W], indicating that the spectra are representative of the bulk of the crystals.

6.1.2: 340 cm^{-1} phonon

The B_{1g} like symmetry (tetragonal notation) of this phonon (see chapter 3) is consistent with its absence in the (zz) spectra of the crystals as shown in Fig. 6.1(b). All measurements of this phonon are therefore obtained

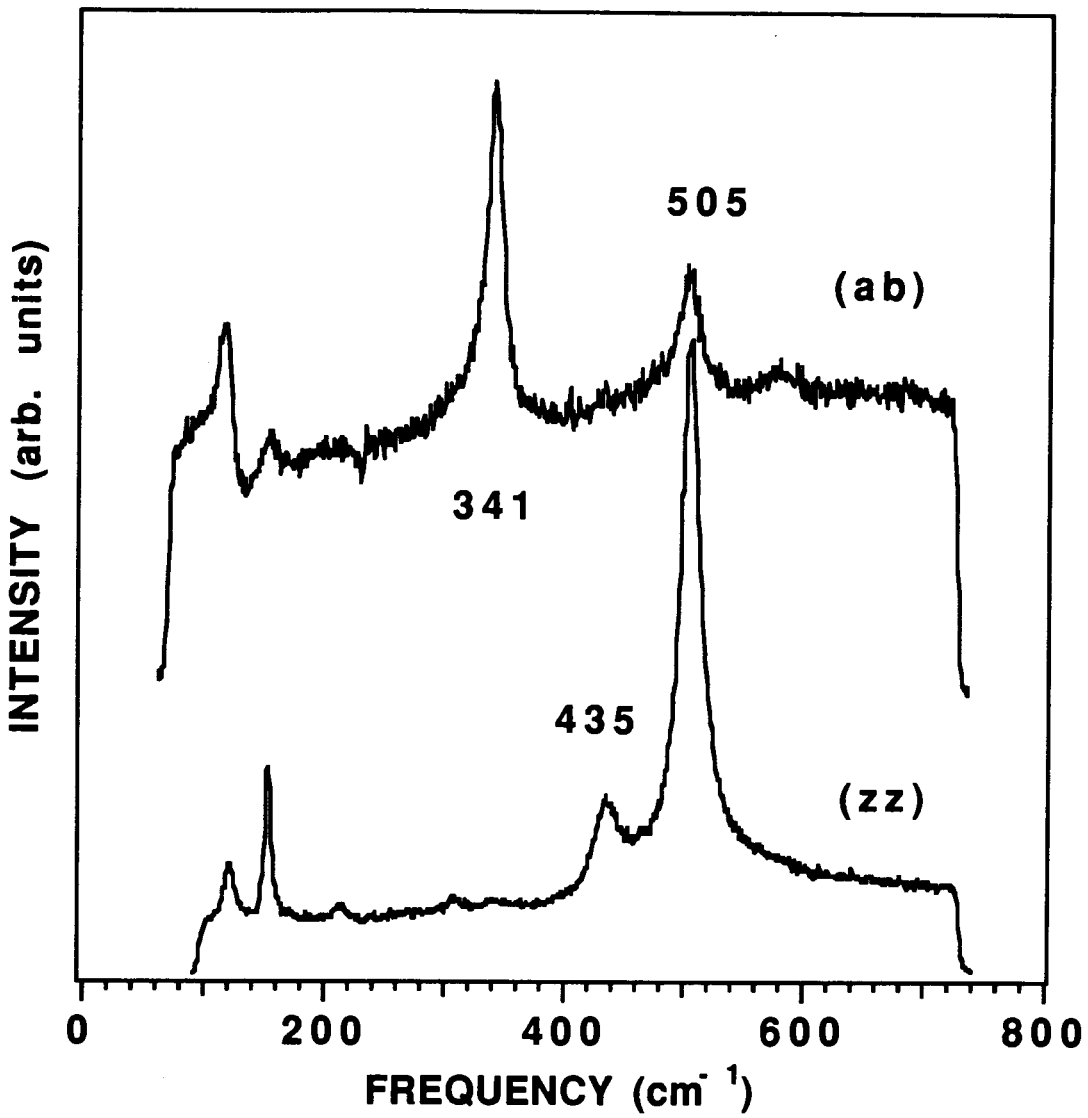

Figure 6.1

Raman spectra obtained at 200 K with the incident and scattered light polarized in the a-b plane ((ab) spectra) and along the c-axis of the crystal ((zz) spectra). Spectra offset for clarity.

from (ab) spectra with the incident light polarized in the ab plane of the crystal. Stated frequencies and linewidths (FWHM) of this phonon correspond to the values obtained by numerically fitting the observed lineshape to the Fano profile given by equation 2.28 of chapter 2, combined with a constant background term (B_o).

The resulting frequencies and linewidths obtained from spectra taken at temperatures ranging from 300 K (room temperature) down to 15 K are shown in Figs. 6.2(a) and 6.2(b) respectively. The frequency of the 340 cm^{-1} phonon clearly softens near T_c by about 3 cm^{-1}. This softening is qualitatively similar to that reported previously [87M] [89T] [88Kc] [90I], but is significantly smaller in magnitude than the value of about 8 cm^{-1} obtained by Cooper et al. [88Cb] and Friedl et al. [90Fb] for example. The linewidth temperature dependence of this same mode shown in Fig 6.2 (b) is however clearly different than that reported previously. For example, Cooper et al. [88Cb] found that the linewidth of this phonon abruptly increased by about 10.0 cm^{-1} as the temperature was reduced below T_c. In the present case the linewidth actually appears to decrease by about 1.5 cm^{-1} as the temperature is lowered below T_c. The dashed line in Fig. 6.2(b) is a plot of the expected linewidth variation based on the anharmonic decay [66K] of the 340 cm^{-1} phonon into two acoustic phonons each with half the frequency of the 340 cm^{-1} phonon, as described in chapter 2. The resulting analytic expression (equation 2.27) for the linewidth as a function of temperature was fitted to the data points above T_c.

The present results thus appear to differ rather dramatically from the measurements of other groups [88Cb] [90Fb], however, this difference may be consistent with the suggestion [90Fb] [90Z] [88Cc] that the frequency of the 340 cm^{-1} mode is comparable to the superconducting gap energy, 2Δ, where large

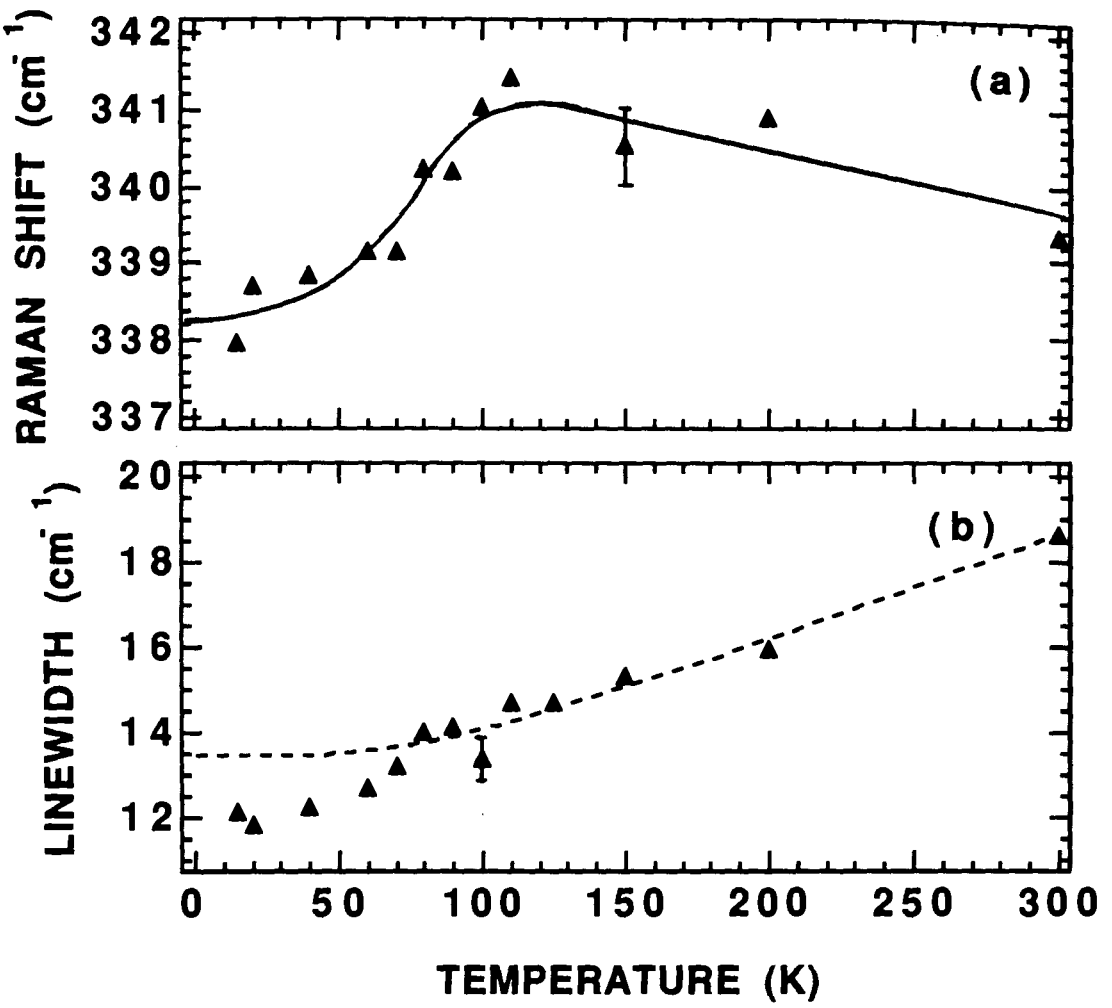

Figure 6.2

The frequency (a) and linewidth (FWHM) (b) of the 340 cm^{-1} phonon as a function of temperature. The solid curve in Fig. 2(a) is intended to serve only as a guide to the eye. The dashed line in Fig. 2(b) is the calculated linewidth variation assuming an anharmonic decay [66K] of the 340 cm^{-1} mode into two phonons with smaller but equal energy (equation 2.27).

variations in the frequency and linewidth are expected as a function of temperature and doping, due to relatively small changes in 2Δ.

6.1.3 440 cm^{-1} phonon

Estimates for the frequencies and linewidths of this mode were obtained by eye from (zz) spectra taken at temperatures ranging from 300 K to 15 K. The resulting frequency and linewidth temperature dependences are shown in Fig. 6.3(a) and 6.3(b) respectively. As is evident from a comparison of Figs. 6.2 and 6.3, the behavior of this mode, as the sample temperature is reduced below T_c, is quite different from the previously discussed behavior of the 340 cm^{-1} phonon. The frequency of the 440 cm^{-1} mode increases by about 3.0 cm^{-1} as the sample is cooled from 100 to 15 K. In this same temperature range the linewidth also increases by about 4.0 cm^{-1} over what one would expect from the anharmonic decay mechanism (equation 2.27) [66K] which was fit to the data points above T_c and is represented by the dashed line in Fig. 6.3(b). These temperature dependences are similar to those observed by other groups [90Ta] [90Fb] in polycrystalline samples. McCarty et al. [90Mb] [91Ma] [92Ma], however, from measurements carried out on single crystals with transition temperatures of about 90 K, state that the 440 cm^{-1} phonon exhibits decreased or unchanged damping for temperatures below T_c, in contrast to the results obtained for this sample. In particular, the increase in linewidth below T_c shown in Fig. 6.3(b) implies an increase in the damping of the 440 cm^{-1} phonon corresponding to the crystal being investigated here. The reason for these differences is not known, but may be related to the small amount of thoria (2.5% by weight) present in the crystals investigated here.

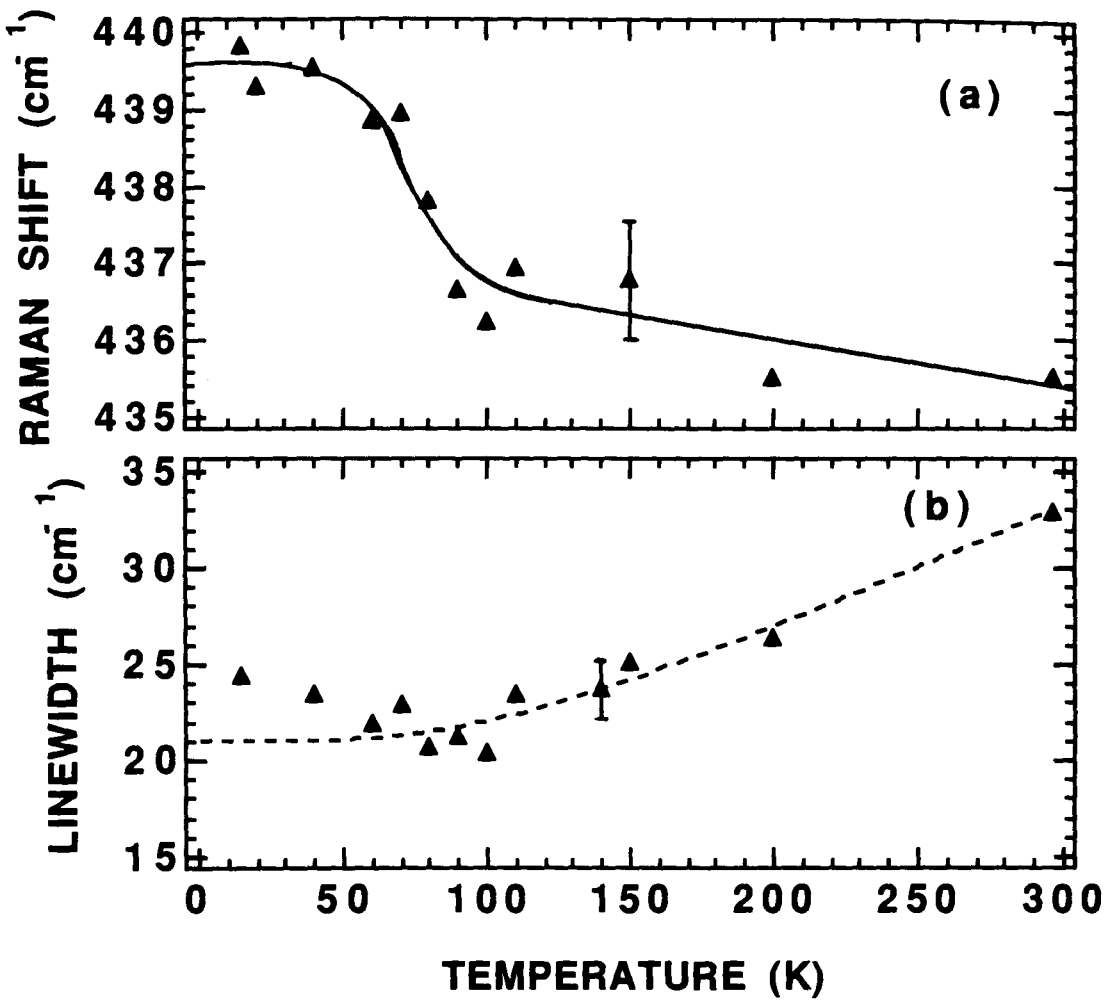

Figure 6.3

The frequency (a) and linewidth (FWHM) (b) of the 440 cm^{-1} mode as a function of temperature. The solid curve in (a) serves only as a guide to the eye and the dashed line in (b) is the calculated linewidth assuming anharmonic decay into two phonons of lower but equal energy (equation 2.27).

6.1.4 500 cm^{-1} phonon

The frequencies and linewidths of this phonon were obtained from both the (ab) and (zz) spectra due to the strong Raman cross-section of this mode. The 500 cm^{-1} phonon peaks in the (zz) spectra were very symmetric and Fano fits to these profiles yielded Fano parameter magnitudes of $|q| > 1000$. The frequencies and linewidths of the 500 cm^{-1} mode in the (zz) spectra were therefore determined by fitting the observed (zz) peaks to Lorentzian profiles (equation 2.26) with a constant background. The 500 cm^{-1} peaks in the (ab) spectra were significantly less symmetric ($|q| \geq 10$), particularly for $T > T_c$, and hence were fitted using Fano profiles (equation 2.28) combined with a linear background. The different q parameters required to fit the 500 cm^{-1} phonon in the two scattering geometries suggest that this phonon may interact more strongly with charge fluctuations in the a-b plane than it does along the c-axis.

A comparison of Figures 6.3 and 6.4 indicates that the frequency temperature dependences of the 440 and 500 cm^{-1} modes are qualitatively similar in that both modes show a distinct hardening or increase in frequency by about 3 cm^{-1} as the sample temperature is reduced from 100 K to 15 K. In contrast to the 440 cm^{-1} mode, however, the 500 cm^{-1} mode frequency appears to reach a maximum at about 50 K and then plateau (or perhaps even decrease) as the temperature is further lowered to 15 K.

The linewidth temperature dependence of the 500 cm^{-1} phonon is also similar to that of the 440 cm^{-1} phonon in that the linewidth decreases as the temperature is lowered from 300 K, reaches a minimum at $T \approx T_c$, and then steadily increases as the temperature is lowered to 15K.

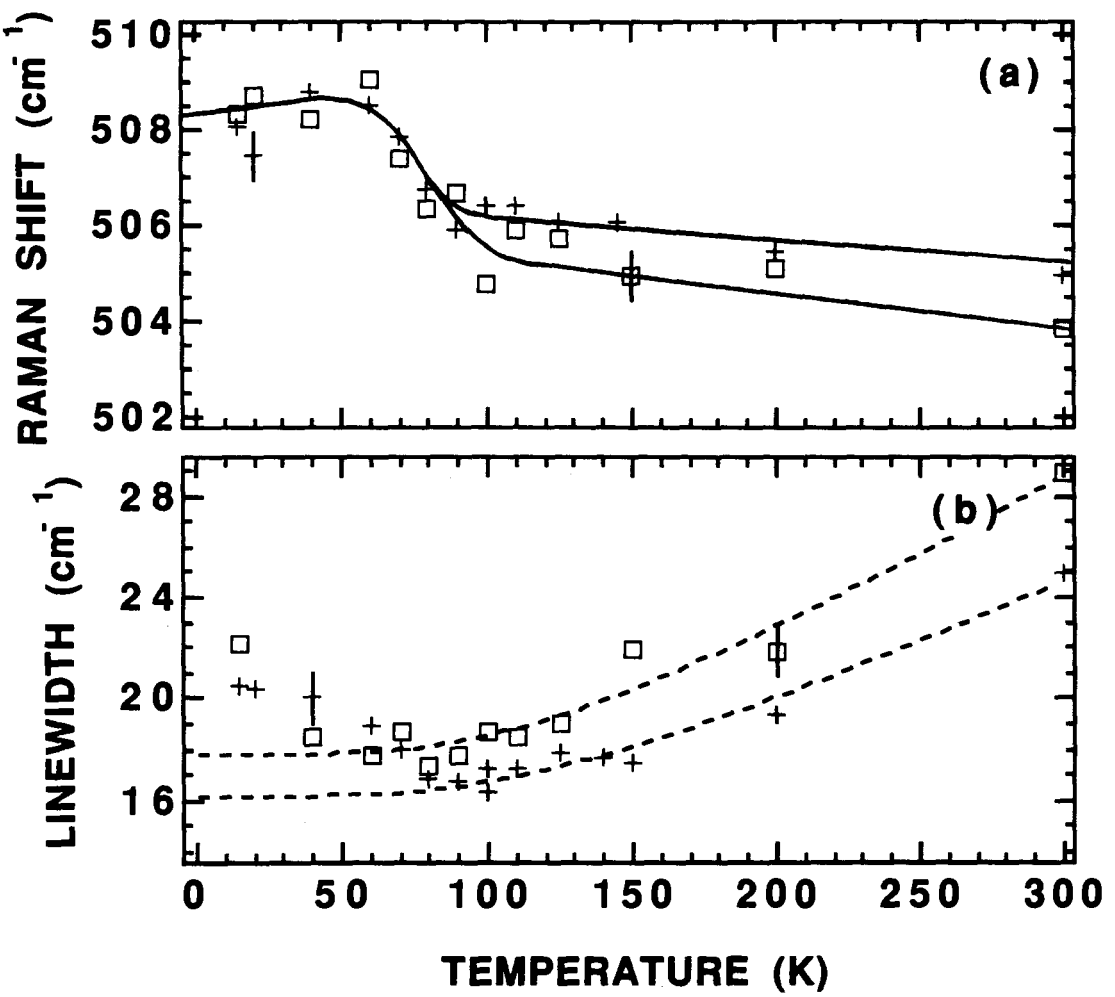

Figure 6.4

The frequency (a) and linewidth (FWHM) (b) of the 500 cm^{-1} phonon as a function of temperature. The open squares represent values obtained from Fano fits to (ab) spectra and the crosses correspond to values obtained from Lorentzian fits to the (zz) spectra. The solid lines in (a) only serve as a guides to the eye while the dashed lines in (b) are the calculated linewidth variations assuming a decay of the 500 cm^{-1} phonon into two phonons with smaller but equal energy (equation 2.27).

The above temperature dependences in the frequency and linewidth of the 500 cm^{-1} mode, are qualitatively the same in both (ab) and (zz) scattering geometries and appear equivalent within experimental uncertainties for $T < T_c$. For temperatures greater than T_c, however, some differences do appear. For example, the room temperature frequencies obtained in the (ab) and (zz) geometries differ by about 1 cm^{-1}, while for $T > 150$ K, the linewidth measured in the (ab) geometry is about 4 cm^{-1} larger than that obtained from the (zz) spectra. These differences may reflect anharmonic interactions which are anisotropic. This possibility is in effect modelled by the two anharmonic curves of Fig. 6.4(b) which provide reasonable agreement with the linewidths obtained from the Fano fits ((ab) spectra-open squares) and from the zz spectra (Lorentzian fits-crosses) for $T > T_c$.

6.1.5 Comparisons with Strong Coupling Theory

As mentioned in chapter 2, Eliashberg theory can be used [73A] [75S] [90Z] to interpret the anomalous changes in the phonon linewidth and frequency that occur for temperatures below T_c. In particular, the the superconductivity induced frequency change can be expressed as

$$\Delta\omega_\nu = \frac{\lambda_\nu \omega_\nu}{2} \mathrm{Re}\{f(\tilde{\omega})\} \qquad (6.1),$$

where λ_ν is the electron-phonon coupling constant for the vth phonon, $\tilde{\omega}$ is the phonon frequency divided by the superconducting gap energy;$\tilde{\omega} = \omega_\nu / 2\Delta$, and $f(\tilde{\omega})$ is a function which is dependent on the temperature and scattering rate. Similarly, the change in the linewidth (HWHM) due to superconductivity is given by

$$\Delta\gamma_v = -\frac{\lambda_v \omega_v}{2} \mathrm{Im}\{f(\tilde{\omega})\} \qquad (6.2).$$

Zeyher and Zwicknagl [90Z] have calculated the real and imaginary parts of $f(\tilde{\omega})$ for various temperatures below T_c and for different scattering times. The results of these calculation are presented in Figs. 3 to 6 of reference [90Z]. In order to compare these calculations to experimental measurements, values for the electron-phonon coupling constants λ_v must first be obtained. Rodriguez et al. [90R] and Cohen et al. [90C] have independently determined values of λ_v for the Raman modes of $YBa_2Cu_3O_7$, from band structure calculations. These electron phonon coupling constants are listed are listed in Table 6.1. It should be noted that the values presented in the second row of Table 6.1 are average values given by Cohen et al. [90C] which were renormalized by dividing by three times the number of atoms in the unit cell and multiplying by 2, the number of spin states. This procedure yields sets of values that are normalized on the same basis as those due to Rodriguez et al. [90R].

Zeyher and Zwicknagl [90Z] have calculated the real and imaginary parts of the function $f(\tilde{\omega})$ for various scattering times and at a temperature of $T = 0.16\ T_c$ ($T \approx 14$ K). Their results are reproduced in Figs. 6.5 and 6.6 for four scattering times ($\tau = \infty, \frac{1}{0.33(2\Delta)}, \frac{1}{2\Delta}, and\ \frac{1}{3(2\Delta)}$). In Fig. 6.5 the normalized frequency shifts, $2(\Delta\omega_v)/\lambda_v\omega_v$, are compared to the theoretical curves $\mathrm{Re}\{f(\tilde{\omega})\}$ for all three modes. Here $\Delta\omega_v$ is the frequency shift measured when the sample is cooled from 90 K to 15 K (i.e. $\omega_V(15) - \omega_V(90)$). The normalized frequency shifts have been determined using both the coupling constants of Rodriguez et al. [90R] and Cohen et al. [90C] (see Table 6.1). The normalized

shifts determined using the coupling constants of Rodriguez et al. are indicated by closed circles while those determined using the coupling constants of Cohen et al. are indicated by open circles.

Table 6.1. Calculated electron-phonon coupling constants λ_ν for the 340, 440 and 500 cm^{-1} modes of $YBa_2Cu_3O_7$ [[90R], [90C]].

Mode	340	440	500
λ_ν (ref. [90R])	0.02	0.01	0.009
λ_ν (ref. [90C])	0.051	0.041	0.010

It is apparent from Fig. 6.5 that a better agreement between theory and experiment is obtained using the coupling constants of Rodriguez et al [90R].

In Fig. 6.6, the normalized measured linewidth shifts $-2(\Delta\gamma_\nu)/\lambda_\nu\omega_\nu$ occurring between the data points and the anharmonic decay curve, at 15 K, are also compared to the theoretical curves $\mathrm{Im}\{f(\tilde{\omega})\}$ reproduced from Zeyher and Zwicknagl [90Z] for the four scattering times ($\tau=\infty$, $\frac{1}{0.33(2\Delta)}$, $\frac{1}{2\Delta}$, *and* $\frac{1}{3(2\Delta)}$). Again the results using both sets of coupling constants (Table 6.1) for the linewidth normalization are shown in Fig. 6.6 and again those of Rodriguez et al. [90R] yield the best agreement.

In carrying out the linewidth comparisons, no corrections have been made to account for the effects of dispersion in the real part of the phonon self energy Σ_1. Consideration of these effects as described in chapter 2 (and using Fig. 6.5), result in a linewidth estimate for the 340 cm^{-1} mode which is

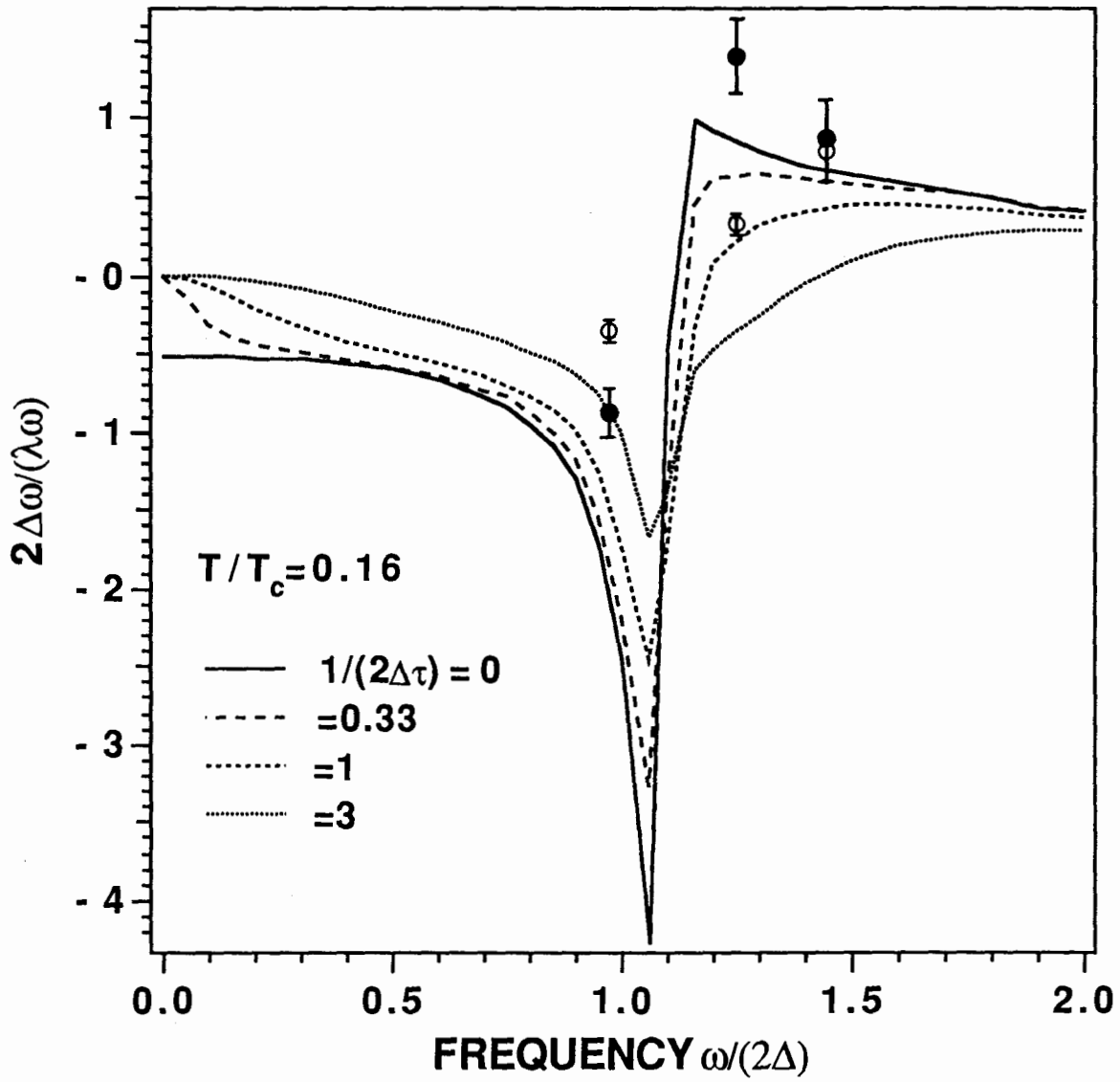

Figure 6.5

A comparison of the normalized measured frequency shifts $2\Delta\omega_\nu / (\lambda_\nu \omega_\nu)$ occurring between 90 and 15 K with the calculated curves of the real part of $f(\tilde{\omega})$ (from Fig. 5 of ref. [90Z]) for the four different scattering times; $1/(2\Delta\tau)$ = 0, 0.33, 1.0, 3.0. Experimental values obtained with λ_ν of ref. [90R] (closed circles) and ref. [90C] (open circles) are both shown (see table 6.1).

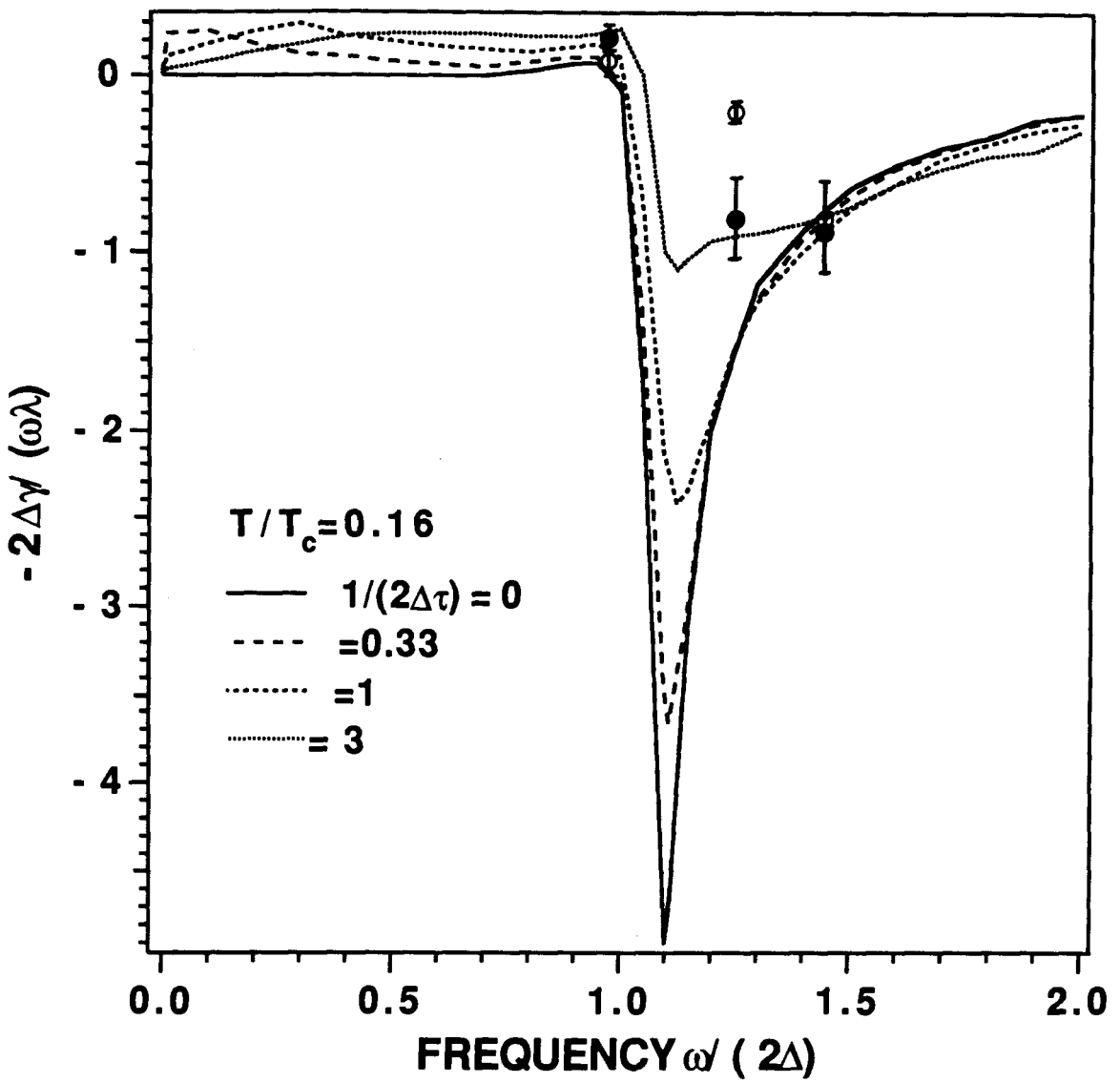

Figure 6.6

A comparison of the normalized measured shifts in linewidth $-2\Delta\gamma_\nu / (\lambda_\nu \omega_\nu)$ occurring at 15 K with the calculated curves of the imaginary part of $f(\tilde{\omega})$ (from Fig. 6 of ref. [90Z]) for the four different scattering times; $1/(2\Delta\tau)$ = 0, 0.33, 1.0, 3.0. Experimental values obtained with λ_ν of ref. [90R] (closed circles) and ref. [90C] (open circles) are both shown (see table 6.1).

approximately 6% greater than the measured value for $T < T_c$. This correction when applied to the low temperature points of Fig. 6.2(b) results in a linewidth which may be a small amount ($\approx$0.5 cm^{-1}) greater than the data points shown in Fig. 6.2(b). This in turn implies that the magnitude of the linewidth narrowing corresponding to the 340 cm^{-1} phonon in Fig. 6.6 may be slightly less than indicated. Similar corrections to the 440 and 500 cm^{-1} modes are negligible since Σ_1 has a very small dispersion in this frequency range (see Fig. 6.5).

It is apparent from Figs. 6.5 and 6.6 that no pair of strong coupling curves corresponding to a given scattering rate, quantitatively agree with the data points for all three phonons within the experimental uncertainties. This is true even for the data points obtained with the coupling constants of Rodriguez et al. [90R], and in addition, adjusting the values of the coupling constants cannot remove the inconsistencies.

An upper and lower limit to the magnitude of the superconducting gap energy, 2Δ, can however be estimated from the frequency of the 440 cm^{-1} phonon which hardens below T_c ($2\Delta \lesssim 380$ cm^{-1}) and the linewidth of the 340 cm^{-1} phonon which narrows below T_c ($2\Delta \gtrsim 350$ cm^{-1}). As the crystal being investigated is essentially fully oxygenated, and contains a relatively low concentration of impurities, the scattering rate is expected to be small and hence the $1/(2\Delta\tau)$=0.33 curves were used to determine the above limits. The lower limit of 350 cm^{-1} was used to position the experimental data points along the horizontal axes of Figs. 6.5 and 6.6.

Alternatively, it may be more reasonable to conclude that a single gap s-wave strong coupling theory may not adequately describe the superconductivity induced renormalization of all three phonons at 340, 440, and 500 cm^{-1}. More specifically, the 440 and 500 cm^{-1} phonons, for instance,

may interact with a different gap or distribution of electrons than the 340 cm^{-1} phonon as has been suggested previously [90Ta]. If the 340 cm^{-1} phonon alone, with the coupling constant of Rodriguez et al. (λ=0.02) [90R], is used in conjunction with the $1/2\Delta\tau$=0.33 strong coupling curves of Figs. 6.5 and 6.6, then an estimate of $2\Delta = 425 \pm 30$ cm^{-1} ($6.7k_BT_c \pm 0.5k_BT_c$) is obtained for the superconducting gap energy. A similar estimate for the gap value corresponding to the 440 and 500 cm^{-1} phonons is not as readily obtained since the experimental data points do not match any pair of strong coupling curves to within the experimental uncertainties (error bars). As previously mentioned, however, an upper limit of 2Δ = 380 cm^{-1} is suggested by the hardening of the 440 cm^{-1} phonon frequency below T_c.

All of the above estimates for 2Δ are significantly higher than the value of 2Δ = 316 cm^{-1} obtained by Friedl et al. [90Fb]. This variation in the obtained gap values reflects the differences in behavior of the 340 cm^{-1} phonon which broadens dramatically below T_c in the samples of Friedl et al. [90Fb] in contrast with the behavior discussed above and shown in Fig. 6.2(b). It is suggested that this phonon behavior (and the resulting larger estimates of 2Δ) is due to the presence of thoria impurities which result in a reduced hole concentration. This hypothesis is investigated further in the next section.

6.2 $YBa_2Cu_3O_y$ single crystals with $6.7 \lesssim y \leq 7.0$

6.2.1 Introduction

The results presented in the previous section (6.1) suggest that the presence of hole donor or acceptor impurities (e.g. thorium), or more generally variations in the hole concentration, may strongly affect the behavior of the phonon modes below T_c and hence the derived value of the superconducting gap energy in $YBa_2Cu_3O_7$. The frequency shifts and

linewidth changes of the 340 cm^{-1} mode below T_c appear to be particularly susceptible to such effects. In the previously discussed crystal (section 6.1), for example, a relatively small amount of thorium (8700 ppm by weight) appears to have completely removed the broadening of the 340 cm^{-1} mode below T_c observed by other workers [88Cb] [90Fb] in crystals with essentially the same T_c ($\approx$ 90 K) as the crystals investigated in section 6.1. This in turn has suggested slightly larger gap values ($2\Delta \gtrsim 350$ cm^{-1}) for the crystal discussed in the previous section than the values obtained by the above mentioned researchers ($2\Delta \approx 300$ cm^{-1}) [90Fb].

To confirm the hypothesis suggested above in a systematic manner, crystals obtained from seven different batches with different oxygen concentrations were investigated. These crystals labeled A, B, C, D, E, F, and G, are described in chapter 4 and listed in Table 4.2 along with their transition temperatures, transition widths, c-axis spacings and estimated oxygen concentrations which range from y = 6.67 to y = 7.0 (fully oxygenated). Since increasing oxygen concentrations, y in $YBa_2Cu_3O_y$, correspond to increasing hole concentrations, a Raman investigation of these crystals should determine whether, and to what extent, the hole concentration affects the phonon behavior below T_c.

Unlike the previous crystals which were grown in thoria crucibles and hence contain some thorium as an impurity, the crystals described in this section do not appear to contain any significant levels or amounts of heavy metal impurities ($\lesssim$ 500 ppm by weight (total)). The main factor in determining the hole concentration in these crystals should therefore be the oxygen content. A more detailed description of the preparation and characterization of these crystals can be found in chapter 4.

6.2.2 Raman spectra

Raman spectra were obtained from crystals A,B,C,D,E,F, and G, with the incident light polarized in the a-b plane ((ab) spectra) and typical examples obtained at room temperature from crystals A and E are shown in Fig. 6.7(a). Spectra have also been obtained from the edges of the crystals with the incident and scattered light polarized parallel to the c-axis which as before will be referred to as (zz) spectra. Typical (zz) spectra obtained at room temperature from crystals A and E are shown in Fig. 6.7(b). Just as in the previous section, the focus of attention will be on the temperature dependences of the three oxygen dependent modes with nominal frequencies of 340, 440, and 500 cm^{-1}. The additional modes at 235 and 598 cm^{-1} seen in the ab spectra of crystal E are the defect induced chain modes mentioned in chapter 3, which are thought to be [91H] the result of oxygen vacancies in the chains of the deoxygenated crystals. These modes are observed in all crystals with $y \lesssim 6.95$ in agreement with the findings of Hadjiev et al [91H].

6.2.3 The 340 cm^{-1} phonon

All measurements of this phonon were carried out with the incident light in the a-b plane of the crystals ((ab) spectra). The absence of this phonon in the (zz) spectra (Fig. 6.7(b)) is once again consistent with the fact that it has B_{1g}-like symmetry (tetragonal notation). A full discussion of this selection rule is found in chapter 3 of this thesis. Values for the frequencies and linewidths of the 340 cm^{-1} phonon were obtained by fitting the corresponding 340 cm^{-1} Raman feature to the Fano profile given by equation 2.28 plus a linear background term of the form $B\,\omega + C$ where B and C are adjustable

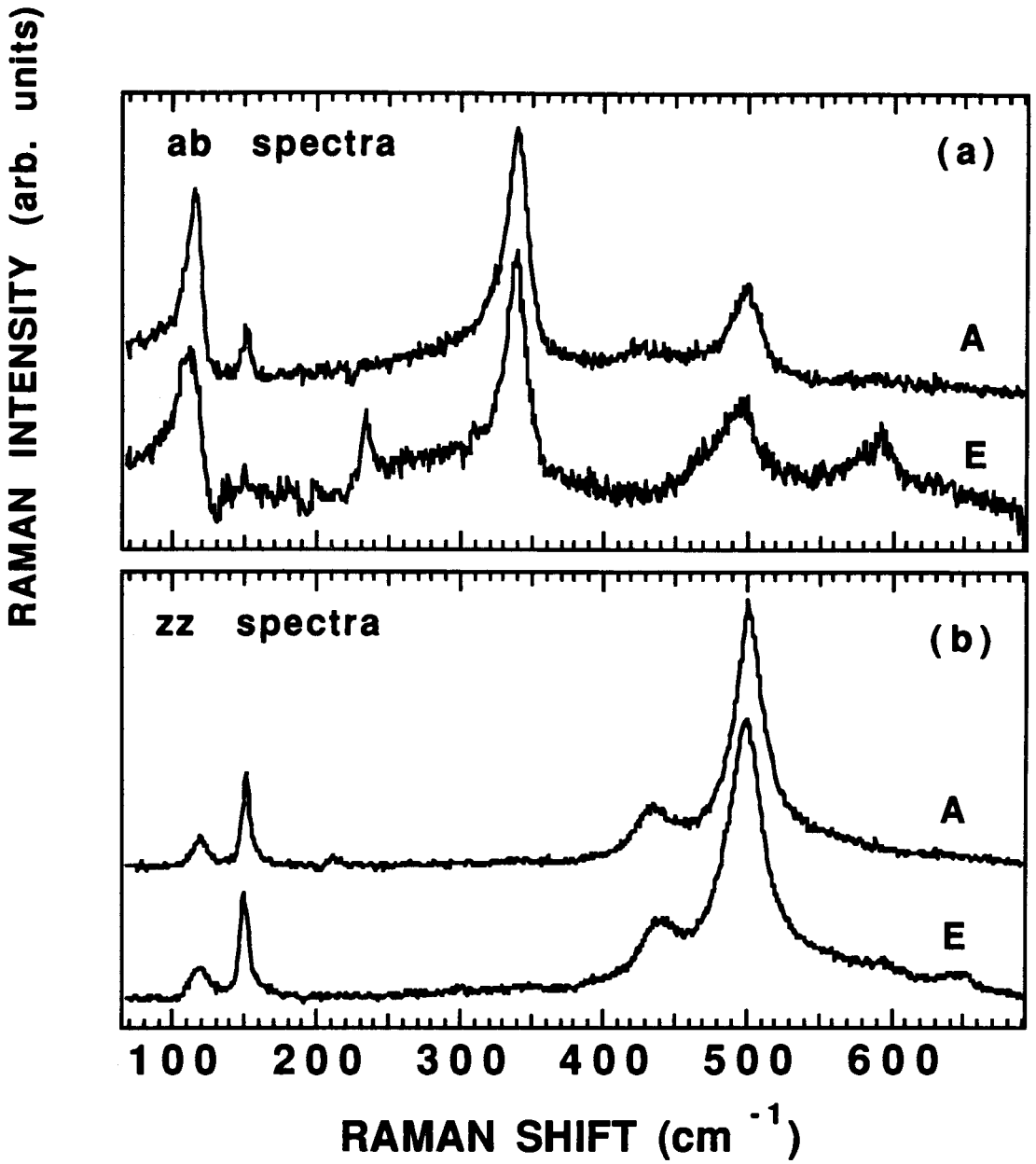

Figure 6.7

Raman spectra obtained at room temperature (295 K) from crystals A and E with the incident polarization in a) the a-b plane ((ab) spectra), b) along the c-axis of the crystal ((zz) spectra). Spectra have been offset for clarity.

parameters. An example of such a fitted profile is shown in Fig. 6.8 superimposed on the experimental data of crystal A at 40 K. Fits of similar quality were obtained for all the crystals described in this thesis.

In Fig. 6.9 the temperature dependences of the frequencies of the 340 cm^{-1} mode are plotted. A softening in the frequency near T_c is observed in crystals A through F in accordance with the observations of other groups [87M] [88Cb] [88Cc] [88Kc] and the results presented in the previous section (6.1). The largest shift is observed in crystal A in which the frequency softens by approximately 8 cm^{-1} between 90 K and 15 K while the amount of softening is greatly reduced in the deoxygenated crystals and vanishes in crystal G. Such a reduction in the softening was also observed in deoxygenated polycrystalline samples by Krantz et al [88Kc].

The temperature dependences of the linewidths of the 340 cm^{-1} mode are shown in Fig. 6.10 for crystals A,B,C,D,E,F, and G. The solid lines in Fig. 6.10 indicate a fit of the experimental data points above T_c to the model of anharmonic decay [66K] described in chapter 2 and given by equation 2.27. Crystal C (T_c = 93.7 K) shows an overall narrowing below T_c of about 2 cm^{-1} as indicated by the departure of the experimental data points from the anharmonic decay curve while for crystals D,E and F (y = 6.9 to about y = 6.8) the degree of narrowing increases by approximately 1 cm^{-1}. Finally, linewidth broadening below T_c in a manner similar to that reported by other groups [88Cb] [88Kc] [90Fb] is observed in crystals A and B which are essentially completely oxygenated (y = 7.0). It therefore appears that the oxygen content, or more generally the hole concentration, is the dominant factor in determining the nature of the superconductivity induced linewidth and frequency shifts of the 340 cm^{-1} mode in these crystals. The enhanced broadening observed in crystal A, is perhaps partially linked to the presence of

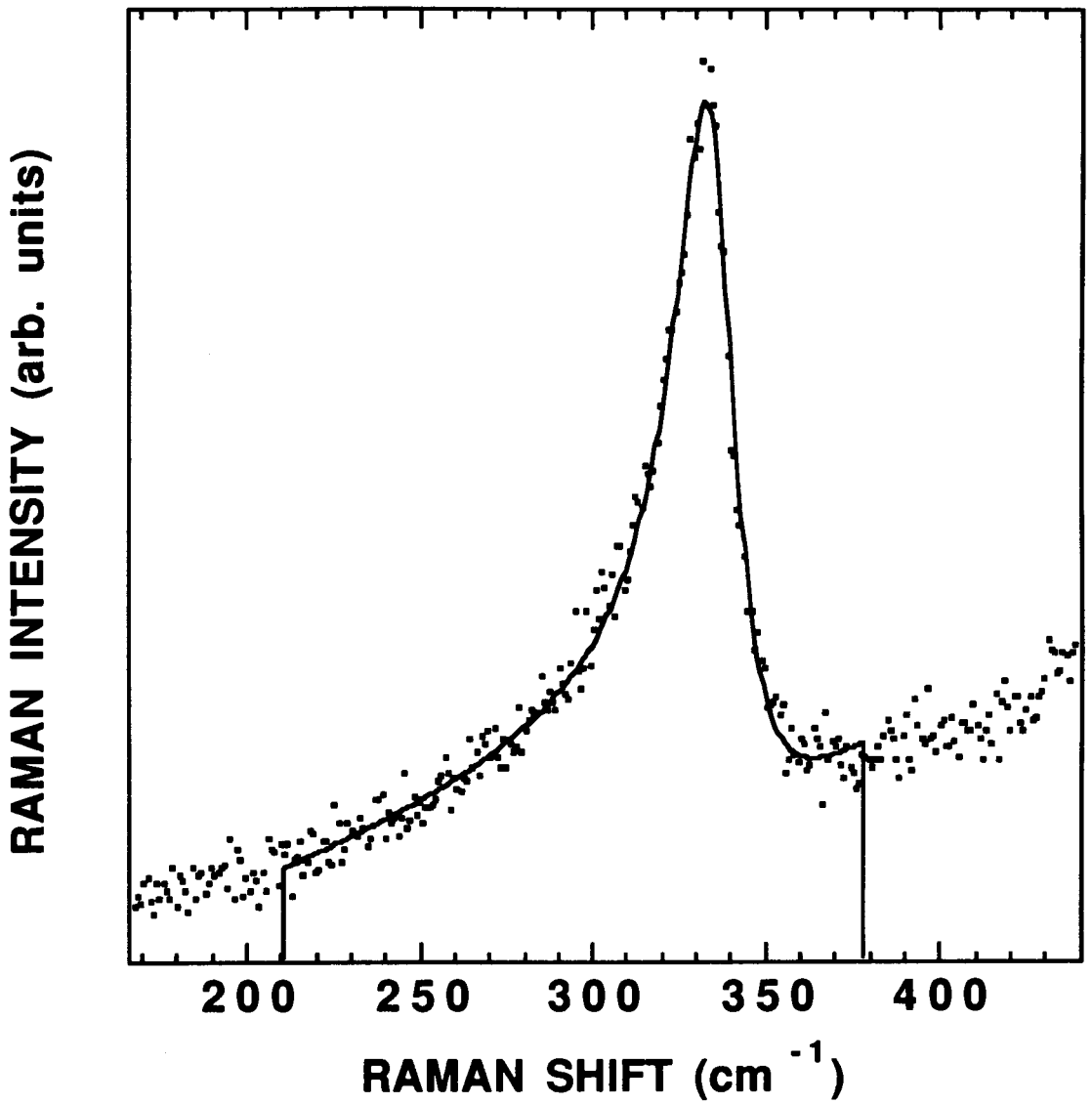

Figure 6.8

The 340 cm^{-1} Raman peak obtained at 40 K in the (ab) geometry from crystal A (dots), and corresponding fitted Fano profile (equation 2.28) with linear background (solid line).

Figure 6.9

Frequencies of the 340 cm^{-1} phonon as a function of temperature for (a) crystal A (y=7.0, T_c=89.7 K), (b) crystal B (y=6.99, T_c=92.8 K), (c) crystal C (y=6.93, T_c=93.7 K), (d) crystal D (y=6.90, T_c=92.0 K), (e) crystal E (y=6.86, T_c=91.1 K), (f) crystal F (y=6.81, T_c=87.7 K), and (g) crystal G (y=6.68, T_c=59.2 K). The solid lines are only intended to serve as guides to the eye. The data point with error bar in each graph indicates the experimental uncertainty.

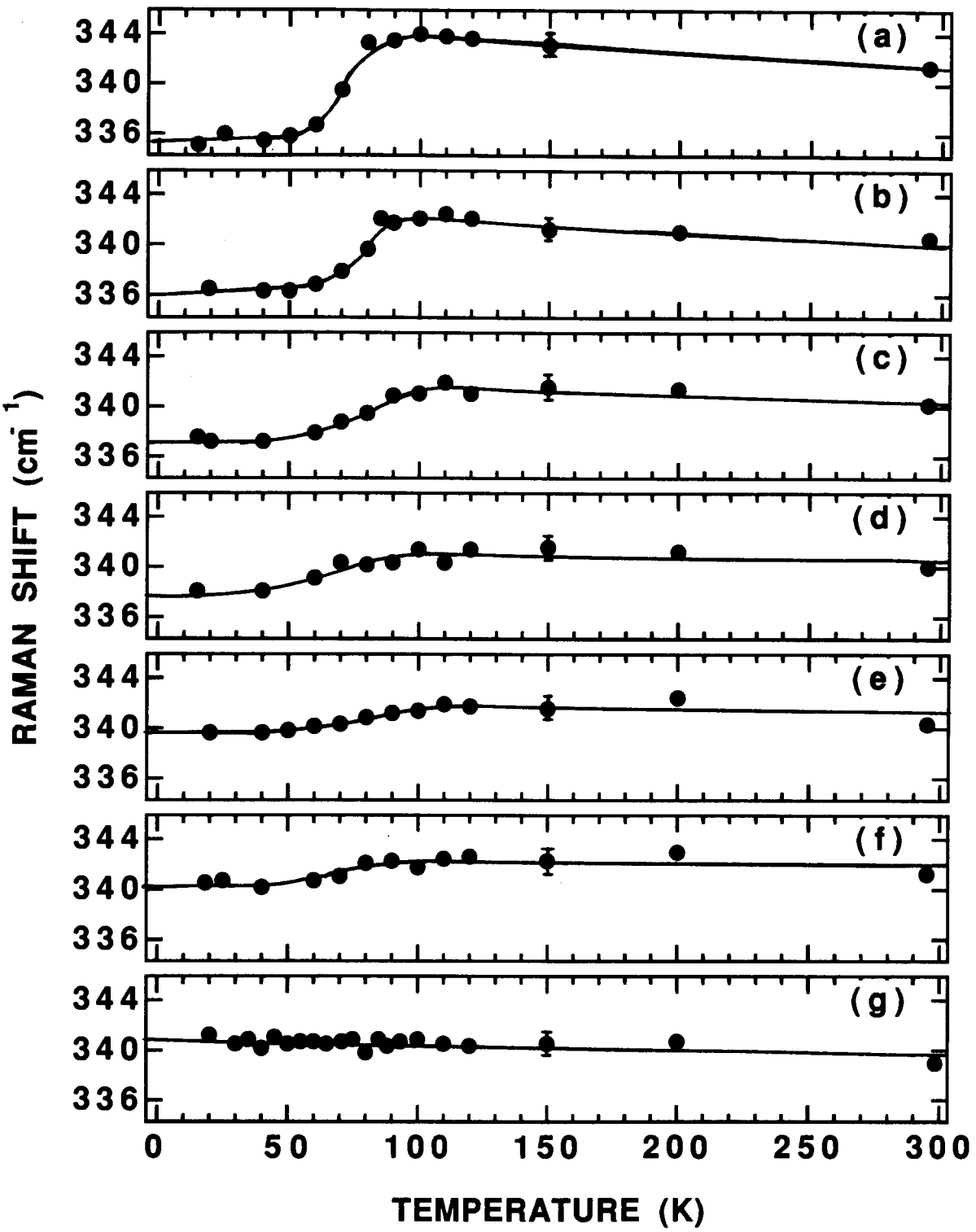
RAMAN SHIFT (cm^{-1})
344
340
336
(a)
(b)
(c)
(d)
(e)
(f)
(g)
0
50
100
150
200
250
300
TEMPERATURE (K)

Figure 6.10

Linewidths (FWHM) of the 340 cm^{-1} phonon as a function of temperature for (a) crystal A (y=7.0, T_c=89.7 K), (b) crystal B (y=6.99, T_c=92.8 K), (c) crystal C (y=6.93, T_c=93.7 K), (d) crystal D (y=6.90, T_c=92.0 K), (e) crystal E (y=6.86, T_c=91.1 K), (f) crystal F (y=6.81, T_c=87.7 K), and (g) crystal G (y=6.68, T_c=59.2 K) as determined by numerical fits to Fano profiles (equation 2.28) with a linear background. The solid lines are fits of the data above T_c to a model of anharmonic decay (equation 2.27). The data point with error bar in each graph indicates the experimental uncertainty.

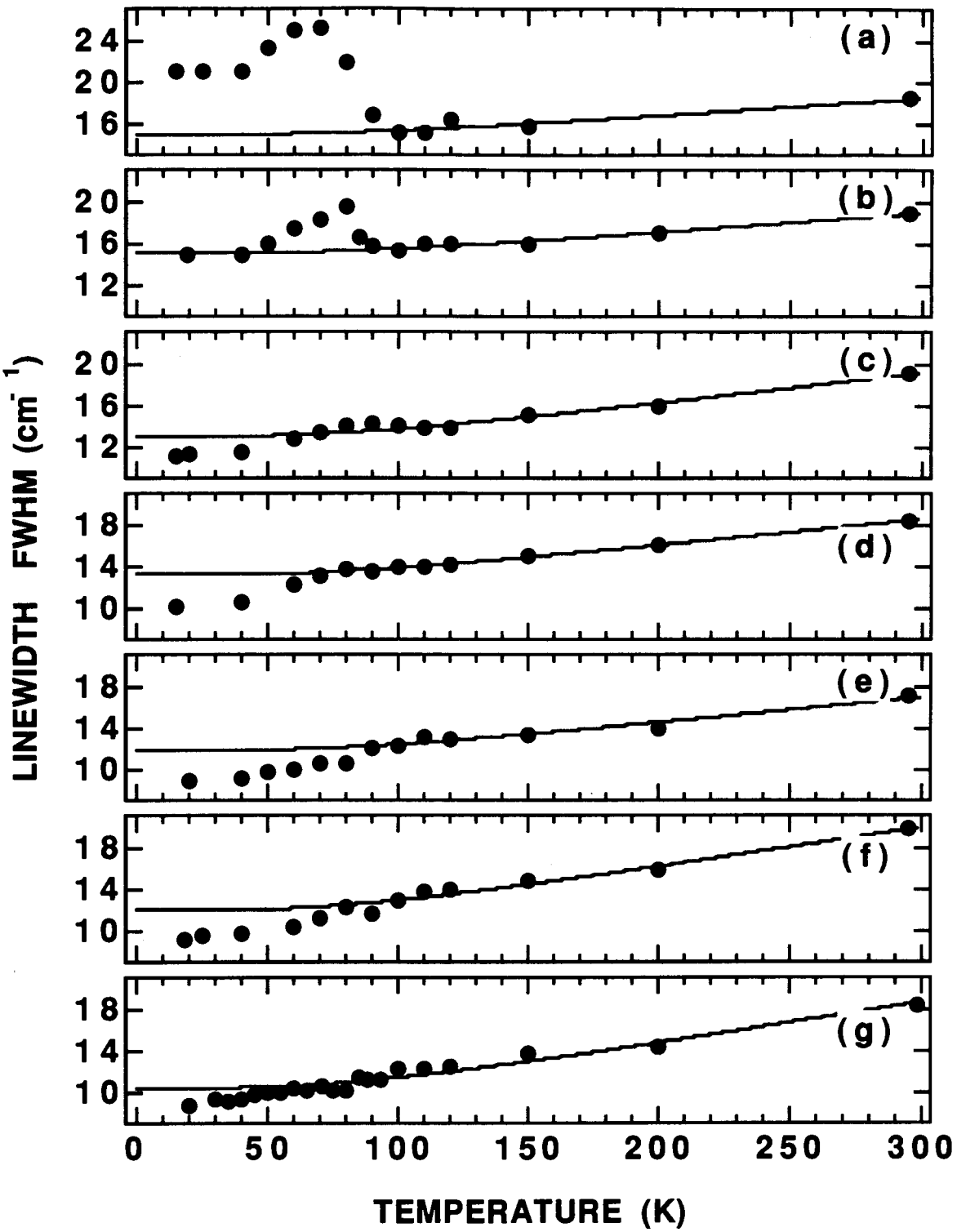
LINEWIDTH FWHM (cm^{-1})
TEMPERATURE (K)
(a)
(b)
(c)
(d)
(e)
(f)
(g)
0
50
100
150
200
250
300

potassium (~ 500 ppm by weight) which should substitute for Ba and thus effectively increase the hole concentration in the crystals.

Finally, the dependences of the inverse of the Fano parameter (unit of -10/q) of the 340 cm^{-1} mode are plotted for all seven crystals in Fig. 6.11. Displaying the Fano parameter dependences in this way allows all the data points to be plotted on a convenient scale with values close to zero indicating a very symmetric line profile. Fig. 6.11 therefore implies that the 340 cm^{-1} phonon peak becomes increasingly more symmetric as the oxygen concentration is reduced in the crystals. This suggests that there may be a reduction in the amount of interaction between the 340 cm^{-1} phonon and the carriers in the deoxygenated crystals. Furthermore, it is clear from Fig. 6.11 (a),(b),(c),(d) that there is a maximum asymmetry (-10/q) in the 340 cm^{-1} peak which moves to higher temperatures as y is reduced from 7.0 to about 6.9. If it is assumed that this minimum in $|q|$ occurs when the phonon energy coincides with a peak in the pair-breaking distribution then it can be concluded that this peak moves to higher energies as oxygen is removed from the crystals.

6.2.4 The 440 and 500 cm^{-1} phonons

All measurements of these phonons were carried out with the incident light polarized parallel to the c-axis of the crystals in the (zz) geometry. Values for the frequencies and linewidths of the 440 and 500 cm^{-1} phonons were obtained by fitting the corresponding Raman peaks to the combination of two profiles, a Lorentzian for the 440 cm^{-1} phonon and a Fano profile for the 500

Figure 6.11

Inverse Fano parameters (units of -10/q) of the 340 cm^{-1} phonon as a function of temperature for (a) crystal A (y=7.0, T_c=89.7 K), (b) crystal B (y=6.99, T_c=92.8 K), (c) crystal C (y=6.93, T_c=93.7 K), (d) crystal D (y=6.90, T_c=92.0 K), (e) crystal E (y=6.86, T_c=91.1 K), (f) crystal F (y=6.81, T_c=87.7 K), and (g) crystal G (y=6.68, T_c=59.2 K) as determined by numerical fits to Fano profiles (equation 2.28) with a linear background. The solid lines are only intended to serve as guides to the eye. Experimental uncertainties in -10/q are represented by the size of the solid circle marker.

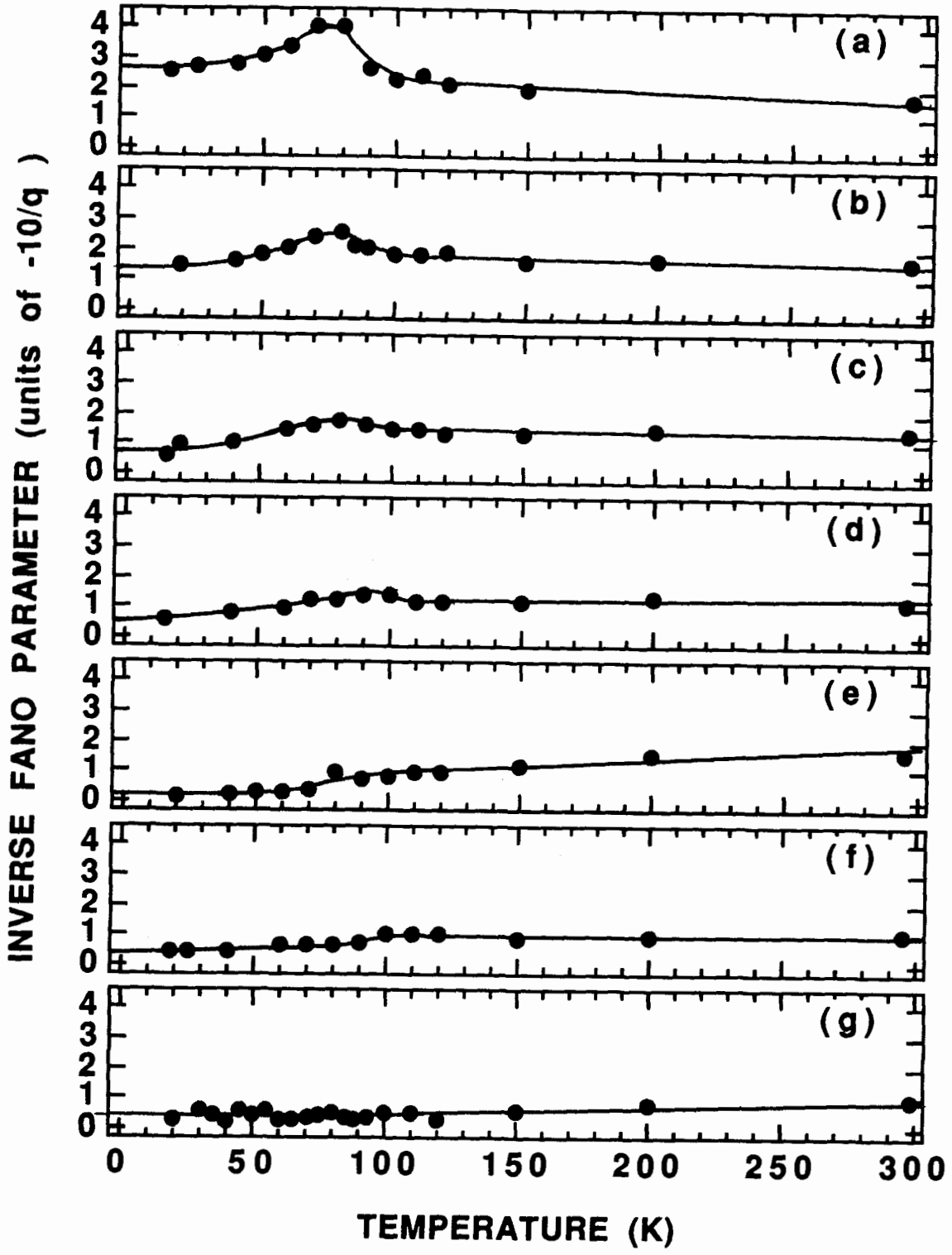
INVERSE FANO PARAMETER (units of -10/q)
(a)
(b)
(c)
(d)
(e)
(f)
(g)
0
1
2
3
4
0
50
100
150
200
250
300
TEMPERATURE (K)

cm^{-1} phonon; thus

$$I = \frac{I_{440}}{1+\varepsilon_{440}^2} + I_{500}\frac{(\varepsilon_{500}+q)^2}{1+\varepsilon_{500}^2} + B \qquad (6.3),$$

where $\varepsilon_v = (\omega - \omega_v)/\gamma_v$, ω_v are the frequencies, γ_v are the linewidths (HWHM), B is a linear background term and q is the Fano asymmetry parameter for the 500 cm^{-1} phonon peak. The relatively weak 440 cm^{-1} Raman peak is located on the wings of the dominant feature at 500 cm^{-1} in all the spectra. The combined fitting procedure (equation 6.3) was adopted in an attempt to account for any mutual interference between these two peaks. This has resulted in a smaller estimate for $\Delta 2\gamma_{440}$ than was obtained by estimating the phonon linewidth in isolation as was done for the crystals grown in thoria crucibles (section 6.1). An example of such a combined Lorentz-Fano profile is shown in Fig. 6.12 superimposed on the experimental data for crystal A at 40 K.

In Fig. 6.13 the temperature dependences of the frequencies of the 440 cm^{-1} mode are plotted. The frequency of this phonon hardens below T_c for crystals A,B,C,D,E, and F and softens marginally in crystal G. The largest shift in frequency is again observed in crystal A, while the amount of hardening is gradually reduced in the deoxygenated crystals. In Fig. 6.14 the temperature dependence of the 500 cm^{-1} mode frequency is plotted for each crystal. As with the 440 cm^{-1} phonon, the 500 cm^{-1} phonon shown in Fig. 6.4, and the observations of other groups [91Ma] [92F], hardening of the 500 cm^{-1} phonon is observed below T_c for crystals A,B,C,D,E, and F. The greatest frequency shift is observed in crystal C which hardens by about 4 cm^{-1}. In contrast to these results a softening of about 2 cm^{-1} is observed in crystal G. It should be noted that this softening (Fig. 6.14(g)) has an onset at approximately 90 K which is

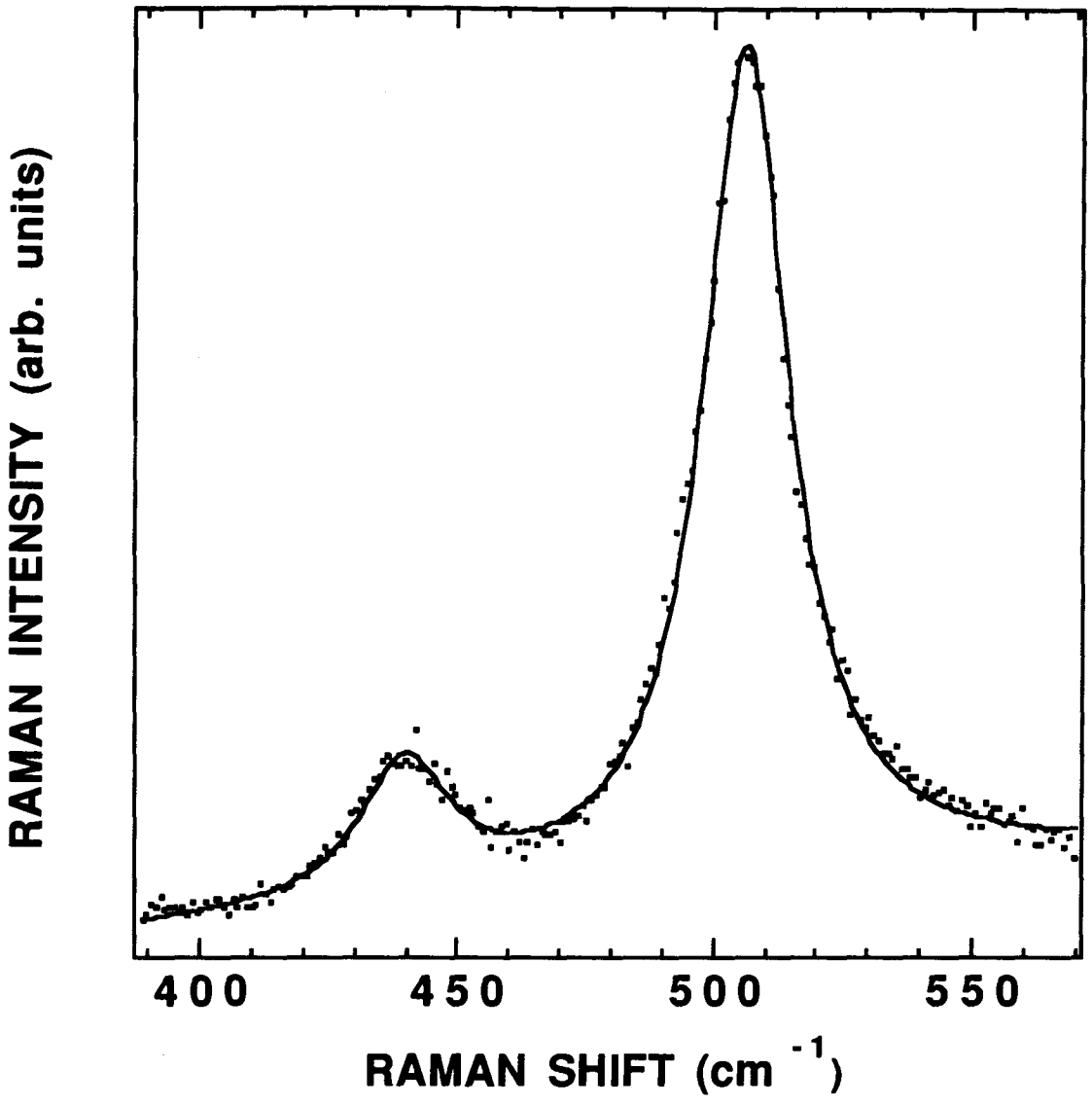

Figure 6.12

The 440 and 500 cm^{-1} peaks obtained at 40 K in the (zz) geometry from crystal A (dots). The solid line represents a fit of the data to the combination of two profiles, a Lorentzian for the 440 cm^{-1} phonon, and a Fano profile for the 500 cm^{-1} phonon, plus a linear background (equation 6.3).

Figure 6.13

Frequencies of the 440 cm^{-1} phonon as a function of temperature for (a) crystal A (y=7.0, T_c=89.7 K), (b) crystal B (y=6.99, T_c=92.8 K), (c) crystal C (y=6.93, T_c=93.7 K), (d) crystal D (y=6.90, T_c=92.0 K), (e) crystal E (y=6.86, T_c=91.1 K), (f) crystal F (y=6.81, T_c=87.7 K), and (g) crystal G (y=6.68, T_c=59.2 K). The solid lines are only intended to serve as guides to the eye. The data point with error bar in each graph indicates the experimental uncertainty.

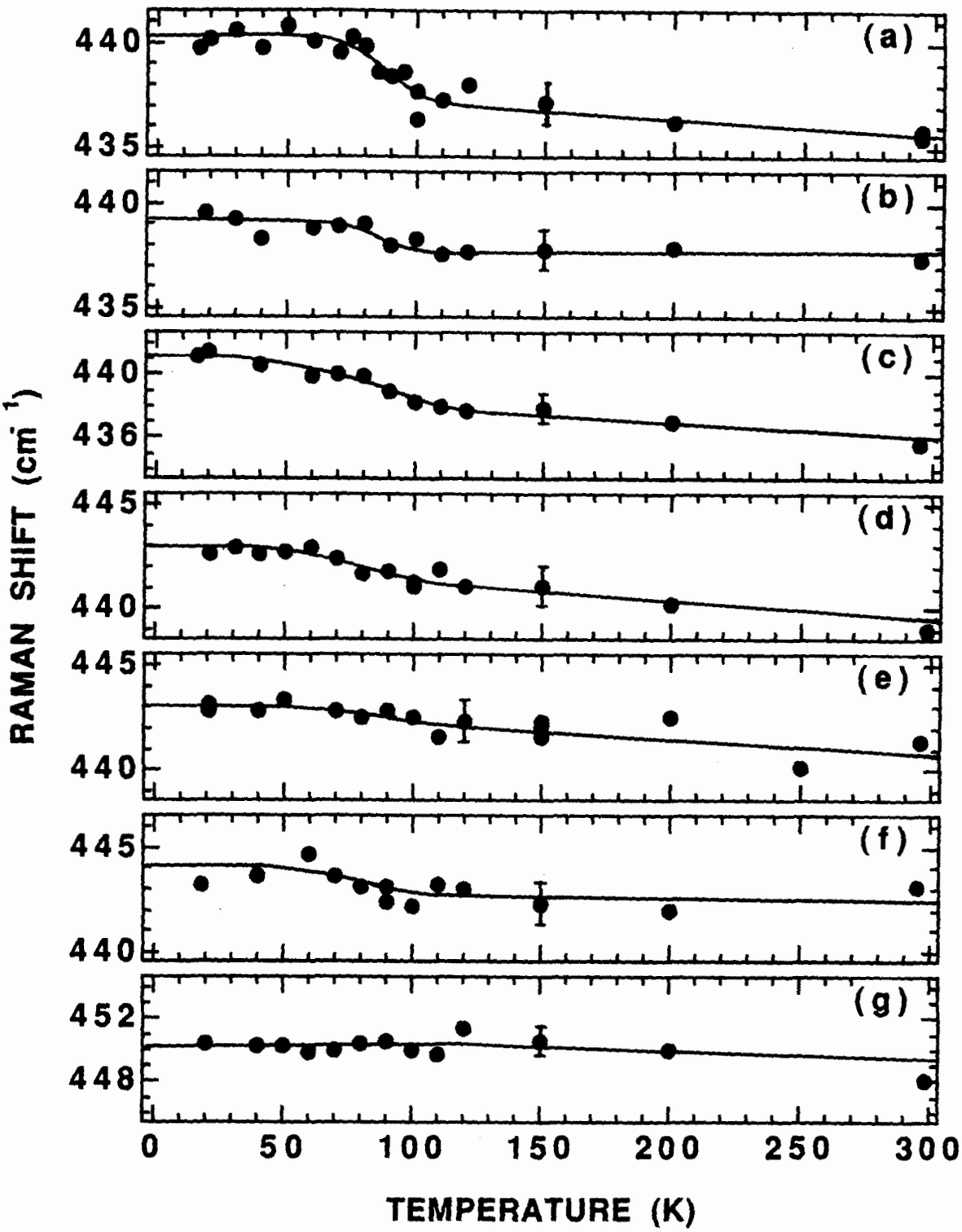
RAMAN SHIFT (cm^{-1})
440
435
(a)
440
435
(b)
440
436
(c)
445
440
(d)
445
440
(e)
445
440
(f)
452
448
(g)
0
50
100
150
200
250
300
TEMPERATURE (K)

Figure 6.14

Frequencies of the 500 cm^{-1} phonon as a function of temperature for (a) crystal A (y=7.0, T_c=89.7 K), (b) crystal B (y=6.99, T_c=92.8 K), (c) crystal C (y=6.93, T_c=93.7 K), (d) crystal D (y=6.90, T_c=92.0 K), (e) crystal E (y=6.86, T_c=91.1 K), (f) crystal F (y=6.81, T_c=87.7 K), and (g) crystal G (y=6.68, T_c=59.2 K). The solid lines are only intended to serve as guides to the eye. The data point with error bar in each graph indicates the experimental uncertainty.

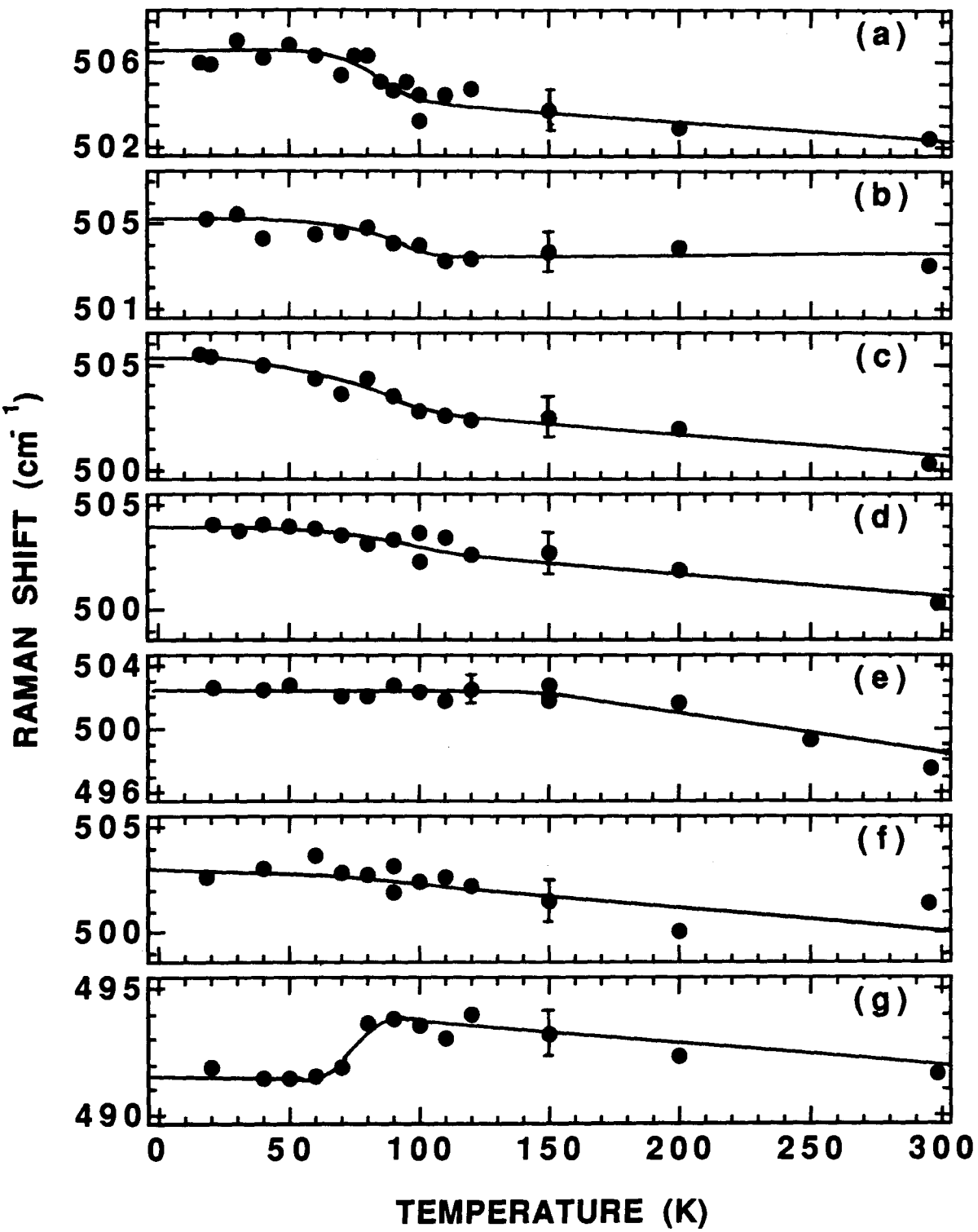
(a)
(b)
(c)
(d)
(e)
(f)
(g)
506
502
505
501
505
500
505
500
504
500
496
505
500
495
490
0
50
100
150
200
250
300
RAMAN SHIFT (cm^{-1})
TEMPERATURE (K)

well above the critical temperature of this crystal ($T_c \approx 60$ K). This suggests that the softening in this crystal is not superconductivity induced. An explanation for such softening above T_c may involve coupling of the phonon to a pseudo-gap due to magnetic excitations as has been suggested by Litvinchuk et al. [92Lb].

In Fig. 6.15 the temperature dependences of the linewidths (FWHM) of the 440 cm^{-1} mode is plotted for crystals A,B,C,D,E,F, and G. In each case, the departure of the experimental data points from the anharmonic decay curve (equation 2.27) below T_c is approximately equal to the experimental uncertainties. This is not the case for the temperature dependences of the linewidths (FWHM) of the 500 cm^{-1} mode shown in Fig. 6.16 for all seven crystals. The 500 cm^{-1} phonon linewidth broadens by approximately 4 cm^{-1} in crystals A,B, and C as shown by the departure of the experimental data points from the anharmonic decay curve (equation 2.27) at 15 K and in a manner similar to that reported by other groups [90Fa] [91Ma] [92Ma]. Crystals D,E, and F show a diminished broadening in the 500 cm^{-1} phonon linewidth of between 1 and 2 cm^{-1} and a narrowing in the 500 cm^{-1} phonon linewidth by about 2 cm^{-1} is observed in crystal G. Finally, the value of the Fano parameter, q, for the 500 cm^{-1} mode in crystals A,B,C,D,E and F varied from about 100 to about 2500 indicating that the 500 cm^{-1} Raman peak in these crystals was highly symmetric and essentially Lorentzian in the (zz) geometry, in agreement with the (zz) spectra of section 6.1. The value of the Fano parameter, q, for the 500 cm^{-1} phonon of crystal G, however, varied between 3 and 5 indicating a highly asymmetric peak. Interestingly, these results differ from those of McCarty et al. [92Ma] which give relatively small negative values for the Fano parameter even in highly oxygenated crystals.

Figure 6.15

Linewidths (FWHM) of the 440 cm^{-1} phonon as a function of temperature for (a) crystal A (y=7.0, T_c=89.7 K), (b) crystal B (y=6.99, T_c=92.8 K), (c) crystal C (y=6.93, T_c=93.7 K), (d) crystal D (y=6.90, T_c=92.0 K), (e) crystal E (y=6.86, T_c=91.1 K), (f) crystal F (y=6.81, T_c=87.7 K), and (g) crystal G (y=6.68, T_c=59.2 K) as determined by numerical fits of the 440 and 500 cm^{-1} Raman peaks to combined Lorentz-Fano profiles (equation 6.3) with a linear background. The solid lines are fits to the data above T_c to a model of anharmonic decay (equation 2.27). The data point with error bar in each graph indicates the experimental uncertainty.

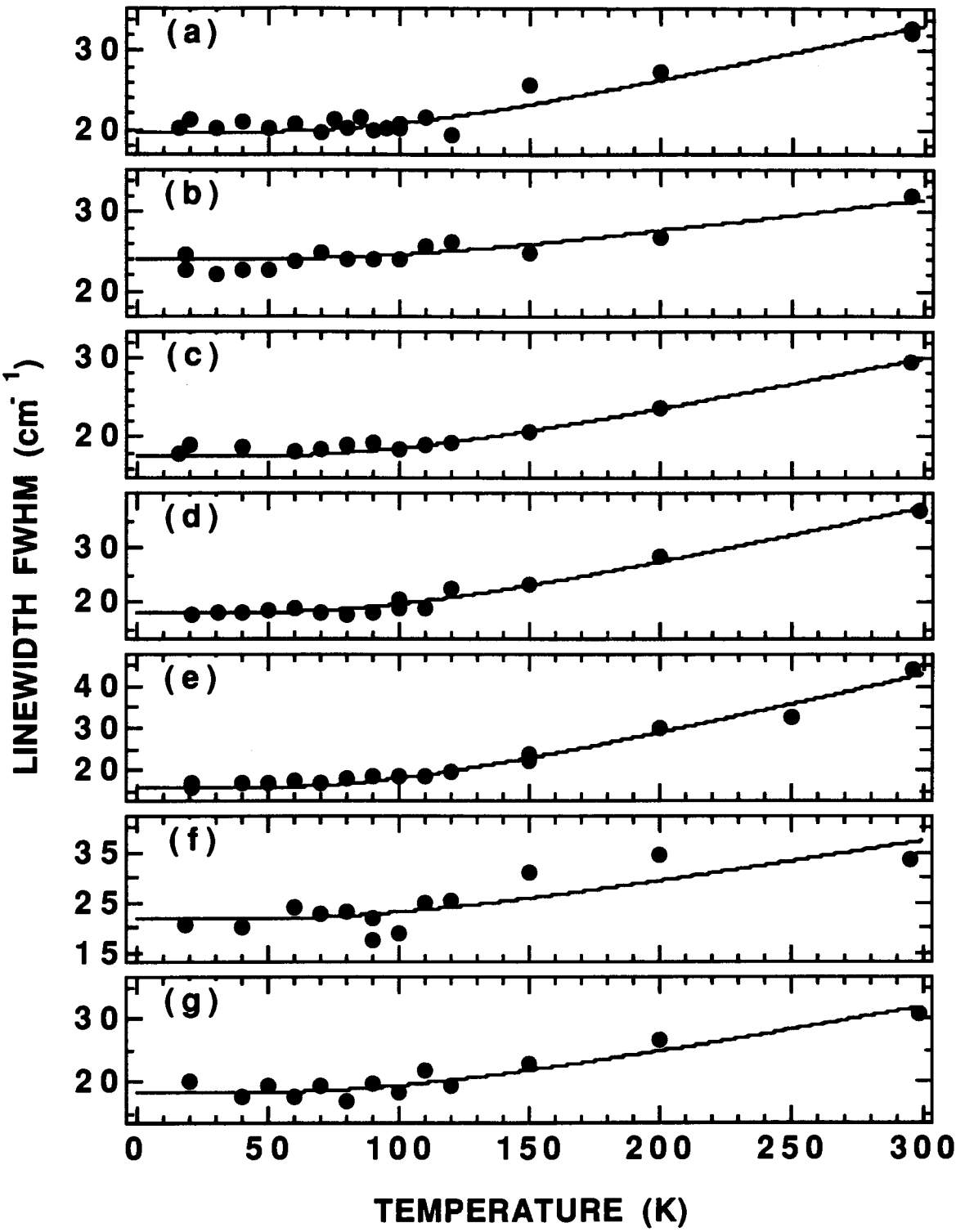
(a)
(b)
(c)
(d)
(e)
(f)
(g)
LINEWIDTH FWHM (cm^{-1})
TEMPERATURE (K)
0
50
100
150
200
250
300

Figure 6.16

Linewidths (FWHM) of the 500 cm^{-1} phonon as a function of temperature for (a) crystal A (y=7.0, T_c=89.7 K), (b) crystal B (y=6.99, T_c=92.8 K), (c) crystal C (y=6.93, T_c=93.7 K), (d) crystal D (y=6.90, T_c=92.0 K), (e) crystal E (y=6.86, T_c=91.1 K), (f) crystal F (y=6.81, T_c=87.7 K), and (g) crystal G (y=6.68, T_c=59.2 K) as determined by numerical fits of the 440 and 500 cm^{-1} Raman peaks to combined Lorentz-Fano profiles (equation 6.3) with a linear background. The solid lines are fits to the data above T_c to a model of anharmonic decay (equation 2.27). The data point with error bar in each graph indicates the experimental uncertainty.

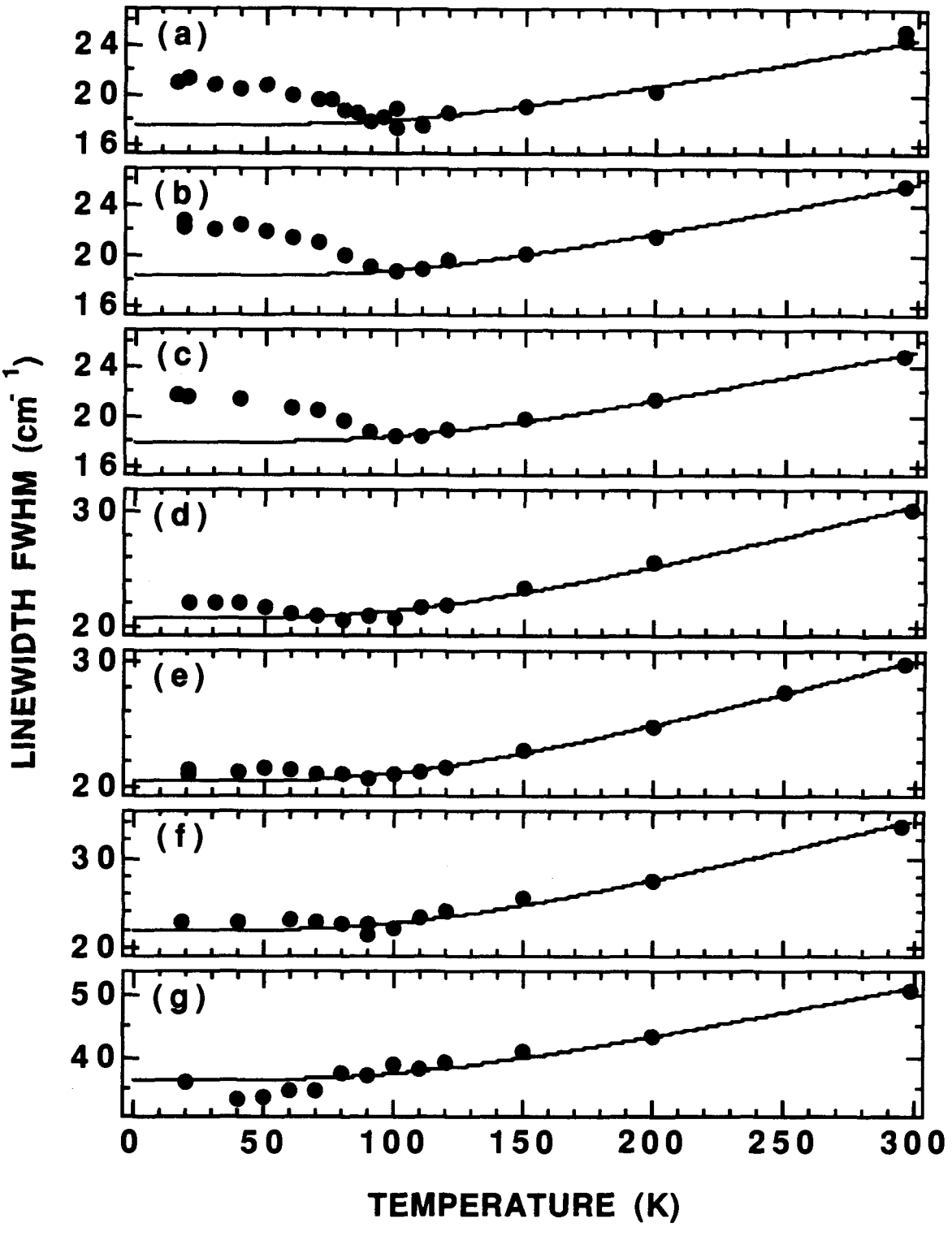
(a)
(b)
(c)
(d)
(e)
(f)
(g)
LINEWIDTH FWHM (cm^{-1})
TEMPERATURE (K)
0
50
100
150
200
250
300

Finally, note that the effects of dispersion in the real part of the self energy (equation 2.35) should only significantly affect the broadening below T_c in the 340 cm^{-1} mode of crystals A and B. The true broadening in these crystals may be up 20% greater [90Fb] than that shown in Fig. 6.10 (a) and (b). For the remaining crystals, as with the crystals described in section 6.1, the dispersion effects are expected to be small.

6.2.5 Discussion

Figures 6.17 and 6.18 summarize the observed superconductivity induced shifts in frequency ($\Delta\omega_v$) and linewidth ($\Delta 2\gamma_v$) respectively as a function of oxygen concentration, y, for crystals A,B,C,D,E,F, and G discussed in this section, and for all three oxygen dependent phonons. Shifts in linewidth, $\Delta 2\gamma_v$, are taken between the experimental data points and the anharmonic decay curve [66K] at 15 K while shifts in frequency, $\Delta\omega_v$, are taken as the difference in the phonon frequencies at 15 K and T_c. It is evident from these figures that although there are variations in the 440 and 500 cm^{-1} frequency and linewidth shifts over the range $6.93 \leq y \leq 7.0$ of oxygen concentrations, they are not as dramatic as the corresponding behavior of the 340 cm^{-1} mode.

Once again, it is of interest to compare the observed superconductivity induced changes in frequency and linewidth to the predictions of strong coupling models [90Z] [92Mb] in an attempt to obtain an estimate for 2Δ in each of the different samples. Ideally, for a given sample the values of $\Delta\omega_v$ and $\Delta 2\gamma_v$ for all three phonons should define a single value for the gap.

Considering first the behavior of the 340 cm^{-1} phonon, comparisons with strong coupling calculations [90Z] ($1/2\Delta\tau$=0.33 curves in Figs. 6.5 and 6.6) suggest that $2\Delta \approx 340$ $cm^{-1} \pm 10$ cm^{-1} ($5.4k_BT_c \pm 0.2k_BT_c$) for crystal A(y = 7.0).

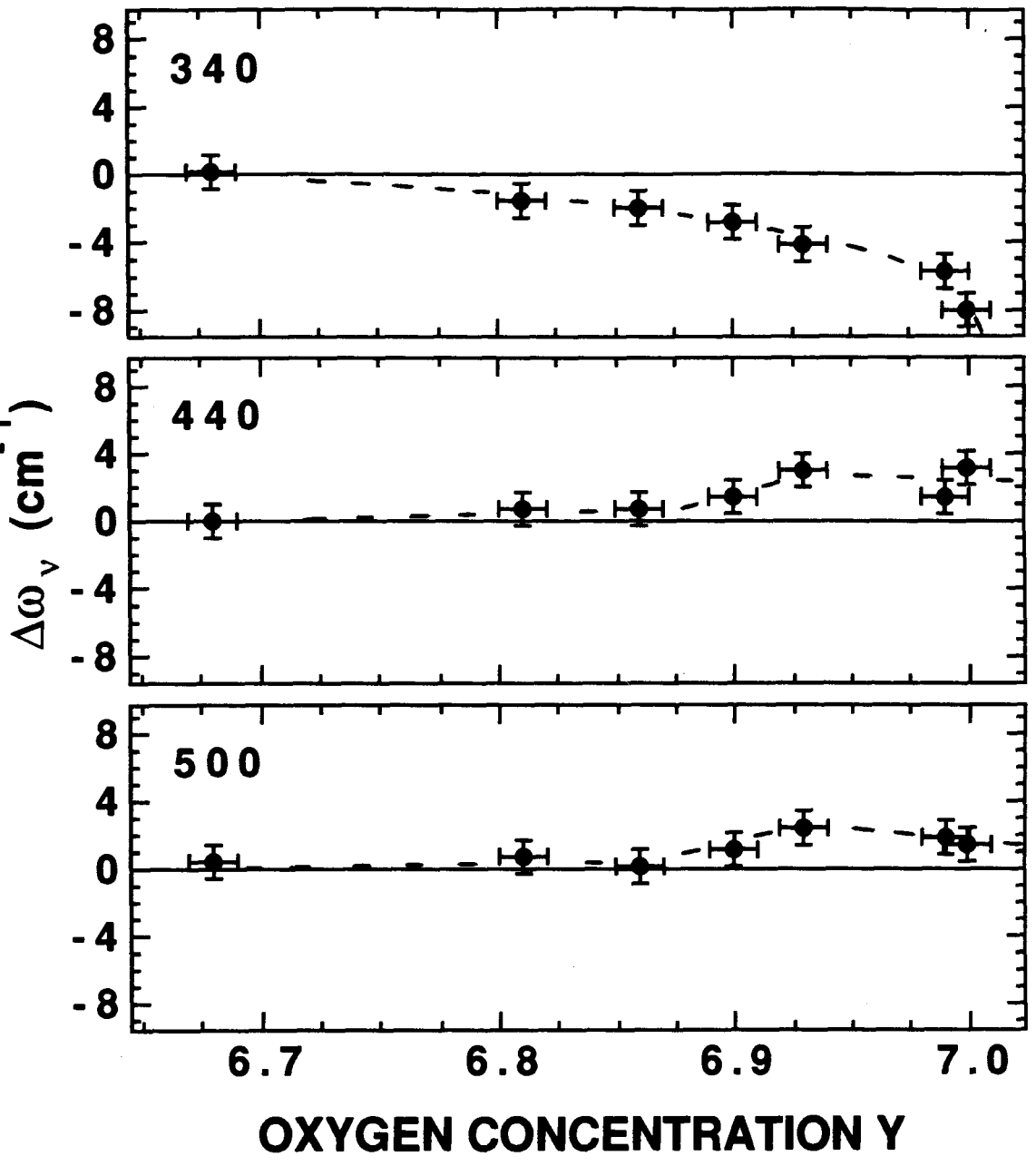

Figure 6.17

Superconductivity induced frequency shifts between 15 K and T_c for the 340, 440 and 500 cm^{-1} phonons as a function of oxygen concentration. Data points with error bars correspond to crystals A, B, C, D, E, F, and G. The dashed lines are only intended to serve as guides to the eye.

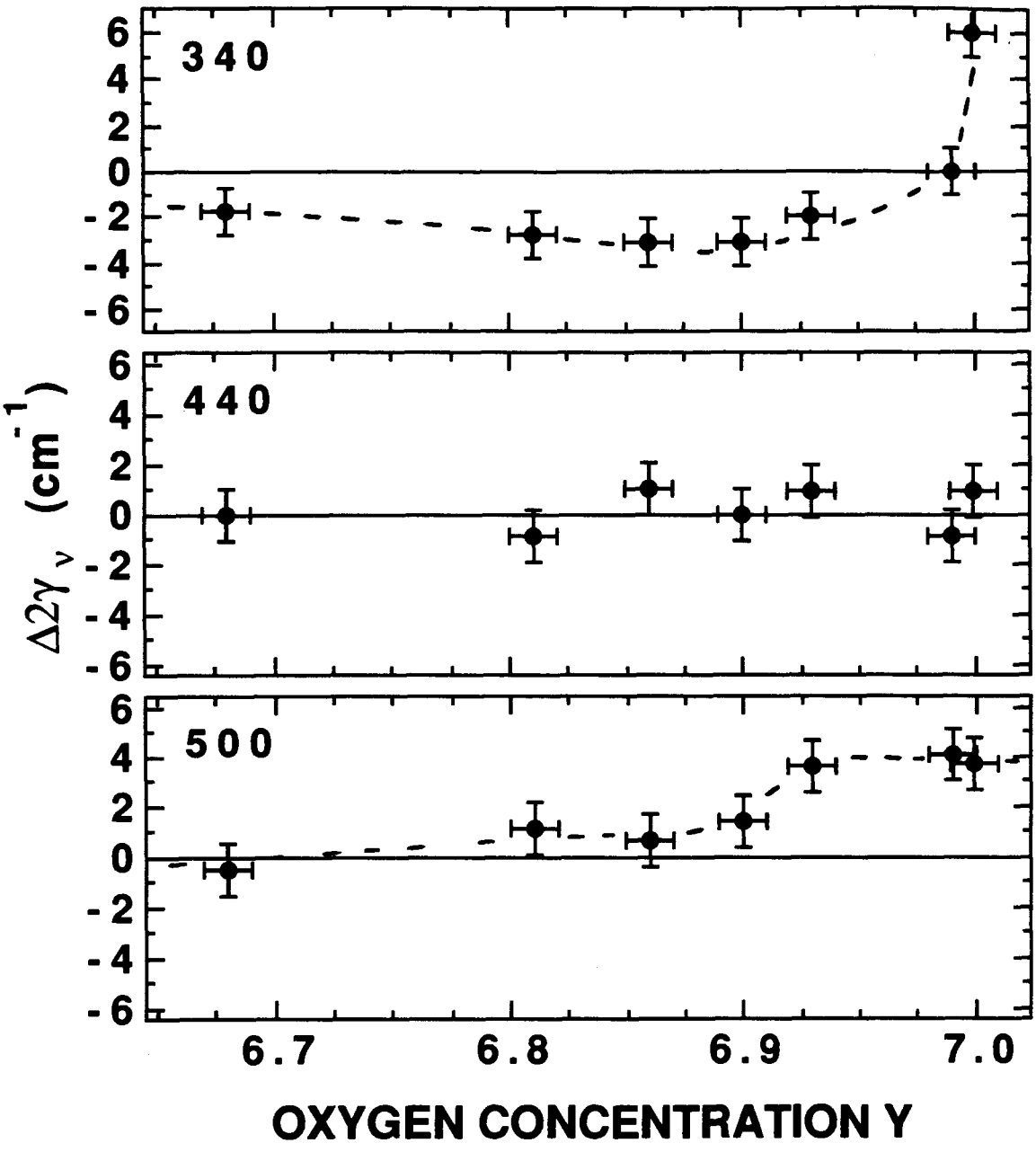

Figure 6.18

Superconductivity induced linewidth shifts (FWHM) at 15 K for the 340, 440, and 500 cm^{-1} phonons as a function of oxygen concentration. Data points with error bars correspond to crystals A, B, C, D, E, F, and G. The dashed lines are only intended to serve as guides to the eye.

The smaller values of $\Delta\omega$ and $\Delta 2\gamma$ obtained for crystals B (y = 6.99) and C (y = 6.93) further suggest that the gap is becoming larger as oxygen is removed from the sample and reaches a value of about $2\Delta \approx 425$ $cm^{-1} \pm 30$ cm^{-1} ($6.7k_BT_c \pm 0.5k_BT_c$) for y = 6.90. As before, in determining these gap values the coupling constant of Rodriguez et al. [90R] has been used. It should be noted that increasing defect or impurity concentrations could also [90Z] [92Mb] result in reductions of $\Delta\omega_v$ and $\Delta 2\gamma_v$ similar to those observed in Figures 6.9, 6.10, 6.13, 6.14, 6.15 and 6.16. However, impurity scattering does not appear to be playing an important role here at least for crystals with $y \gtrsim 6.9$. Support of this statement can be found in the dramatic changes in $\Delta 2\gamma_v$ that occur between samples A and B where $\Delta y \approx 0.01$, the relatively narrow phonon linewidths in crystals with $6.9 \lesssim y \leq 7.0$, and measurements of the surface resistance [92B], scattering rate [92B], and specific heat jump [92La] described in chapter 4 for crystal C with y = 6.93, the results of which are indicative of high quality crystals. The $1/2\Delta\tau$=0.33 curves have, however, been used as in the previous section to allow for some impurity scattering.

From Fig. 6.10 it is also evident that for crystals A,B and C, $\Delta 2\gamma_{340}$ exhibits a maximum relative to the anharmonic decay curve (equation 2.27) [66K] as the temperature is reduced below T_c. This maximum can be interpreted as a resonance between the phonon frequency and a peak in the pair breaking distribution density of states which is moving to higher energies as the temperature is decreased. The maximum broadening occurs at about 65 K, 80 K and 85 K for samples A,B and C respectively and if the peak in the pair breaking density of states is associated with the opening of a gap then these results also suggest that the gap is increasing in energy as y is decreased from 7.0 to 6.93. It should also be noted that the observed peak in

the broadening is correlated with the maximum in -10/q (Fig. 6.11) for the same samples.

Interestingly, an increase in the ratio $2\Delta / kT_c$ from 5.8 for y = 7.0 to 6.8 for y = 6.63 has recently been predicted in a theoretical paper by Monthoux et al. [91Mc] in which magnetic interactions constitute the pairing mechanism. This result thus perhaps provides some plausibility for the increasing gap behavior that has been deduced in this thesis from the 340 cm^{-1} phonon renormalization. It should be noted that the negative values of $\Delta 2\gamma_{340}$ shown in Fig. 6.10 cannot be reconciled with the strong coupling models [92Mb] because rigorous k-vector conservation would normally preclude the normal state decay of a $k \approx 0$ phonon into an electron-hole pair. The observed narrowing thus implies that the usual k-vector selection rules must be relaxed in these compounds. This conclusion is further supported by the observation of an electron-phonon interaction (asymmetric 340 cm^{-1} profile) for $T > T_c$ and the existence of electronic scattering at high energies (see chapter 2).

As the oxygen content in the crystals (D,E,F,G) is reduced below 6.93 $\Delta\omega_{340}$ continues to decrease (Fig. 6.9(d)-(g)) and reaches zero at y = 6.68 while $\Delta 2\gamma_{340}$ remains negative. These results could be interpreted in terms of the strong coupling models [90Z] [92Mb] as implying further increases in gap energy. However, as y decreases the defect concentration in the crystals can be expected to increase with a corresponding increase in the scattering rate $1/\tau$. As shown by the various curves plotted in Figs. 6.5 and 6.6, large scattering rates tend to "wash out" observable phonon renormalization effects and can also lead to linewidth narrowing in the weak coupling limit . Thus the observed results for crystals E to G could be explained by any, or all, of an increasing gap, an increase in the scattering rate or simply by a reduction in

the carrier concentration and hence a smaller coupling constant (equation 2.33).

The behavior of the 500 cm^{-1} mode is qualitatively consistent with the above interpretation of the 340 cm^{-1} phonon behavior in that the phonon both hardens and broadens below T_c for all crystals with y > 6.8 implying that $\omega_{500} > 2\Delta$. The magnitude of the hardening and broadening both decrease as y decreases below 6.9 which could result from a reduced hole concentration and hence smaller coupling constant (equation 2.33) or from an increase in the scattering rate $1/\tau$ (Figs. 6.5, 6.6). In crystal G (y = 6.68), however, the 500 cm^{-1} phonon is observed to both soften and narrow with an onset temperature ($\approx$ 80K) that is significantly larger than the critical temperature ($\approx$ 60K) of this sample and thus these changes are difficult to associate with the onset of superconductivity. It is interesting to note that Slakey et al. [90Sb] in a study of the electronic scattering in a 60K crystal also found that the peak in the B_{1g} electronic continuum was observable at temperatures well above T_c.

The behavior of the 440 mode is however anomalous in that $\Delta 2\gamma_{440} \approx 0$ for all crystals and yet $\Delta\omega_{440} > 0$ for crystals A,B and C. Such behavior does not appear to fit on any pair of strong coupling curves taken from Figs. 6.5 and 6.6. In particular, If an attempt at a more quantitative comparison of $\Delta\omega_\nu$ and $\Delta 2\gamma_\nu$ for the 440 and 500 cm^{-1} modes with the strong coupling model of Zeyher and Zwicknagl [90Z] is made, it becomes clear that neither of these two modes responds in a manner that is completely consistent with a gap that is increasing from 340 cm^{-1} (y = 7.0) to 425 cm^{-1} (y = 6.90) as is implied by the 340 cm^{-1} mode. The 440 cm^{-1} phonon for instance should show significant broadening as the superconducting gap increases and sweeps through the energy of this phonon. Similarly, the 500 cm^{-1} phonon should show increased hardening below T_c and the 440 cm^{-1} phonon should soften for the

crystals with $y \lesssim 6.9$ (see Fig. 6.5). These inconsistencies are similar to those described in the previous section where it was suggested that the 440 and 500 cm^{-1} modes might interact with a different set of electrons than the 340 cm^{-1} phonon. For example the 340 cm^{-1} mode might interact most strongly with the B_{1g} electronic continuum (see chapter 3) and the 440 and 500 cm^{-1} modes with the A_{1g} continuum [88Cb] [88Cc] [90Mb].

CHAPTER 7

CONCLUSIONS

The experimental isotopic frequency shifts listed in Table 5.1 of chapter five indicate that the 500 cm^{-1} phonon in the ^{18}O exchanged polycrystalline samples is shifted on average by about 3.1% of the frequency of the same phonon in the ^{16}O samples. The 340 and 440 cm^{-1} phonons on the other hand are both shifted by about 4.6% on average from the corresponding frequencies in the ^{16}O samples. This significantly larger percentage shift in the 340 and 440 cm^{-1} phonon frequencies suggests that the degree of ^{18}O exchange may not be as complete at the O(4) site, which is involved in the 500 cm^{-1} mode, as it is at the planar O(2) and O(3) sites.

These conclusions are based on the results of a number of dynamical calculations [87Bb] [88Ka] [88Kb] [88Lb] [89B] which suggest that the eigenmodes responsible for the 340, 440, and 500 cm^{-1} phonons are given by the atomic displacement patterns shown in Fig. 3.3. It has been suggested [90C], however, that the 340, 440, and 500 cm^{-1} phonons are strongly hybridized, implying that the O(2), O(3), and O(4) atoms all have significant and roughly comparable amplitudes of vibration for all three modes. This in turn implies that all three phonons should have approximately the same isotopic frequency shifts, in contrast with the results presented in chapter 5. It therefore appears that the experimental results presented in this thesis are more in accord with the eigenmodes and atomic displacement patterns shown in Fig. 3.3.

The linewidth change in the 500 cm^{-1} mode of the ^{18}O exchanged samples is also on average larger than the corresponding change in the linewidth of the 340 cm^{-1} mode (Table 5.2), and is greatest in those samples

where the 500 cm^{-1} mode is frequency shifted by about 50% of the frequency shifts of the 340 and 440 cm^{-1} modes. These observations are also consistent with the previously stated conclusion that the O(2) and O(3) sites are exchanged to a greater degree than the bridging O(4) site.

It should also be mentioned that a number of additional factors could also contribute to the reduced isotope shift of the 500 cm^{-1} mode. In particular, a significant amount of evidence [90Mc] [90Md] suggests that the vibrations of the O(4) atom may be quite anharmonic. It is known [45H] that such anharmonicity can result in reduced isotope shifts. It is not anticipated, however, that such anharmonicity could account entirely for the significantly reduced isotopic frequency shift and broadening observed in the 500 cm^{-1} phonon.

It is also possible that the 500 cm^{-1} phonon, even in isotopically pure samples, could involve some motion of heavier atoms such as Ba or Cu(1) that is not present in the 340 or 440 cm^{-1} modes. This would also result in a relatively smaller percentage isotope shift of the frequency of the 500 cm^{-1} mode. This possibility, however, also appears to be unlikely, in view of experimental results obtained from samples which have been substituted in a number of different ways [89T]. For example, experiments carried out on ^{63}Cu and ^{65}Cu samples [90I] have shown that the copper isotope has no effect on the frequencies of the 340, 440 and 500 cm^{-1} phonons.

These observations have led to the application of the linear chain model to describe the 500 cm^{-1} phonon in $YBa_2Cu_3O_7$. The results of the numerical calculations, using this model and the equation of motion method, are in good agreement with the Raman measurements. In particular, the isotopic frequency shift and degree of broadening in the ^{18}O exchanged samples is well represented by the linear chain model calculations shown in

Figs. 5.3 and 5.5. The O(2) and O(3) atoms are not incorporated into this model, however, and hence the agreement between the experimental and calculated results is consistent with the previously stated conclusion that the degree of hybridization between the 340, 440 and 500 cm^{-1} modes is small, and that the broadening of the 500 cm^{-1} phonon reflects the incomplete ^{18}O exchange at the O(4) site. The linear chain model calculations are therefore also consistent with the eigenmode atomic displacement patterns shown in Fig. 3.3.

Finally, the chain model calculations predict that the isotopic frequency shift does not vary linearly with the degree of ^{18}O exchange as is shown in Fig. 5.4. This is due to the disorder induced motion of the heavier copper atoms which tends to depress the vibrational frequencies. This effect should be taken into consideration when estimating the degree of isotope exchange based on the isotopic frequency shifts.

Having provided evidence for the consistency of the atomic displacement patterns shown in Fig. 3.3 for the 340, 440, and 500 cm^{-1} oxygen dependent phonons, the results of the temperature dependences of these phonons was also examined. The frequency and linewidth self energy shifts below T_c were obtained from Raman measurements on $YBa_2Cu_3O_7$ single crystals containing significant amounts of thorium (section 6.1), and seven batches of $YBa_2Cu_3O_y$ crystals with a range of oxygen concentrations ($6.7 \lesssim y \leq 7.0$) and low levels of impurities (section 6.2). The results obtained from the crystals containing thorium, indicate (Fig. 6.2 (b)) that the presence of this impurity can remove the substantial broadening below T_c of the 340 cm^{-1} mode linewidth (up to ~50%) observed in some ceramic [90Fb] and single crystal [88Cb] samples. Since Th^{4+} substitutes for Y^{3+} in $YBa_2Cu_3O_7$, and hence reduces the hole concentration, it is reasonable to suspect that the hole

concentration is the factor responsible for the variability in the behavior [90Fb] [91Ac] [92Ma] of the superconductivity induced self energy shifts of the 340 cm^{-1} phonon. The results obtained from the seven $YBa_2Cu_3O_y$ crystals (A,B,C,D,E,F, and G) with varying oxygen concentrations, y, are consistent with this conclusion, and indicate a strong sensitivity of the 340 cm^{-1} phonon linewidth and frequency shifts below T_c on the oxygen and hence hole concentration (Figs. 6.9, 6.10). In particular, the 340 cm^{-1} phonon broadens below T_c by up to 8 cm^{-1} in crystal A, which is estimated to be fully oxygenated (y = 7.0), and narrows below T_c in crystal C, which is only slightly deoxygenated (y = 6.93).

Hadjiev et al. [91H] have correlated a lack of broadening of the 340 cm^{-1} mode with the appearance of features at 232 and 598 cm^{-1}. They have further attributed these modes to forbidden (ir-active) vibrations of the chain atoms which become Raman active because of defect induced disorder in the chains. The results presented in this thesis are consistent with this interpretation in that these modes are also observed in the oxygen depleted ($YBa_2Cu_3O_y$), and hence chain disordered, samples. As mentioned above, however, a lack of broadening of the 340 cm^{-1} mode was observed in the samples containing Th, and yet there was no indication of the features at 232 and 598 cm^{-1} in the spectra (Fig. 6.1). It may therefore be concluded that the modes at 232 and 598 cm^{-1} will be correlated with a lack of broadening only if the hole concentration is reduced by chain defects created by oxygen removal or impurity substitution (eg. gold [91Ma]) on the chain sites.

Estimates for the superconducting gap energy, 2Δ, based on the behavior below T_c of the 340 cm^{-1} phonon and comparisons with strong coupling theories [90Z] [92Mb], therefore vary from $2\Delta \approx 340$ cm^{-1} ($\sim 5.4 k_B T_c$) for crystal A (y=7.0), to $2\Delta \approx 425$ cm^{-1} ($\sim 6.7 k_B T_c$) for the oxygen reduced

$YBa_2Cu_3O_y$ (y=6.9) crystal, and $YBa_2Cu_3O_7$ crystals containing Thorium. Values for the superconducting gap energy, 2Δ, for the more heavily deoxygenated crystals ($y < 6.9$) are difficult to estimate due to the substantially increased scattering rates and decreased carrier concentrations anticipated in these samples.

The superconductivity induced changes in linewidths and frequencies below T_c of the 440 and 500 cm^{-1} phonons in the $YBa_2Cu_3O_y$ crystals also vary with the oxygen or hole concentration (Figs. 6.13 to 6.16), although to a lesser extent than the 340 cm^{-1} phonon. It does not, however, appear to be possible to consistently incorporate the superconductivity induced self energy shifts of the 440 and 500 cm^{-1} phonons into the strong coupling model of Zeyher and Zwicknagl [90Z], assuming the superconducting gap energies determined from the behavior of the 340 cm^{-1} phonon. As discussed in chapter six, the 440 cm^{-1} linewidth for instance either undergoes no broadening ($YBa_2Cu_3O_y$ crystals, Fig. 6.15), or a degree of broadening which is far less than that expected given the proximity of the energy of the 440 cm^{-1} phonon to the superconducting gap energy, 2Δ, ($YBa_2Cu_3O_7$ crystals containing thorium, Fig. 6.6). The linewidths shifts below T_c of the 440 and 500 cm^{-1} phonons should also increase significantly in the deoxygenated $YBa_2Cu_3O_y$ crystals if the gap increases as implied by the behavior of the 340 cm^{-1} phonon.

These discrepancies suggests that there may be two or more gaps, or quasi-gaps, with different symmetries. The 340 cm^{-1} phonon for example might interact more strongly with a gap with B_{1g} symmetry and the 440 and 500 cm^{-1} phonons with a gap with A_g symmetry. More specifically, if the different gaps correspond to the redistribution of electronic states associated with the Raman background then it may be that the 340 cm^{-1} mode interacts

most strongly with the B_{1g} component of this background and the 440 and 500 cm^{-1} modes with the A_{1g} component (tetragonal notation) of the Raman background. These possibilities are presently being investigated through further research which will hopefully lead to a better understanding of the mechanism of superconductivity in $YBa_2Cu_3O_7$ and related high temperature superconductors.

References

11O H. Kamerlingh Onnes, Leiden Comm. 120b, 122b, 124c (1911)

27R C.V. Raman, J. Optical Soc. America, 15, 185 (1927).

28Ra C.V. Raman and K.S. Krishnan, Nature 121, 501, 619 (1928).

28Rb C.V. Raman and K.S. Krishnan, Indian Journal of Physics 2, 399 (1928).

28Rc C.V. Raman and K.S. Krishnan, Proc. Roy. Soc. 122A, 23 (1928).

45H G. Herzberg, *Infrared and Raman Spectra*, (Van Nostrand Reinhold, New York, 1945).

50M E. Maxwell, Phys. Rev. 78, 477 (1950).

57B J. Bardeen, L.N. Cooper, and J.R. Schrieffer, Phys. Rev. 108, 1175 (1957).

60K D.A. Kleinman, Physical Review 118, 118 (1960).

62K J. Kokkedee, Physica 28, 374 (1962).

66G J.J. Gilman, *The Art and Science of Growing Crystals*, (John Wiley and Sons Inc. 1966) p. 252.

66K P.G. Klemens, Physical Review 148, 845 (1966).

66P David Pines and Philippe Nozieres, *The theory of Quantum liquids Vol. I : Normal Fermi Liquids*, (W.A. Benjamin Inc. New York, 1966). p. 108.

68M D.L. Mills, A.A. Maradudin and E. Burstein, Phys. Rev. Lett. 21, 1178 (1968).

69B Gordon Baym, *Lectures on Quantum Mechanics*, (W.A. Benjamin Inc. 1969) pp. 294-296.

69J J. Jortner and G.C. Morris, Journal of Chemical Physics, 51, 3689 (1969).

69M A. Maitland and M.H. Dunn, *Laser Physics*, (North Holland Publishing Company, 1969) pp. 384-387.

70S Benjamin Sharf, Chem. Phys. Lett. 5, 456 (1970).

71Ma G.P. Montgomery Jr., Impurity induced Raman scattering in Alkali-Halides, Ph.D. thesis, 1971.

71Mb A.A. Maradudin, E.W. Montroll, G.H. Weiss, and I.P. Ipatova, *Theory of Lattice dynamics in the Harmonic Approximation*, (Academic Press, 1971) p. 47.

73A J.D. Axe and G. Shirane, Phys. Rev. B8, 1965 (1973).

73K J.F. Kielkopf, Journal of the Optical Society of America, 63, 987 (1973).

74F U. Fano, Phys. Rev. 124, 1866 (1961).

74S Stephen Gasiorowicz, Quantum Physics, John Wiley and Sons, 1974. p. 341.

75S S.M. Shapiro, G. Shirane and J.D. Axe, Phys. Rev B12, 4899 (1975).

77Ba Gerald Burns, *Introduction to Group theory with applications*, (Academic Press, 1977), pp. 105-122.

77Bb D. Beeman and R. Alben, Adv. Phys. 26, 339 (1977).

77H John Allen Holy, Raman scattering from Metals, Ph.D. thesis, 1977.

78H William Hayes and Rodney Loudon, Scattering of Light by Crystals, (John Wiley and Sons, 1978), p. 38.

81K M.V. Klein, *Electronic Raman Scattering, Topics in Applied Physics Vol 8, Light Scattering in Solids I,* edited by M. Cardona, (Springer-Verlag 1983), p. 172.

83D S.B. Dierker, M.V. Klein, G.W. Webb and Z. Fisk, Phys. Rev. Lett. 50, 853 (1983).

83P A. Pinczuk and E. Burstein, in *Light Scattering in Solids I,* edited by M. Cardona, (Springer-Verlag, 1983), p. 32.

84A G. Abstreiter, M. Cardona, and A. Pinczuk, in *Light Scattering in Solids IV,* edited by M. Cardona and G. Güntherodt, (Springer-Verlag, 1984), p.54.

84J Peter A. Jansson, *Deconvolution with Applications in Spectroscopy,* (Academic press, 1984) p. 10.

84K M.V. Klein and S.B. Dierker, Phys. Rev. B29, 4976 (1984).

84M Jose Menendez and Manuel Cardona, Phys. Rev. B29, 2051 (1984).

85B J.S. Blakemore, *Solid State Physics, second edition,* (Cambridge University Press, 1985), pp. 277-281.

86B J.G. Bednorz and K.A. Müller, Z. Phys. B64, 189 (1986).

86S D.J. Scalapino, E. Loh, J. Hirsch, Phys. Rev. B34, 8190 (1986).

87A P.W. Anderson, Science 235, 1196 (1987).

87Ba R. Batlogg, R.J. Cava, A. Jayaraman, R.B. Van Dover, G.A. Kourouklis, S. Sunshine, D.W. Murphy, L.W. Rupp, H.S. Chen, A. White, K.T. Short, A.M. Mujsce, and E.A. Reitman, Phys. Rev. Lett. 58, 2333 (1987).

87Bb F.E. Bates and J.E. Eldridge, Solid State Commun. 64, 1435 (1987).

87C R.J. Cava, B. Batlogg, C.H. Chen, E.A. Rietman, S.M. Zahurak and D. Werder, Phys. Rev. B36, 5719 (1987).

87G C.E. Gough, M.S. Coklough, E.M. Forgan, R.G. Jordan, M. Keene, C.M. Muirhead, A.I.M. Rae, N. Thomas, J.S. Abell and S. Sutton, Nature, 326, 855 (1987).

87L K.J. Leary, H.C. Zur Loye, S.W. Keller, T.A. Faltens, W.K. Ham, J.N. Michaels and A.M. Stacy, Phys. Rev. Lett. 59, 1236 (1987).

87J J. Niemeyer, M.R. Dietrich, C. Politis, Z. Phys. B67, 155 (1987).

87M R.M. Macfarlane, H.J. Rosen and H. Seki, Solid State Commun. 63, 831 (1987).

87P R.H. Parmenter, Phys. Rev. Lett. 59, 923 (1987).

87W M.K. Wu, J.R. Ashburn, C.J. Torng, P.H. Hor, R.L. Meng, L. Gao, Z. J. Huang, Y.Q. Wang, and G.W Chu, Phys. Rev. Lett. 58, 908 (1987).

88Ca M. Cardona, R. Liu, C. Thomsen, W. Kress, E. Schönherr, M. Bauer, L. Genzel, and W. König, Solid State Commun. 67, 789 (1988).

88Cb S.L. Cooper, M.V. Klein, B.G. Pazol, J.P. Rice and D.M. Ginsberg, Phys. Rev. B37, 5920 (1988).

88Cc S.L. Cooper, F. Slakey, M.V. Klein, J.P. Rice, E.D. Bukowski and D.M. Ginsberg, Phys. Rev. B38, 11934 (1988).

88Cd M. Cardona, R. Liu, C. Thomsen, M. Bauer, L. Genzel, W. König, and A. Wittlin, Solid State Commun. 65, 71 (1988).

88F R. Feile, U. Schmitt, P. Leiderer, J. Schubert, and U. Poppe, Z. Phys. B. Condensed Matter 72, 161 (1988).

88H R. Hackl, W. Gläser, P. Müller, D. Einzel, and K. Andres, Phys. Rev. B38, 7133 (1988).

88Ka W. Kress, U. Schröder, J. Prade, A.D. Kulkarni, and F.W. de Wette, Phys. Rev. B38, 2906 (1988).

88Kb W. Kress, J. Prade, U. Schröder, A.D. Kulkarni, and F.W. de Wette, Physica C162-164, 1345 (1989).

88Kc M. Krantz, H.J. Rosen, R.M. Macfarlane and V.Y. Lee, Phys. Rev. B38, 4992 (1988).

88La R.B. Laughlin, Science 242, 525 (1988).

88Lb R. Liu, C. Thomsen, W. Kress, M. Cardona, B. Gegenheimer, F.W. de Wette, J. Prade, A.D. Kulkarni and U. Schroder, Phys. Rev. B37, 7971 (1988).

88Lc B.H. Loo, M.K. Wu, D.H. Burns, A. Ibrahim, C. Jenkins, T. Rolin and D.O. Frazier, in *High-Temperature Superconducting materials: preparations properties and processing,* edited by William E. Hatfield, and John H. Miller Jr. (Marcel Dekker, 1988) pp. 349-366.

88Ma R.M. Macfarlane, H.J. Rosen, E.M. Engler, R.D. Jacowitz, and V.Y. Lee, Phys.Rev. B38, 284 (1988).

88Mb K.F. McCarty, J.C. Hamilton, R.N. Shelton, and D.S. Ginley, Phys. Rev. B38, 2914 (1988).

88Mc William Gordon McMullan, Applications of a high sensitivity imaging photomultiplier tube to optical spectroscopy, Ph.D. thesis, 1988.

88P M.P. Petrov, A.I. Grachev, M.V. Krasin'kova, A.A. Nechitailov, V.V. Prokofiev, V.V. Poborchy, S.I. Shagin, and N.F. Kartenko, Solid State Commun. 67, 1197 (1988).

88R T. Ruf, C. Thomsen, R. Liu, and M. Cardona, Phys. Rev. B38, 11985 (1988).

88S A.W. Sleight, in High-Temperature Superconducting materials: preparations properties and processing, edited by William E. Hatfield, and John H. Miller Jr. (Marcel Dekker, 1988) p. 18.

88Ta J.S. Tsai, I. Takeuchi, J. Fujitu, T. Voshitake, S. Miura, S. Tanaka, T. Terashima, Y. Bando, K. Iijima, and K. Yamamoto, Physica C153-155, 1385 (1988).

88Tb C. Thomsen, R. Liu, M. Cardona, U. Amador and E. Moran, Solid State Commun. 67, 271 (1988).

88Tc J.M. Tarascon, P. Barboux, P.F. Miceli, L.H. Greene, G.W. Hull, M. Eibschutz and S.A. Sunshine, Phys. Rev. B37, 7458 (1988).

88Td C. Thomsen, R. Liu, A. Wittlin, L. Genzel, M. Cardona, and W. König, Solid State Commun. 65, 219 (1988).

88Te C. Thomsen, M. Cardona, B. Gegenheimer, R. Liu, and A. Simon, Phys. Rev. B37, 9860 (1988).

89B F.E. Bates, private communication.

89Ca S.L. Cooper, F. Slakey, M.V. Klein, J.P. Rice, E.D. Bukowski and D.M. Ginsberg, J. Opt. Soc. Am. B6, 436 (1989).

89Cb M. Cardona, C. Thomsen, in *High-T_c Superconductors: Electronic Structure*, edited by A Bianconi, and A. Marcelli, (Pergamon Oxford, 1989) p. 79.

89F J.P. Franck, J. Jung, G.J. Salomons, W.A. Miner, M. A. -K. Mohamed, J. Chrzanowski, S. Gygax, J.C. Irwin, D.F. Mitchell, and I. Sproule, Physica C162-164, 753 (1989).

89Ga D.M. Ginsberg, in Physical Properties of High Temperature Superconductors I, edited by D.M. Ginsberg (World Scientific, 1989) p. 4.

89Gb L. Genzel, A. Wittlin, M. Bauer, M. Cardona, E. Schönherr, and A. Simon, Phys. Rev. B40, 2170 (1989).

89Ha V. Daniel Hunt, *Superconductivity Sourcebook*, (John Wiley and Sons, 1989).

89Hb R. Hackl, R. Kaiser, W. Glaser: Physica C162-164, 431 (1989).

89I J.-M. Imer, F. Patthey, B. Dardel, W.-D. Schneider, Y. Baer, Y. Petroff, and A. Zettl, Phys. Rev. Lett. 62, 336 (1989).

89M H. Monien and A. Zawadowski, Phys. Rev. Lett. 63, 911 (1989).

89P M. Plischke, B. Bergersen, *Equilibrium Statistical Mechanics*, (Prentice Hall, 1989) pp. 257-258.

89T C. Thomsen and M. Cardona, in Physical Properties of High Temperature Superconductors I, ed. D.M. Ginsberg (World Scientific, Singapore, 1989) pp. 419-426.

89V C.M. Varma, P.B. Littlewood and S. Schmitt-Rink, Phys. Rev. Lett. 63, 1989.

89W D.J. Werder, C.H. Chen, M. Gurvitch, B. Miller, L.F. Schneemeyer, and J.V. Waszczak, Physica C160, 411 (1989).

90A E. Altendorf, J. Chrzanowski, J.C. Irwin and J.P. Franck, Solid State Commun. 76, 391 (1990).

90B B. Batlogg, in Selected Experiments on High T_c Cuprates, High Temperature Superconductivity: The Los Alamos Symposium-1989, edited by K. Bedell, D. Coffey, D. Meltzer, D. Pinese, and J.R. Schrieffer, (Addison-Wesley Publishing Company, 1990) p. 46.

90C R.E. Cohen, W.E. Pickett, and H. Krakauer, Phys. Rev. Lett. 64, 2575 (1990).

90Fa B. Friedl, C. Thomsen, E. Schönherr and M. Cardona, Solid State Commun. 76, 1107 (1990).

90Fb B. Friedl, C. Thomsen and M. Cardona, Phys. Rev. Lett. 65, 915 (1990).

90Fc G. Salomons, W.A. Miner, M.A.-K. Mohamed, J. Chrzanowski, S. Gygax, J.C. Irwin, D.F. Mitchell and G.I. Sproule, Physica C172, 90 (1990).

90I J.C. Irwin, J. Chrzanowski, E. Altendorf, J. Jung, and J.P. Franck, J. Mater. Res. 5, 2780 (1990).

90J J.D. Jorgensen, B.W. Veal, A.P. Paulikas, L.J. Nowicki, G.W. Crabtree, H. Claus, and W.K. Kwok, Phys. Rev. B41, 1863 (1990).

90Ma K.F. McCarty, J.Z. Liu, R.N. Shelton, and H.B. Radousky, Phys. Rev. B41, 8792 (1990).

90Mb K.F. McCarty, J.Z. Liu, R.N. Shelton and H.B. Radousky, Phys. Rev. B42, 9973 (1990).

90 Mc D. Mihailovic and C.M. Foster, Solid State Commun. 74, 753 (1990).

90Md J. Mustre de Leon, S. Conradson, I. Batistic, and A. Bishop, Phys. Rev. Lett. 65, 1675 (1990).

90R C.O. Rodriguez, A.I. Liechtenstein, I.I. Mazin, O. Jepsen, O.K. Andersen and M. Methfessel, Phys. Rev. B42, 2692 (1990).

90Sa Z. Schlesinger, R.T. Collins, F. Holtzberg, C. Feild, S.H. Blanton, U. Welp, G.W. Crabtree, Y. Fang, and J.Z. Liu, Phys. Rev. Lett. 65, 801 (1990).

90Sb F. Slakey, M.V. Klein, J.P. Rice and D.M. Ginsberg, Phys. Rev. B42, 2643 (1990).

90Ta C. Thomsen, M. Cardona, B. Friedl, C.O. Rodriguez, I.I. Mazin and O.K. Andersen, Solid State Commun., 75, 219 (1990).

90Tb D. R. Tilley and J. Tilley, *Superfluidity and Superconductivity*, Third edition, (Adam Hilger, 1990), p. 130.

90Z R. Zeyher and G. Zwicknagl, Z. Phys. B, Condensed Matter 78, 175 (1990).

91Aa E. Altendorf, J. Chrzanowski, J.C. Irwin, and J.P. Franck, Phys. Rev. B43, 2771 (1991).

91Ab E. Altendorf, J. Chrzanowski, J.C. Irwin, A. O'Reilly and W.N. Hardy, Physica C 175, 47 (1991).

91Ac E. Altendorf, J.C. Irwin, R. Liang and W.N. Hardy, Solid State Commun. 80, 627 (1991).

91B Bertram Batlogg, Physics Today, June, 1991, p.41.

91H V.G. Hadjiev, C. Thomsen, A. Erb, G. Müller-Vogt, M.R. Koblischka and M. Cardona, Solid State Commun. 80, 643 (1991).

91K M.V. Klein, S.L. Cooper, A.L. Kotz, Ran Liu, D. Reznik, F. Slakey, W.C. Lee, D.M. Ginsberg, Physica C185-189, 72 (1991).

91Ma K.F. McCarty, H.B. Radousky, J.Z. Liu and R.N. Shelton, Phys. Rev. B43, 13751 (1991).

91Mb K.F. McCarty, J.Z. Liu, Y.X. Jia, R.N. Shelton and H.B. Radousky, Solid State Commun. 79, 359 (1991).

91Mc P. Monthoux, A.V. Balatsky and D. Pines, Phys. Rev. Lett. 67, 3448 (1991).

91O Israel Ohana, M.S. Dresselhaus and S. Tanuma, Phys. Rev. B43, 1773 (1991).

91S P. Schleger, W.N. Hardy and B.X. Yang, Physica C176, 261 (1991).

91T C. Thomsen, B. Friedl, M. Cieplak and M. Cardona, Solid State Commun. 78, 727 (1991).

91V K.G. Vandervoort, U. Welp, J.E. Kessler, H. Claus, G.W. Crabtree, W.K. Kwok, A. Umezawa, B.W. Veal, J.W. Downey, and A.P.Paulikas, Phys. Rev B43, 13042 (1991).

92A E. Altendorf, J.C. Irwin, R. Liang and W.N Hardy, Phys. Rev. B45, 7551 (1992).

92B D.A. Bonn, P. Dosanjh, R. Liang and W.N. Hardy, Phys. Rev. Lett. 68, 2390 (1992).

92F B. Friedl, C. Thomsen, H. -U. Habermeier, and M. Cardona, Solid State Commun. 81, 989 (1992).

92La Ruixing Liang, P. Dosanjh, D.A. Bonn, D.J. Baar, J.F. Carolan and W.N. Hardy, Physica C195, 51 (1992).

92Lb A.P. Litvinchuk, C. Thomsen and M. Cardona, Solid State Commun., 83, 343 (1992).

92Ma K.F. McCarty, J.Z. Liu, Y.X. Jia, R.N. Shelton and H.B. Radousky, Physica C192, 331 (1992).

92Mb F. Marsiglio, R. Akis and J.P. Carbotte, Phys. Rev. B45, 9865 (1992).

92Mc A.A. Maksimov, A.V. Puchkov, I.I. Tartakovskii, V.B. Timofeev, D. Reznik and M.V. Klein, Solid State Commun. 81, 407 (1992).

92T C. Thomsen, in *Light Scattering in Solids VI*, (Springer-Verlag, 1991) p. 285.

92W H. Wang, F.D. Medina, Y.D. Zhou, and Q.N. Zhang, Phys. Rev. B45, 10356 (1992).

[E] Elemental Research, Vancouver, B. C.

[Q] Quanta Trace Laboratories, Burnaby, B.C.